



**Analytical, computational and experimental investigations of  
architected beams and panels.**

by

Ahmed Saleh Dalaq

Department of Mechanical Engineering  
McGill University

Montreal, Quebec, Canada

December 2019

A thesis submitted to McGill University in partial fulfillment of the requirements for a  
doctoral degree

© Ahmed Saleh Dalaq, 2019

# **Dedication**

*To the one that belongs to [Him] all the best names. To Sharifah (mother) and Saleh (father)*

# Table of Contents

<b>List of Figures</b> .....	<b>vi</b>
<b>List of Tables</b> .....	<b>xii</b>
<b>Nomenclature</b> .....	<b>xiii</b>
<b>Abstract</b> .....	<b>xvi</b>
<b>Résumé</b> .....	<b>xvii</b>
<b>Acknowledgment</b> .....	<b>xviii</b>
<b>Contributions of the Author</b> .....	<b>xix</b>
<b>Chapter 1: Introduction</b> .....	<b>2</b>
1.1 Historical evolution of materials.....	2
1.2 Natural materials.....	5
1.3 Architected materials.....	10
1.4 A brief theoretical background of segmented materials .....	12
1.5 Topologically interlocked materials (TIMs).....	14
1.6 Thesis objectives.....	15
1.7 Thesis organization .....	16
1.8 References.....	18
<b>Chapter 2: Strength and stability in architected spine-like segmented structures</b> .....	<b>23</b>
2.1 Abstract.....	23
2.2 Introduction.....	24
2.3 “Tabletop” experiments with dice .....	26
2.4 Instrumented experiments.....	27
2.5 Modelling the onset of sliding .....	31
2.6 Modelling the onset of hinging.....	37
2.7 Failure modes competition: sliding versus hinging .....	40
2.8 Geometrical enrichments .....	41
2.9 Summary .....	46
2.10 Acknowledgements.....	48
2.11 Appendix.....	48
2.11.1 Load analysis .....	48
2.11.2 Stress analysis .....	49
2.11.3 Pre-sliding behavior .....	49

2.11.4	Post sliding behavior.....	50
2.11.5	Finite element model of curved interfaces.....	51
2.12	References.....	51
<b>Link between chapter 2 and chapter 3.....</b>		<b>55</b>
<b>Chapter 3: Manipulating the geometry of architected beams for maximum toughness and strength.....</b>		<b>46</b>
3.1	Abstract.....	46
3.2	Introduction.....	47
3.3	Model setup and enrichment of cubes with fillets .....	50
3.4	Geometrical enrichments with polynomial functions .....	54
3.5	Optimization of monomials and binomials for finite strength of blocks .....	60
3.6	Experimental testing of architected ceramic glass .....	65
3.7	Summary .....	70
3.8	Acknowledgements.....	72
3.9	Appendix.....	72
3.9.1	Details of finite element model.....	72
3.9.2	Calculating the strength and toughness.....	73
3.9.3	Optimization of monomials and binomials.....	74
3.9.4	Preparing the ceramic glass samples.....	76
3.10	References.....	77
<b>Link between chapter 3 and chapter 4.....</b>		<b>80</b>
<b>Chapter 4: Three-Dimensional Laser Engraving for Fabrication of Tough Glass-Based Bioinspired Materials .....</b>		<b>82</b>
4.1	Abstract.....	82
4.2	Introduction.....	83
4.3	Laser-engraved interfaces: Fabrications and 3D morphology .....	85
4.4	An image-based damage parameter .....	87
4.5	Fracture toughness and fractography of engraved interfaces .....	88
4.6	Predicting the fracture toughness of engraved interfaces. ....	90
4.7	Example: Laser engraved architected panels.....	92
4.8	Summary.....	98
4.9	Acknowledgements.....	100
4.10	Appendix.....	100

4.10.1	Converting confocal images to binary images.....	100
4.10.2	Measuring the fracture toughness of engraved interfaces.....	102
4.11	References.....	103
<b>Chapter 5:</b>	<b>Conclusions .....</b>	<b>108</b>
5.1	Summary of the findings.....	108
5.2	Thesis contributions and accomplishment.....	109
5.3	Possible future directions.....	110
5.4	Publications.....	111
5.4.1	Refereed journals .....	111
5.4.2	Conference papers and presentations.....	112

# List of Figures

Figure 1-1: Evolution of materials from 10,000 until 2010. The plot is partly adapted from [7] until 2010, with some additional schematic projection, particularly after 2010 to highlight the prominence of architected materials and the emergence of bioinspired materials (was denoted in yellow as a combination of polymers and ceramics). ..... 3

Figure 1-2: (a) Ashby chart for Young’s modulus and toughness, data is adapted from [7]; (b) demonstrates how combining soft and hard materials produce superior composites, a strategy that is prominent in natural materials, data is adapted from [16]. ..... 6

Figure 1-3: Some examples of natural materials; (a) bones (adapted from [16] with permission by Springer Nature), (b) nacre image is adapted [23] with permission by Pixabay License; the microstructure image is adapted from [24] with permission by Elsevier, (c) fish fins (the microstructure is adapted and modified from [25] with permission by John Wiley and Sons), (d) shark jaws, (e) stingray teeth (adapted from [26]), (f) crocodile spine (adapted from [27] with free access, reuse rights). ..... 7

Figure 1-4: Types of architected materials: (a) composites; (b) sandwiched; (c) cellular and (d) segmented materials; this thesis examines segmented materials, so they are marked in red and with an asterisk (\*). Individual images are adapted from [18] with permission by Taylor and Francis. .... 11

Figure 1-5: Segmentation improves (a) damage resistance (resistance to crack propagation) and (b) energy absorption and deformability. The top images in (a) are adapted from [42] with permission by Royal Society of chemistry, and (b) is adapted from [48] with permission by Taylor and Francis. .... 13

Figure 1-6: Segmentation in (a) masonry structures; lintel image is adapted from [68] with permission by Elsevier; (b) topologically interlocked materials. .... 15

Figure 2-1: Examples of synthetic and natural architected materials: (a) Topologically interlocked materials (TIMs); (b) typical force-displacement response of architected materials versus monolithic materials. Linearly segmented architected materials in nature: (c) wings of a stingray fish: *Pteromylaeus asperrimus* (adapted from [33]) and (d) concavo-convex vertebrae in the crocodile spine (adapted from [38]). ..... 26

Figure 2-2: Simple experiments with rows of dice ( $N=2$  to 6). An axial pre-compression is applied with thumb and index fingers. The failure mode and the stability of the system can be assessed by applying a transverse force half-way along the dice row. .... 27

Figure 2-3: A segmented beam model and the experimental setup: (a) a row of cubes with sides of  $L \times L \times L$ , compressed from both ends with a force  $F_A$  and loaded halfway along the span  $S$  with a transverse force  $F_T$ ; (b) 3D printed cubes made from ABS polymer ( $L=5$  mm) arranged linearly and pre-compressed axially. A loading machine is then used to impose a transverse displacement half-way along the system and to record the corresponding force. .... 28

Figure 2-4: Experimental force-displacement  $F_T - u$  curve for the segmented cubes with different number of cubes ( $N= 3$  through 10), for  $f_s=0.18\pm0.02$ ,  $f_d=0.12\pm0.02$  and with axial pre-compression  $F_A=150$  N. The failure mode transitions from sliding to hinging as  $N$  is increased. .... 30

Figure 2-5: Critical sliding force  $F_T^{(s)}$  and hinging force  $F_T^{(h)}$  as function of (a) axial pre-compression  $F_A$  and (b) number of cubes  $N$ . .... 31

Figure 2-6: Load analysis for a row of 5 cubes showing the distribution of bending moment. ... 33

Figure 2-7: Maps of sliding ratio:  $|\tau_{xy} \geq f_s \sigma_{xx}|_{\max}$ , locations of the critical interfaces and experimental snapshots of the sliding cubes for (a) an odd case ( $N=5$ ) and (b) an even case ( $N=8$ ). .... 35

Figure 2-8: Comparisons of model predictions with experiments: (a) critical sliding force as function of the number of cubes and friction coefficient; (b) Force-displacement ( $F_T - u$ ) curves. .... 36

Figure 2-9: Distribution of the interface opening criterion:  $1+\sigma_{xx}L^2/F_A$  across the whole beam for (a) odd and (b) even cases. Snapshots of the experiment during hinging is shown below the contour plots to compare it with analytical predictions for the hinging points..... 38

Figure 2-10: (a) Critical hinging force  $F_T^{(h)}$  as function of number of cubes, model prediction and experiments; (b) snapshots of the hinging process, with the load lines highlighted..... 39

Figure 2-11: Deformations maps as function of the friction coefficient  $f_s$  and the number of cubes  $N$ ; (a) deformation map for odd and even cases; (b-c) comparison of the different combination of

$(N, f_s)$ with the actual experimental measurements at the onset of sliding for even cases and odd cases. ....	41
Figure 2-12: (a) Enrichment of the blocks with curved contact surfaces with various values of $CL$ (schematics of individual blocks and with corresponding 3D printed samples tested under transverse loading; (b) Force-deflection ( $F_T - u$ ) curves for different curvatures: $CL=L/R=0, 1/2, 2/3, 1, 3/2, 2$ . ....	43
Figure 2-13: (a) Example of a contact surface enrichment that prevents hinging in the case $N=10$ ; (b) Corresponding $F_T - u$ curve for flat case (hinged) and curved case (sliding); (c) deformed architected beam obtained using finite element method (FE) for the cases in (a); (d) $F_T - u$ curves obtained from FE. ....	44
Figure 2-14: Deformations maps obtained from FE simulations for different $(N, f)$ . Increasing the curvature $CL$ delays hinging. For each curvature, a deformed beam simulated using FE is shown for $(N=10, f=0.2)$ . ....	45
Figure 2-15: Strength $(F_T)_{\max} / EL^2$ as function of curvature $CL$ and for different friction coefficients $f$ . ....	46
Figure 2-16: Finite element model (FE). (a) meshed beam under axial pre-compression $F_A$ and transverse force $F_T$ ; (b) compare FE results with experiments for validation. ....	51
Figure 3-1: (a) Typical force–displacement curves of architected materials versus monolithic materials; (b) topologically interlocked materials (TIMs). Linearly segmented architected materials in nature: (c) fish fins of zebrafish (adapted from [40]), (d) vertebrae of orca (adapted from [32]), (e) concavo-convex vertebrae in the spines of crocodiles (adapted from [37]) and (f) goniatite (adapted from [34]). ....	49
Figure 3-2: (a) Finite element model: blocks are meshed and mesh refinement is applied at edges and corners; (b) the cube is enriched by rounding the edges and corners with fillets from $r/L=0$ to $r/L=0.5$ where finally the cube is transformed into a sphere. Effect of applying fillets $r/L$ on (a) $F_T - u$ curves and (b) deformation. ....	50
Figure 3-3: Normalized maximum principal stresses in the segmented beam during deformation; (a) stress contours in the blocks at $u/L=0.5$ for $r/L=0.3$ ; (b) maximum principal stress variation	

during deformation,  $(\sigma_1)_{\max} - u$  curves, the point of maximum stress is denoted by a red dot marker. .... 53

Figure 3-4: Toughness–strength map for segmented beams made of blocks with different rounding. .... 54

Figure 3-5: Enriching the contact surfaces between blocks with 2D-monomial functions. Pascal triangle depicting individual terms; the degree of the polynomial  $i+j$  increases from top to bottom. .... 55

Figure 3-6: Combining monomials to form binomials. .... 56

Figure 3-7: Force–displacement,  $F_T - u$  curves for (a)  $z(x) = a_{2,0}x^2$ , (b)  $z(y) = a_{0,2}y^2$  and (c)  $z(x, y) = a_{1,2}xy^2$ , (d)  $z(y) = a_{0,1}y + a_{0,2}y^2$  and (e)  $z(x, y) = a_{2,1}x^2y + a_{0,3}y^3$ ; the plots are reported for  $f=0.12$ . .... 57

Figure 3-8: (a) Normalized maximum strength  $F_{max}$  and toughness  $U_{max}$ ; (b) the geometric metric  $\phi L$  for different designs. Normalized (c) strength relationship and (d) toughness with  $\phi L$ . .... 59

Figure 3-9: Maximum principal stress during deformation for (a)  $z(x) = a_{2,0}x^2$ , (b)  $z(y) = a_{0,2}y^2$  and (c)  $z(x, y) = a_{1,2}xy^2$ . The plots are reported for  $f=0.12$ . .... 60

Figure 3-10: Optimization of (a) a monomial:  $z(y) = a_{0,3}y^3$  and (b) a binomial:  $z(x, y) = a_{2,1}x^2y + a_{0,3}y^3$  for  $\sigma_s/E = 10^{-4}$ ,  $10^{-3}$  and  $10^{-2}$ . The plots are reported for  $f=0.12$ . .... 61

Figure 3-11: Strength and toughness in an Ashby-like plot for (a)  $\sigma_s/E = 10^{-4}$  (blue), (b)  $\sigma_s/E = 10^{-3}$  (red), and (c)  $\sigma_s/E = 10^{-2}$  (grey). The plots are reported for  $f=0.12$ . .... 64

Figure 3-12: Deformations of ceramic glass beams during experiments for (a) monolithic beam and architected beams: (b)  $z(y) = 0$ , (c)  $z(y) = 0.5xy$ , (d)  $z(y) = 0.15y - 0.625y^2$  and (e)  $z(y) = 0.1875y - 1.0y^3$ . .... 67

Figure 3-13: Experimental data of monolithic and architected beams. (a)  $F_T - u$  curves and (b) strength and toughness plotted in an Ashby-like chart. For monolithic data, toughness calculated

by the total area under the  $F_T-u$  curve is denoted by a cross marker, and by the work of fracture it is denoted by a dash marker..... 69

Figure 3-14: Validation of the FE-model; (a) experimental force-displacement (denoted by black line and grey; the grey color is used to allow visualization of  $A/L=0$  case) curves compared with FE-model (denoted by a red line), (b) shows the deformation of architected beam with blocks having contact faces described by  $z(y) = a_{0,2}y^2$ , the deformed contour plots are compared side by side with experimental snapshots of the same design..... 73

Figure 3-15: Procedure for calculating the maximum strength and toughness based on the limits of the strength of blocks  $\sigma_s / E$ , (a) maximum principal stress  $(\sigma_1)_{\max}$  variation with displacement; displacement at the point of fracture can be found, here for example, displacement at fracture is  $u/L=0.2$  for  $\sigma_s / E = 10^{-3}$ ; (b) contour plot of  $(\sigma_1)_{\max}$  at the point of fracture; (c) force-displacement truncated,  $F_T-u$ ; (d)  $F_T-u$  truncated at the point of fracture, therefore toughness  $U_{\max}$  and strength  $F_{\max}$  are found. .... 74

Figure 3-16: Brute force optimization for the coefficients  $a_{i,j}$  such that the  $A/L \leq 0.5$  for (a) a monomial:  $z(y) = a_{0,3}y^3$  and (b) a binomial:  $z(x, y) = a_{2,1}x^2y + a_{0,3}y^3$  ..... 75

Figure 3-17: Experimental testing and fabrication of architected ceramic glass beams. (a) monolithic beam is laser cut into blocks; (b) experimental setup..... 77

Figure 4-1: (a) Nacre is a hard biological material where the interplay between micro-architecture and weak interfaces generate unique mechanisms and high toughness (adapted from [35] and [22]); (b) these concepts are inspiring new architected materials; (c) Ideal force-deformation curves for monolithic and architected material. .... 84

Figure 4-2: (a) Schematic of the engraved interface showing orientations, laser beam direction and microcrack spacing; (b) Confocal microscope images of an individual microcrack generated in borosilicate with a focused laser pulse; (c) Confocal images of engraved interface showing the microcracks distribution for  $s=100, 50, 20,$  and  $5 \mu\text{m}$ ..... 86

Figure 4-3: (a) Two examples of raw images from confocal microscopy converted to binary images using a thresholding technique; (b) The binary images were used to estimate a damage parameter  $\phi$ , plotted here as function of microcrack spacing  $s$ ..... 88

Figure 4-4: Experimental results for the fracture tests. (a) Relative fracture toughness  $K_{IC}^{(i)} / K_{IC}^{(b)}$  plotted as function of microcrack spacing for ceramic glass (red) and borosilicate glass (black); (b) Optical images of fracture surfaces for different microcrack spacing  $s$ . The macro-crack induced by the external load propagated from left to right along the  $x$ -direction. .... 89

Figure 4-5: Capturing the experimental model using an empirical model for (a) borosilicate glass and (b) ceramic glass. .... 91

Figure 4-6: (a) Laser engraving a  $7 \times 7$  grid pattern through the thickness of a monolithic glass panel to create an architected glass panel; (b) borosilicate glass panel before engraving (monolithic) and after engraving (architected). .... 92

Figure 4-7: (a) Experimental setup for impact testing of borosilicate glass panels and high-speed imaging; (b) impact force-displacement curve for monolithic and architected panels; (c) corresponding high-speed images and post mortem pictures; the red arrows indicate crack deflection and pinning (d) energy absorbed (in dark blue) and strength (in orange) of architected panels fabricated with different interface fracture toughness. .... 94

Figure 4-8: (a) Schematic and pictures of the sandwiched architecture glass panel; (b)  $F-u$  curves for monolithic panel and sandwiched panels; (c) high speed snapshots during impact at  $u=0, 0.2, 0.6$  mm, with post mortem images; (d) summary of all tests results on an Ashby like plot for strength-energy absorbed. .... 97

Figure 4-9: Thresholding of raw confocal images. (a) raw confocal image (first column) and their frequency histogram, challenging regions are indicated by red circles; (b) binary images generated by 3 different thresholding algorithms: mean, Ostu and Phansalkar. .... 101

Figure 4-10: Fracture toughness test for the engraved interfaces: (a) schematic of the engraved interface in front of a sharp notch; (b) a bend fracture sample mounted in a 3-point bending test configuration; (c) load-displacement curve showing the critical load  $P_c$  at fracture, where the inset shows the sample after fracture. .... 103

# List of Tables

# Nomenclature

$J_i$	: Energy release rate at interfaces
$\sigma_a$	: Apparent strength of segmented materials
$\sigma_s$	: Apparent strength of non-segmented materials, strength of individual blocks
$K_{IC}$	: Fracture toughness of non-segmented sample (monolithic sample)
$K_{IC}^{(b)}$	: Fracture toughness of bulk glass
$K_{IC}^{(i)}$	: Fracture toughness of laser engraved interfaces
$a$	: Crack size
$G_d$	: Energy release rate to crack deflection
$G_p$	: Energy release rate to crack penetration
$\Gamma_i$	: Toughness of interfaces
$\Gamma_I$	: Toughness of tablets (segments)
$P_s$	: Survival probability of brittle materials
$P_f$	: Probability of failure of brittle materials
$D$	: Probability of damage of individual blocks
$V_o$	: Materials constant for Weibull probability expression
$\sigma_o$	: Material constant for Weibull probability expression
$m$	: Weibull exponent for brittleness
$n$	: Number of segments, empirical constant
$V$	: Volume of the material
$\sigma$	: Applied stress
$N$	: Number of blocks
$L$	: Side length of blocks
$E$	: Young's modulus
$F_A$	: Axial precompression force

$F_T$	: Transverse force
$S$	: Half span of beams
$f, f_d$	: Dynamic friction coefficient
$f_s$	: Static friction coefficient
$F_Y$	: Yield force
$R$	: Indenter nozzle radius, curvature radius, reaction forces
$u$	: Transverse displacement
$F_T^{(s)}$	: Critical force at sliding
$u^{(s)}$	: Displacement at critical sliding force $F_T^{(s)}$
$F_T^{(h)}$	: Critical force at hinging
$M(x)$	: Moment as function of $x$
$M_{\max}$	: Maximum moment
$M_{\min}$	: Minimum moment
$\sigma_{xx}$	: Normal stress along $x$ -direction
$\sigma_1$	: Tensile principal stress
$(\sigma_1)_{\max}$	: Maximum tensile principal stress
$\tau_{xy}$	: Shear stress on $x$ - $y$ plane
$C$	: Surface curvature, combinations (statistical concept)
$F_{\text{interface}}^{(s)}$	: Coulomb's sliding force
$\nu$	: Poisson's ratio
$r$	: Fillets radius
$U_{\max}$	: Maximum energy absorbed (toughness)
$F_{\max}$	: Maximum transverse force (Strength)
$z(x, y)$	: Polynomial function for transforming contact faces of blocks at $x$ - $y$ plane
$a_{i,j}$	: Coefficients of polynomial function $z(x, y)$
$x_{\max}, y_{\max}$	: Location of maximum point on $z(x, y)$

$x_{\min}, y_{\min}$	: Location of minimum point on $z(x, y)$
$i, j$	: Indexes
$A$	: Amplitude of $z(x, y)$ .
$\phi$	: Surface curvature (“waviness”), damage parameter
$s$	: Spacing between laser induced microcracks
$A_c$	: Total cracked area of laser engraved interfaces
$A_l$	: Total ligament area of laser engraved interfaces
$p, q$	: Empirical constants
$R^2$	: Residuals
$F$	: Impact force for glass panels

# Abstract

Architected and segmented material designs have recently emerged as a powerful approach to high strength and toughness. These materials are made of regular building blocks that can collectively slide, rotate, separate or interlock, providing a wealth of tunable mechanisms. The properties of architected materials can be tuned with geometry, surface morphology, friction and adhesion between the blocks. This article-based dissertation is organized in three main chapters: First we use experiments and modeling to explore the strength and the stability of idealized segmented systems made of a linear array of cubes subjected to axial pre-compression and to a transverse force. We highlight two failure modes in this segmented system: sliding and hinging. The transition between these modes depends on the number of blocks and on friction coefficient, but it is independent of axial compression. In the next chapter, we show how the stiffness, strength and failure mode of this system can be manipulated with the 3D shape of the blocks. For example enriching the morphology of the cubes with curved interfaces (akin to the vertebrae in the spine of reptiles) delays hinging and improves stability. Using finite elements models we identify optimum block geometries, which we then tested on architected beams made of blocks of ceramic glass carved with a pulsed laser beam. Unlike monolithic glass, architected glass fails gracefully exhibiting progressive deformation, resulting in 370 times increase in toughness relative to monolithic glass. Finally, we explore in more details three-dimensional laser engraving as a way to create architectures within glass. We characterize the morphology of individual microcracks, arrays of cracks and engraved interfaces using confocal microscopy. We also assess how laser engraving parameters govern the interface toughness and found optimum microcrack spacings. We then implement these results in architected borosilicate glass panels based on a simple grid pattern. These all-brittle panels do not require mechanical confinement, and they absorb significantly more impact energy than monolithic glass, provided that the interface toughness is tuned properly. Using plain glass as front and back layers provided additional reinforcement and confinement of the architected layer, which further increased strength and energy absorption.

# Résumé

Les matériaux architecturés et segmentés sont récemment apparus comme une nouvelle stratégie pour produire de la haute résistance et de la ténacité. Ces matériaux sont fabriqués à partir de « blocs de construction » pouvant glisser, pivoter, se séparer ou s'emboîter de manière collective, offrant ainsi une multitude de mécanismes. Les propriétés des matériaux architecturés peuvent être ajustées en jouant sur la géométrie, la morphologie des surfaces, le frottement et l'adhérence entre les blocs. Cette dissertation, basée sur des articles, est organisée en trois chapitres principaux: Nous utilisons d'abord des approches théoriques et expérimentales pour explorer la résistance et la stabilité de systèmes segmentés idéalisés constitués d'un arrangement linéaire de cubes soumis à une pré-compression axiale et à une force transversale. Nous mettons en évidence deux modes de défaillance dans ces systèmes segmentés: le glissement et le pivotement. La transition entre ces modes dépend du nombre de blocs et du coefficient de frottement, mais nous démontrons qu'elle est indépendante de la compression axiale. Dans le chapitre suivant, nous montrons comment la rigidité, la résistance et le mode de défaillance de ce système peuvent être manipulés en jouant sur la géométrie des blocs. Par exemple, enrichir la morphologie des cubes avec des interfaces courbes (semblables aux vertèbres de la colonne vertébrale des reptiles) améliore la stabilité mécanique. En utilisant des modèles d'éléments finis, nous identifions les géométries de blocs optimales, que nous avons ensuite testées sur des poutres architecturées constituées de blocs de verre céramique taillés avec un faisceau laser. Contrairement au verre monolithique, le verre architecturé présente une déformation progressive gracieuse qui se traduit par une augmentation de la ténacité de 370 fois supérieure à celle du monolithique. Enfin, nous explorons plus en détail la gravure laser tridimensionnelle comme moyen de créer des architectures dans le verre. Nous caractérisons la morphologie des microfissures individuelles, des réseaux de fissures et des interfaces gravées à l'aide de la microscopie confocale. Nous évaluons également la manière dont les paramètres de gravure au laser régissent la ténacité de l'interface et permettent de déterminer les espacements optimaux des microfissures. Nous implémentons ensuite ces résultats dans des panneaux de verre au borosilicate architecturés basés sur un simple motif en grille. Ces panneaux ne nécessitent pas de confinement mécanique et absorbent beaucoup plus d'énergie d'impact que le verre monolithique, à condition que la ténacité de l'interface soit correctement réglée. L'utilisation de verre ordinaire comme couches avant et arrière permet de renforcer et de confiner la couche architecturée, ce qui accru encore la résistance et l'absorption d'énergie.

# Acknowledgment

*In the name of God, the Most Gracious, the Most Merciful*

This journey was very rewarding. I have met many wonderful people. I am very grateful to Prof. Francois Barthelat, my PhD supervisor for his active and sincere supervision. From Prof. Barthelat, I learned patience and the art of distilling ideas to its simplest, purest form without compromising rigorousness. I thank him for accepting me in his research group and giving me this chance to pursue my PhD at McGill University.

My hearty gratitude goes to Prof. Rashid K. Abu Al-Rub (My master's supervisor at Khalif University) for his encouragement and continuous guidance in academic and non-academic settings. I reflect back and I remember Prof. Shivakumar Ranganthan (Virginia tech.), my undergraduate teacher and mentor who had ignited my spark of research, his input has been instrumental in kickstarting my research career.

During my PhD I had to troubleshoot lab issues which naturally increased my interaction with the mechanical engineering department administration, that amassed a team of wonderful professionals; they were always ready to provide help and support. Here I thank a few that I interacted with: Anne-Marie Pierre, Shirley Baxendale, Connie Greco, Gregory Doyle and Prof. Meyer Nahon. I would like also to thank Jamil Ahram (the workshops manager), it has been a pleasure working with him as a workshop facilitator. During my work as a teacher assistant, I have worked with the finest of professors, I thank: Prof. Arun K. Misra, Prof. Jianyu Li and Prof. Pascal Hubert who has been especially supportive.

I would like to extend my gratitude towards my committee members: Prof. Larry Lessard (internal member) and Prof. David Restrepo (external member) for accepting to evaluate my PhD dissertation and for their comments. My thanks go also to Prof. Allen Ehrlicher for his constructive comments and ideas in my proposal presentation and for granting access to his microscopy facility at his lab. I also thank my PhD committee members: Prof. Pascal Hubert, Prof. Jozsef Kovacs and Prof. Colin Rogers.

I thank my current and former lab members: Dr. Najmul Abid, Dr. Mohammed Mirkhalaf, Dr. Florent Hannard, Dr. John William Pro, Zhen Yin, Aram Bahmani, Abdulrahman Almessabi, Siyu Liu, Sacha Cavelier, Idris Malik, Alireza Mirmohammadi, Ali Shafiei. I would like to extend my gratitude to my friends here in Canada, USA and express nostalgia for the good times with my friends in UAE.

My special gratitude and love go to Sharifa, my mother for the emotional support that she provided. Her everlasting affection that she projects is unrivaled. I am also grateful for my father's support, he has been the sanity check for my crazy endeavors, he was and remains the go-to person for advice. I also thank my three sisters: Deemah, Alaa and Duaa for their love.

Ahmed S. Dalaq  
Montreal, Canada  
December 2019

# Contributions of the Author

This is a manuscript-based thesis which consists of three journal articles. The title of the articles, name of the authors, and their contributions are listed below:

## **1) Strength and stability in architected spine-like segmented structures (published)**

Ahmed S. Dalaq and Francois Barthelat

Department of Mechanical Engineering, McGill University, 817 Sherbrooke Street West, Montreal, QC H3A 2K6, Canada

Published in the *International Journal of Solids and Structures* (IJSS), Volume 171, 15 October 2019, Pages 146-157.

### ***Author contributions:***

ASD: Developing the analytical model, the computational model and conducted the experiments, ran simulations, analyzed data, prepared figures and manuscript.

FB: Supervised the research and review process, gave technical and scientific advice, guided the development of the analytical model, computational model, experimental methodology and edited the figures and the manuscripts.

## **2) Three-Dimensional Laser Engraving for Fabrication of Tough Glass-Based Bioinspired Materials (published)**

Ahmed S. Dalaq<sup>1</sup>, Francois Barthelat<sup>\*1,2</sup>

1: Department of Mechanical Engineering, McGill University, 817 Sherbrooke Street West, Montreal, QC H3A 2K6, Canada

2: Department of Mechanical Engineering, University of Colorado, 427 UCB, 1111 Engineering Dr, Boulder, CO 80309, United States.

Submitted to *The Journal of The Minerals, Metals & Materials Society (JOM)*, special issue: Advanced Manufacturing for Biomaterials and Biological Materials. (recommended for publication after first round of review)

### ***Author contributions:***

ASD: Developing the analytical model and conducted the experiments, analyzed data, prepared figures and manuscript.

FB: Supervised the research and review process, gave technical and scientific advice, guided the development of the analytical model, the experimental methodology and edited the figures and the manuscripts.

**3) Manipulating the geometry of architected beams for maximum toughness and strength (submitted)**

Ahmed S. Dalaq<sup>1</sup>, Francois Barthelat\*<sup>1,2</sup>

1: Department of Mechanical Engineering, McGill University, 817 Sherbrooke Street West, Montreal, QC H3A 2K6, Canada

2: Department of Mechanical Engineering, University of Colorado, 427 UCB, 1111 Engineering Dr, Boulder, CO 80309, United States.

submitted to *Materials and Design* (JMAD).

***Author contributions:***

ASD: Developing the computational model and conducted the experiments, ran simulations, analyzed data, prepared figures and manuscript.

FB: Supervised the research and review process, gave technical and scientific advice, guided the development of the computational model, experimental methodology and edited the figures and the manuscripts.

---

# Chapter 1

## Introduction

---

# Chapter 1: Introduction

## 1.1 Historical evolution of materials

The history of humans is tied to materials, so much so that entire eras are named according to names of materials. Even in non-materials contexts, terms such as the stone age, golden age, copper age and bronze age are prominent in social sciences and geography. Figure 1-1 shows the evolution of materials demand and their relative importance with time. Figure 1-1 is composed of four areas: metals (denoted by red), polymers (denoted by blue), composites (denoted by green) and ceramics (denoted by orange), which are the four main types of materials. The extensions after the date 2010 on Figure 1-1 are schematic projection that are not based on data but are based on the author's vision. The historical discussion in this section will follow a chronological order.

It all started with stones, around 10,000 B.C.E, early humans smashed bulky stones with bulkier ones to form smaller more portable and hence useful pieces. With time, humans realized that harder objects can shape softer ones [1]. As a result, obsidian, a naturally occurring glass near volcanic sites was extensively used to shape stones, wood, skins and fibers to form tools and shelters [2, 3]. Straw-reinforced mud which is one of the earliest form of composite was developed in parts of Africa for building homes [4] (see early part of the green area on Figure 1-1). The discovery of the clay artifact of “Venus of Vestonic” in Czech Republic, which dates back to 23,000 B.C.E suggested that the art of making pottery coincided with the stone age [1]. With regards to metals, the discovery of an intricate oval shaped copper artifact in northeast Iraq (Shanidar) dating back to 9500 B.C.E [3], suggested that shaping of copper ores was developed back then. However, it is only when the kiln furnace was essentially developed for pottery, around 3500 B.C.E, that smelting of copper from azurite (a natural ore of copper) began [4] (see red area on Figure 1-1). A major step that ushered in the copper age. However, humans have quickly learned that copper is soft. It is unknown how precisely bronze was made. Perhaps accidental alloying of copper with tin and arsenic may have jumpstarted the bronze age [1]. In the Middle East and Thailand, several bronze objects were unearthed dating back to  $\approx$ 4000 B.C.E [1]. Around the same time, Roman historian Pliny reported that an accidental experimentation with sand, fire and lime around Syria led to the formation of glass [5] (see orange area on Figure 1-1). Around 1450 B.C.E, bronze became

obsolete which was substituted by iron. Available furnaces then, were unable to melt iron, instead a spongy malleable form was beaten to various shapes [4]. Around 500 B.C.E, in India, near Kerala a new high carbon steel known as Wootz steel was developed [6].

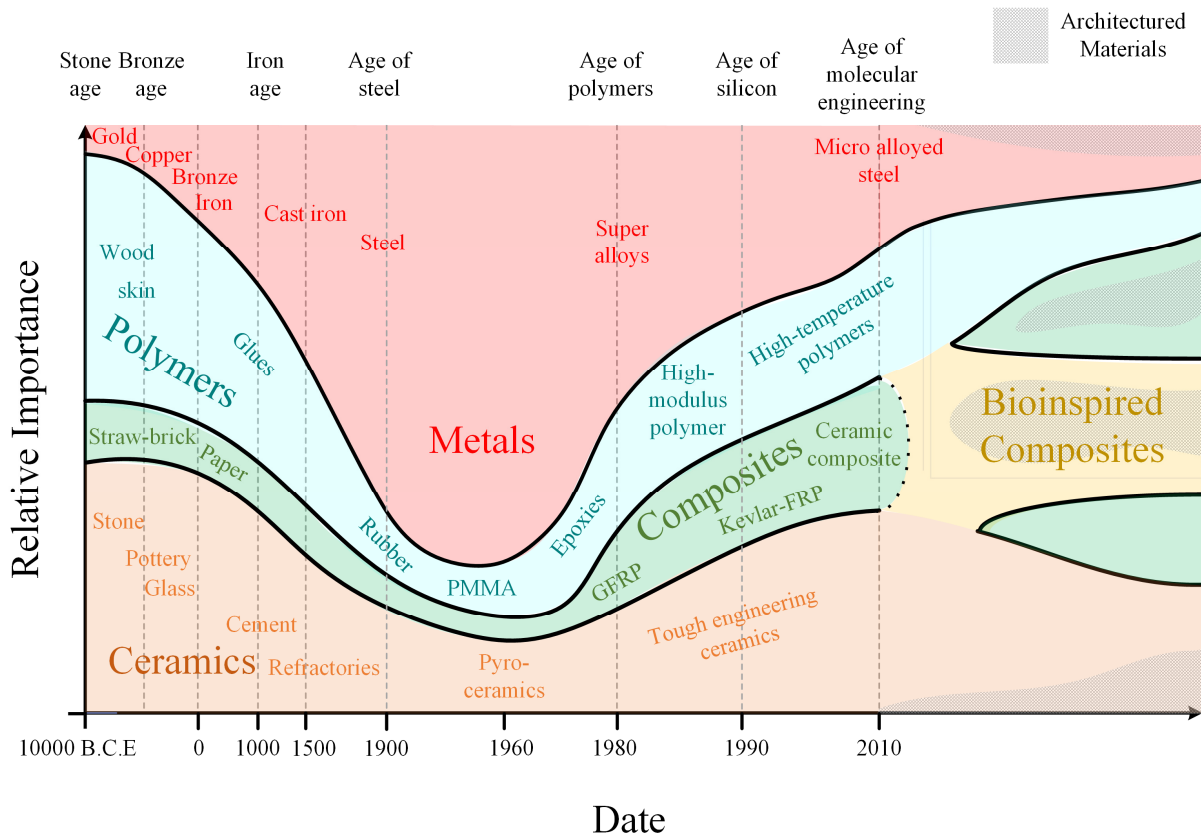


Figure 1-1: Evolution of materials from 10,000 until 2010. The plot is partly adapted from [7] until 2010, with some additional schematic projection, particularly after 2010 to highlight the prominence of architected materials and the emergence of bioinspired materials (was denoted in yellow as a combination of polymers and ceramics).

Approaching 0 CE, the use of sticky glue from plants for assembly of complex tools became prevalent. Around the same time, the Romans were mastering the iron work. In Asia, China was inventing paper (a textile based fiber), which revolutionized documentation that also paved the way for printing [8]. Through trade routes, Arabs imported the Indian ingots to Damascus and with years of refinements developed the well-known Damascus steel [9]. The next major step is iron casting, which required high temperatures up to 1500 °C, only became achievable by the advent

of the blast furnace around 1500 C.E [4]. It is after 1500 C.E that the relative importance of metals increased dramatically (follow the red area on Figure 1-1). Operating at such high temperatures required thermally resistive materials, and hence the emergence of refractories. With the discovery of the new world (the Americas), around 1550 C.E, rubber is introduced to Europe [10]. Around 1800 C.E, the Bessemer process facilitated the production of steel, making steel the dominant structural engineering material. After which there was a rush towards alloying different metals to create stronger and thermal resistant ones, a class of alloys that became known as super alloys (Figure 1-1). Steel became the go-to material for various uses spanning from buildings, infrastructure, transportation, to military.

The development of Bakelite (a polymer) in 1909 marked the beginning of a polymer revolution [11]. During which, polymer science developed rapidly, resulting in the generation of new types of polymers such as nylon and polyurethane (PE), polyvinyl chloride (PVC) and polyurethane (PU) [4, 10]. At the same time, around the mid 1900's, more effective forms of cements started to surface. It also coincided with the emergence and the spread of pyro ceramics [7]. Still within the class of ceramics, the aerospace and aeronautics sectors demanded strong, tough and thermally resistant materials. Two of which ceramics can already provide, namely strength and thermal resistance [12]. In addition, Aerospace industry also demanded multifunctional materials that combine lightweight, strength and damage tolerance in a single material. Therefore, engineers revived the prehistoric strategies used in making straw-reinforced bricks to form modern composites. Accordingly, fiber and particulate composites emerged. In the year 1940 C.E, glass fiber reinforced polymer (GFRP) is employed in aircrafts [4]. By 1940, the rush for alloys persisted, but shifted attention to light alloys.

By 1960, the boundaries between materials are becoming fuzzy. Engineers more than ever realized that combining different constituents is a key strategy to enhance properties of materials. Between 1960-2000, the metallurgist and polymer scientists are pushing boundaries forming super alloys, PMMA, epoxies, polystyrene, high modulus polymer, high-temperature polymer and Kevlar [4, 7]. Concurrently and in the search for tough ceramics; metals were introduced to ceramics to impart it with ductility [13, 14]. By 2010, strategies for strong, tough, light, biodegradable, biocompatible and thermal resistant natural materials were postulated [15, 16]. It actually directed attention back to nature as a source of inspiration. Nature has mastered the art of forming strong and tough

materials from brittle constituents [16]. Natural materials generally are made from polymers and ceramics fused together ingeniously over several length scales in various architectures [17]. Essentially both bioinspired materials as well as traditional composites are basically formed from a combination of two or more types of materials, so they are classified as composites. Therefore, the blue polymer area was merged with the orange ceramics area to form a yellow area that indicates the bioinspired composites (Figure 1-1). An added key element to the design of modern materials is architecture (denoted by a grey mesh over the different regions on Figure 1-1), specifically it represents general geometrical features in materials at any length scale. Geometrical changes within the material can have profound effects on the mechanical, physical, electrical and thermal properties of materials [18, 19]. In parallel to bioinspiration, traditional design of materials is indispensable, where manipulation of microstructure (metallurgy), molecules and atoms (chemistry) of matter for better material properties remain vital in the quest for new materials [4].

## 1.2 Natural materials

The advent of advanced characterization techniques such as optical, confocal, scanning electron (SEM), focus ion beam (FIB), atomic force (AFM) and transmission electron microscopes (TEM) revealed intriguing details of natural materials that were previously hidden. Such realizations accelerated the process of bioinspiration. To see how natural materials compare with synthetic ones, Ashby charts was used. Ashby charts are an elegant presentation of materials properties [7]. Figure 1-2a shows an Ashby chart for Young's modulus and toughness for a variety of materials. Metals are denoted with red, while synthetic composites, polymers and ceramics are denoted with green, blue and orange, respectively. Natural materials are denoted by dark grey.

There is a direct relationship between strength and Young's modulus, so the abscissa of Figure 1-2a is indicative of strength too [20]. The property space of Young's modulus/strength and toughness, for example, though theoretical limits included, still contains holes (vacant spaces) [18]. These vacant holes are clear incentives for designing tougher and stronger materials that could serve multiple functions, which thereby form multifunctional materials. Nevertheless, strength and toughness are a well-known mutually exclusive set of properties (i.e. difficult to achieve both) [21]. For example, weak materials such as polymers are tough, while strong

materials such as glass are brittle (Figure 1-2a). Another example, flexible materials have low response time, which limit their use in micro-electro-mechanical systems (MEMS). Natural materials combined mutually exclusive properties effectively, most notably strength and toughness (Figure 1-2a). Clearly, increased strength/Young's modulus does not have the sharp decrease (black trend line on Figure 1-2a) in toughness as that of the synthetic materials (red trend line on Figure 1-2a). See for example mollusk shells and bones, both of which are prime examples of combined mutually exclusive properties in nature. Left alone, these materials can selfheal. In contrast, synthetic materials follow a very sharp decreasing trend with the slightest increase in Young's modulus, with limited to no self-healing capabilities. Natural materials may indeed offer some solutions for the material of the future. Here therefore some of the strategies present in natural systems that endows it with such remarkable property tradeoffs were examined.

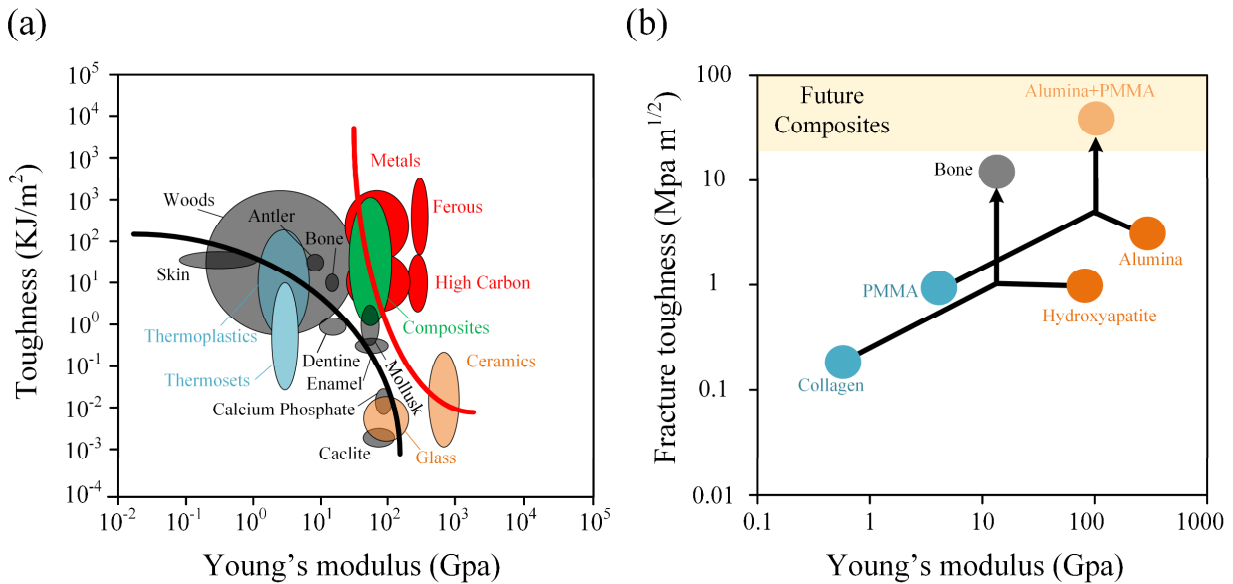


Figure 1-2: (a) Ashby chart for Young's modulus and toughness, data is adapted from [7]; (b) demonstrates how combining soft and hard materials produce superior composites, a strategy that is prominent in natural materials, data is adapted from [16].

Segmentation and architecture in natural materials is ubiquitous. With diverse motifs (design elements) shaped over millions of years to meet survival and/ or functional requirements [22]. These motifs are formed bottom up through organized synthesis from atomic, nano-, micro-, meso- all the way to the macro-scale. To the extent that some natural systems have developed a hierarchal structure as in bone.

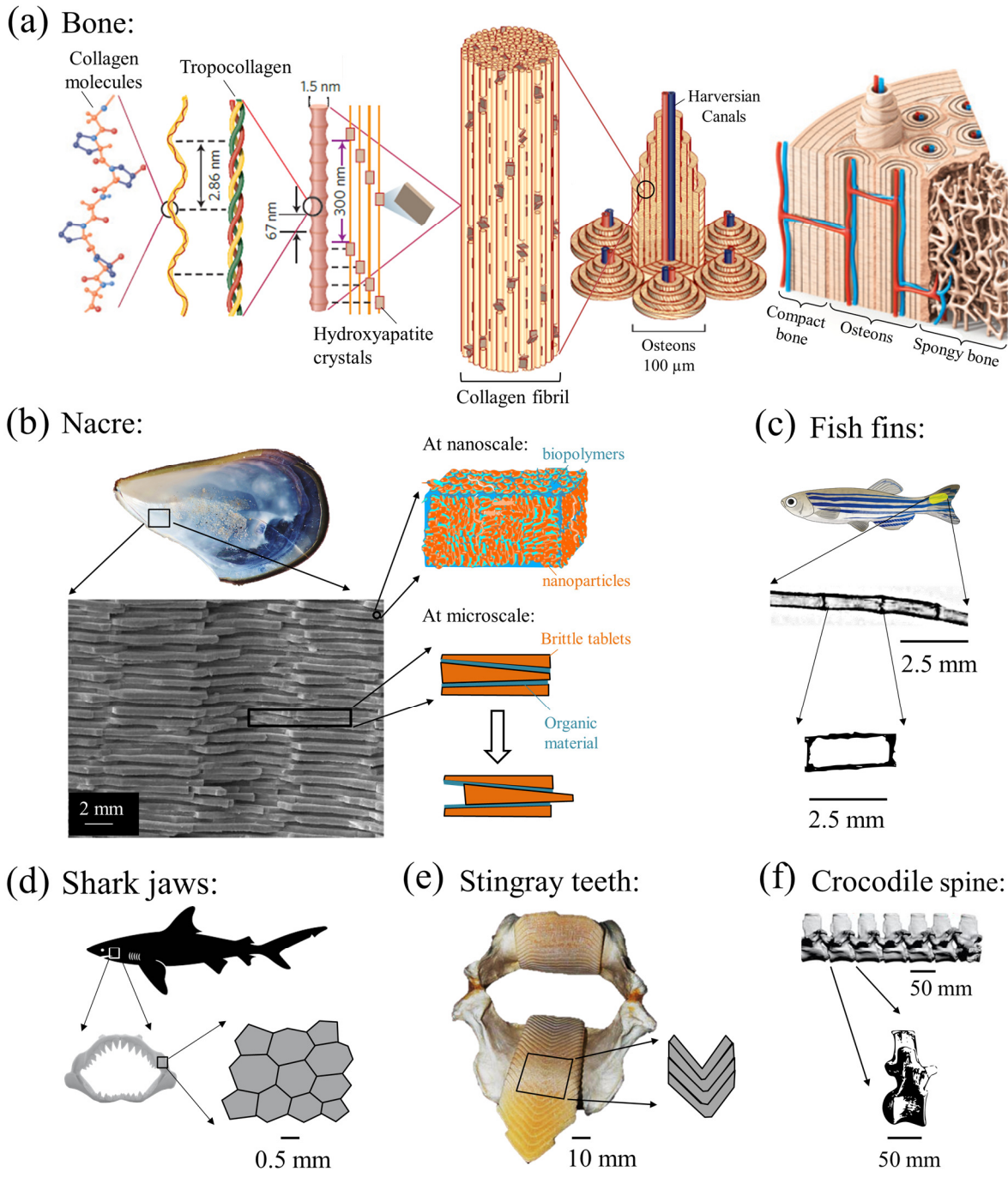


Figure 1-3: Some examples of natural materials; (a) bones (adapted from [16] with permission by Springer Nature), (b) nacre image is adapted [23] with permission by Pixabay License; the microstructure image is adapted from [24] with permission by Elsevier, (c) fish fins (the microstructure is adapted and modified from [25] with permission by John Wiley and Sons), (d) shark jaws, (e) stingray teeth (adapted from [26]), (f) crocodile spine (adapted from [27] with free access, reuse rights).

Generally, at the atomic scale, natural materials are mainly formed of organic components such as chitin, cellulose, collagen, keratin, lignin and water. Skins and tendons possess remarkable toughness, particularly because of collagen. Inorganic materials such as calcium carbonate, calcium phosphates, iron oxides and silica are also prominent basic constituents that are brittle. Yet nature found ways to form strong and light materials from such limited options: brittle constituents and weak compliant organic materials (Figure 1-2b). It does that partly by virtue of architecture and specific geometrical arrangement(s) [17, 28, 29] or gradient variation of material composition [22].

Take for example bone, it has 7 levels of structural hierarchy (Figure 1-3a). At the atomic level, amino acids intertwine in helical formations, forming a tropocollagen structure that in turn is arranged in a staggered fashion [30]. This results in a highly regular staggered helixes bundled into collagen fibrils. These fine details were detected by TEM imaging at the scale of nanometers (nm), around  $\approx 67$  nm. Mechanically, the tropocollagen chain shows almost a linear force displacement curve upon tensile loading, which is a spring-like behavior. Conversely, the collagen fibrils show a typical curve often displayed by polymer chains where they uncoil resulting in slow increase in force, ending with a sharp increase attributed to the stretch of fibrils backbones [30]. In addition, bone is a prime example of a nanocomposite, inorganic nanocrystals known as hydroxyapatite are fused and distributed in a periodic staggered formation along the collagen fibers [31, 32] (Figure 1-3a). At 100-300 nm, these mineralized fibrils bundle together to form collagen fibers forming sheets (at scale of 100  $\mu\text{m}$ ) that wrap in concentric layers to form osteons, a cylindrical structure. At the macroscale, bones display three regions where the outer region form compact bones, a middle one that is composed of osteons and an inner region that is formed of cancellous bones. Essentially the cancellous bone region is a form of cellular materials [32, 33]. Interestingly, examination of bone alone has revealed almost 7 architectures, from helixes of collagens molecules, arrangement of fibrils, fibers, lamella sheets, osteons to the three regions of bones (Figure 1-3a). When bone is subjected to mechanical loads, all these architectures work in concert, spanning from the successive breakage of hydrogen bonds of tropocollagen chains, uncoiling of collagen molecules, sliding of fibrils, the multiple crack resisting mechanisms (both extrinsic and intrinsic) of osteons [16, 34] to the energy absorbing light cellular core of bones at the macroscale [35], all of which cascade to the macroscale level, giving bone the superb damage tolerance that is unmatched by synthetic materials.

The above qualities are not exclusive to bones, microstructures of several natural materials are highly architected [17, 28]. In nacre (mollusk shell) for example, the microstructure is arranged in a 3D brick and mortar fashion [36, 37] (Figure 1-3b). The blocks are made of polygonal aragonite tablets (a brittle material) that are separated by organic materials. In addition, the tablets themselves are composed of nanograins formed of biopolymer matrix fused with nanoparticles (Figure 1-3b). Overall, the organic material in nacre is 5% of the volume fraction, making it a highly mineralized material with almost 95% of mineral content [24]. The strong, stiff tablets along with the architecture, together with soft organic materials between tablets enable sliding of blocks and inelastic deformations at the tablet's interfaces, which are powerful mechanisms for energy dissipation. In addition, some interfaces are wavy and/or tapered where blocks undergo jamming upon sliding [16, 17] (Figure 1-3b). This jamming induces hardening that improves the overall strength of the material. In addition, crack growth is pinned at the interfaces with the possibility of multiple crack deflections, resulting in a series of crack bridging behind propagating cracks [16, 17, 38, 39]. Collective sliding in front of crack tips generate a large process zone that is similar to that of ductile materials [39]. These are some of the mechanisms that impart toughness and strength in nacre making it among the toughest natural materials. The mechanical property of nacre may not be higher than some of the current synthetic materials in the market, but certainly it has superior property tradeoff (Figure 1-2a). Another major example of segmented materials at microscale is fish fins. Examination of fish fins revealed mineralized blocks bonded by organic materials arranged in a linear array [40, 41] (Figure 1-3c). This structure allowed the fish to morph its fins and modulate their stiffness for maneuvers that range from sudden breaks, accelerations and rapid reorientation [41].

Segmentation is also present at the macroscale. For example, jaws of sharks are covered by layer(s) of mineralized tablets known as tesserae in pavement-like arrangement [42] (Figure 1-3d), forming an organized mosaic that serve as armor and modulates the body stiffness of the shark, giving sharks springiness in its body for fast pursuit. Some aggressive sharks that typical consume hard materials build up to 6 layers of armor [43]. Stingrays and its close relatives have flat teeth that are made from interlocking tablets, padding the interior of their mouth in a pavement like arrangement [42] (Figure 1-3e). Generally, in animals, spines are formed from vertebrae arranged in linear formation [44] (Figure 1-3f). Different conditions and environments led to various spine shapes as well as different vertebral morphology [27, 45]. For example, the vertebrae of mammals

tend to have a straight morphology, whereas reptiles have a round articulation, almost similar to a ball-socket connection (Figure 1-3f). They therefore provide flexibility, strength, and agility to reptiles [45]. Typically, the blocks in natural materials are stiff and hard so they undergo small elastic deformations and they are order of magnitudes stronger than its organic matrix, around 1-5 times stronger [30]. Finally, Nature offer myriads of architectures, arrangements and morphologies, each of which is a standalone aspect that requires a thorough investigation for effective implementation in synthetic materials.

### 1.3 Architected materials

Architected materials emerged as a powerful alternative that can fill holes in the property space [18]. Architected materials are typically divided into composites (Figure 1-4a), sandwich structures (Figure 1-4b), lattices (Figure 1-4c) and the less studied one: segmented materials (Figure 1-4d) [18]. Architected materials are simply made from unit blocks with specific geometric features designed for specific loads. Loads can be thermal, electrical, and mechanical. The materials can be tailored to serve multiple functions. Take for example, lattices which are largely made of air along with a small fraction of solid struts [10, 18]. The struts resist the loads, while the air, being a poor conductor of heat and sound can provide thermal and acoustic isolation respectively [18, 46]. Interestingly these properties are tunable by changing the volume fraction of the struts relative to air, or by changing the physical properties, the mechanical properties and the morphology of the struts. As such, designers have unlimited design options and material combinations for architected materials. Segmented materials are the primary focus of this thesis (Marked in red and asterisk \* on Figure 1-4d). Segmented materials were primarily conceived to impart damage tolerance to materials [17, 47], especially for brittle materials that lack toughening mechanisms. The blocks in segmented materials interact by sliding, separation, interlocking and/or jamming [47, 48]. The geometry of blocks controls the interaction between them as well as the overall performance of the material (the component). The interface between blocks can deflect and pin propagating cracks, should crack growth occurs due to excessive loads [49, 50]. Crack pinning is an advantage over monolithic materials, where crack growth occurs with little resistance which

results in a catastrophic failure. In addition, damaged blocks in segmented materials can simply be replaced with new ones with minimal disruption to its function during service [51].

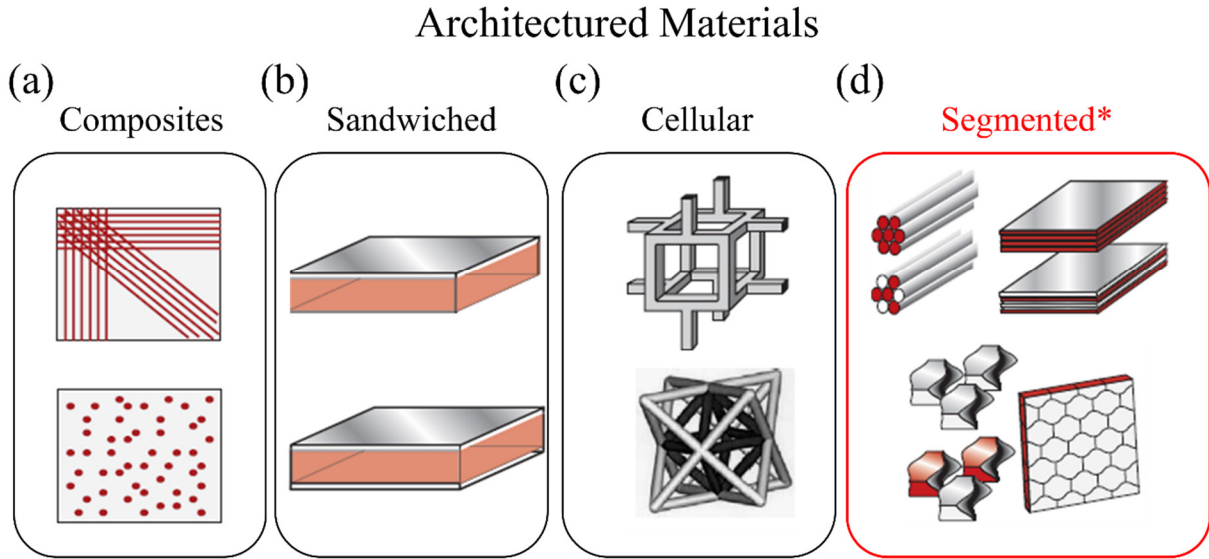


Figure 1-4: Types of architected materials: (a) composites; (b) sandwiched; (c) cellular and (d) segmented materials; this thesis examines segmented materials, so they are marked in red and with an asterisk (\*). Individual images are adapted from [18] with permission by Taylor and Francis.

Apart from damage tolerance, these segmented materials are information rich. They offer a plethora of design variables: arrangements of blocks, block morphology, interface geometry, interface material properties, number of blocks, all of which can be optimized for various applications. As such different combination of these design variables may unlock programmable crack paths, desired stress-strain curves (constitutive models), desired overall behavior where mechanical softening, hardening, and deformability are tuned. Through various geometric designs; multiple stability configurations can be imparted into materials, enabling for example a behavior that is similar to phase transformation. Segmentation is scalable for different applications and applicable to one or more scales that may form hierarchal structures [52]. Segmented materials are therefore ideal candidates for robotics, armors, shields, glass facades, deployable structures and anti-seismic materials [17, 53]. Artists can also make use of such systems to actualize segmented sculptures and designs. The segments in such materials can be actuated into various shapes and

deformation modes, which makes them not only multifunctional, tough and damage tolerant, but also smart materials.

#### 1.4 A brief theoretical background of segmented materials

It was found that the inhomogeneous lamellar arrangement reduces the energy release rate  $J_i$ , meaning that less energy is available for crack propagation [42, 54]. In the case of a discontinuous lamellar arrangement of layers, the crack stops at the interfaces where the crack has to nucleate at each interface in order to propagate. Also, the apparent strength  $\sigma_a$  of a non-segmented material falls exponentially as the crack size  $a$  increases following:  $\sigma_a = K_{IC} / \sqrt{\pi a}$ , where  $K_{IC}$  is the toughness of the monolithic sample. Conversely, the presence of a crack in a lamellar segmented material reduces the strength of the material  $\sigma_a$  linearly following:  $\sigma_a = (1 - 2W/a)\sigma_s$  which shows how the segmented material is more fracture resistant in comparison to the non-segmented counterpart (monolithic) (Figure 1-5a).

Propagating cracks in segmented materials face two options either to kink into the tablet (i.e. penetrate the tablets) or propagate along the interface between the blocks. In terms of fracture mechanics, the crack is more likely to deflect and follow through the interfaces if the energy release rate of deflection  $G_d$  to energy release rate of penetration  $G_p$  ratio ( $G_i / G_p$ ) is higher than the toughness of the interface  $\Gamma_i$  relative to the toughness of the tablet material  $\Gamma_l$ :  $G_i / G_p > \Gamma_i / \Gamma_l$  [55]. Therefore, multiple deflections can be induced by ensuring a low  $\Gamma_i / \Gamma_l$ , which is favored for enhancing the toughness of the material.

The mechanical response of segmented materials is generally characterized by a gradual increase in the force until load maximum load is reached followed by a smooth softening to failure due to relative motion between blocks (energy is being dissipated) [17, 51, 56, 57] (Figure 1-5b). This response can be captured by numerical techniques such as finite element method (FEM) and discrete element method (DEM) or by robust analytical models, such as classical beam theory [58], plate theory [59], strain energy [60], and thrust-line deformation (TD) [61], all of which can be implemented to model the force-deflection curves of architected materials.

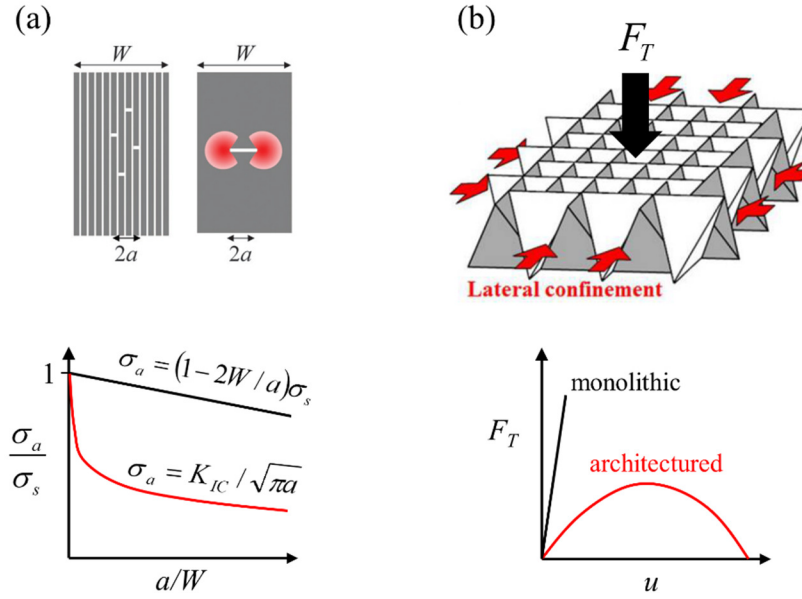


Figure 1-5: Segmentation improves (a) damage resistance (resistance to crack propagation) and (b) energy absorption and deformability. The top images in (a) are adapted from [42] with permission by Royal Society of chemistry, and (b) is adapted from [48] with permission by Taylor and Francis.

In terms of statistics, the survival probability  $P_s$  of brittle materials depend on Weibull exponent  $m$ , following the relationship below:

$$P_s = \exp\left(-\frac{V}{V_o}\left(\frac{\sigma}{\sigma_o}\right)^m\right) \quad (1.1)$$

where  $V_o$  and  $\sigma_o$  are normalized parameters that are material constants. Probability of failure which is typically used is simply:  $P_f = (1 - P_s)$ . The exponent  $m$  characterizes brittleness of materials. The lower the  $m$  the more brittle the material, therefore the slower the increase in  $P_s$  as applied stress  $\sigma$  increases. The larger the size  $V$  the lower the survival probability  $P_s$ . Unlike monolithic materials, segmented bodies fail due to failure of much smaller unit blocks. Therefore, the failure of these small unit blocks requires larger stress  $\sigma$ . In addition, the failure of a segmented structure requires the failure of several of these blocks. As a result, the relative increase in strength of segmented system  $\sigma_a$  relative to monolithic  $\sigma_s$  is given by [62]:

$$\frac{\sigma_a}{\sigma_s} \approx n \left( \frac{D}{P_f} \right)^{1/m} \quad (1.2)$$

Where  $n$  is the number of segments,  $D$  is the probability of damage of individual blocks and  $P_f$  is the probability of failure of a monolithic sample. Here, the key result is that as  $n$  is increased, (1.2) it suggests that the material becomes more damage tolerant. This improvement in damage tolerance scales with  $1/m$ , so when  $m$  decreases (i.e. the material becomes more brittle),  $\sigma_a / \sigma_s$  increases. This suggests that the improvement in damage tolerance is more pronounced in brittle materials in comparison with less brittle ones or ductile ones. Accordingly, segmentation is more suited for brittle materials. It is therefore of no surprise to see brick-walls made from brittle blocks and the microstructure of nacre made from brittle aragonite plates.

## 1.5 Topologically interlocked materials (TIMs)

Bricks, clays, glass and ceramics are examples of brittle materials. In masonry however, these materials are typical building materials [63]. Building blocks are molded into different shapes and stacked together in various arrangements. Such strategy is prevalent in historical buildings, monuments and pavements (Figure 1-6a). Masonry structures proved robust in standing the test of time and particularly in resisting seismic activities. In modern times, masonry takes various arrangements and shapes to form self-standing structures, domes, lentils, shear walls and pavements [63]. Since the emergence of the notion that segmented systems are to be considered as materials, along with the consistent accounts revealing segmented structures in diverse natural systems at multiple scales. Strategies in masonry immediately caught attention and are being revisited, which has directly inspired a new class of architected materials known as topologically interlocked materials (TIMs) (Figure 1-6b). Like masonry, TIMs are segmented into blocks, therefore they inherit the above advantages of segmented systems. TIMs however are made from separate blocks that are not connected. Component made from TIMs maintain integrity through interlocking. The absence of any ligaments or binders to such systems, require side supports and abutments for TIMs to rest on and achieve stability. Also, since such systems are made from discrete blocks, they require an assembly method to put them into service. Assembly methods

range from manual pick-and-place, directional assembly, gravity driven assembly and self-assembly [51]. Self-assembly can be driven by magnetic field or vibration. Another powerfully option is 3D printing, where an entire assembled structure/component is printed with appropriate distances set between blocks to avoid their bonding. 3D printing allows also the fabrication of complex blocks shapes as well as achieve structural hierarchy [49, 64, 65]. Similarly, the advancement in precision cutting such as computer numerical control (CNC) cutting, or molding techniques allowed the fabrication of intricately shaped ceramics and glass, with high geometric fidelity [66].

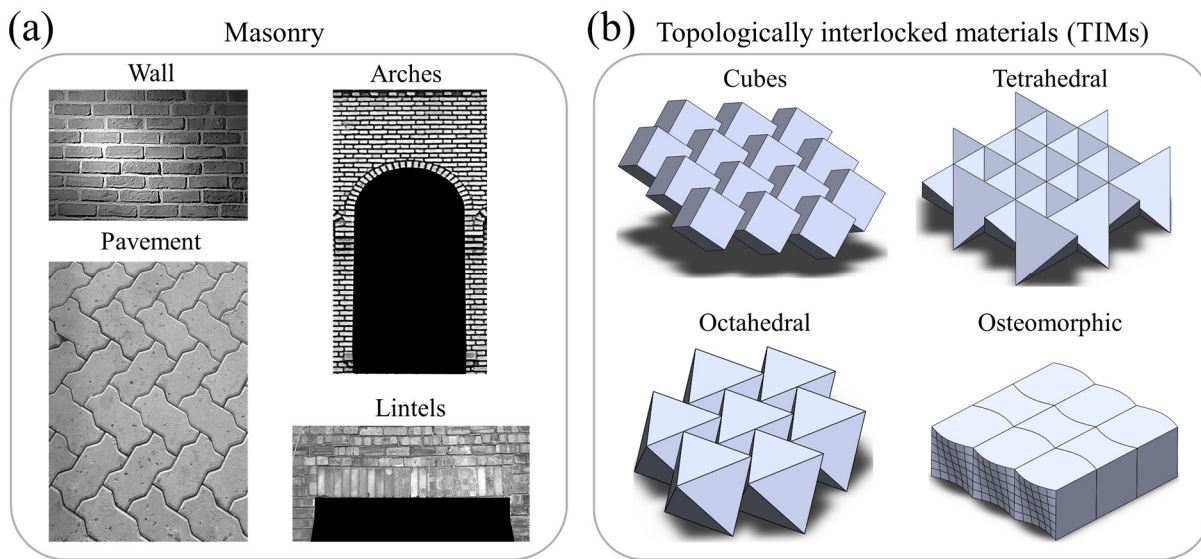


Figure 1-6: Segmentation in (a) masonry structures; lintel image is adapted from [68] with permission by Elsevier; (b) topologically interlocked materials.

## 1.6 Thesis objectives

Some designs in the literature combined several strategies together. Different materials were integrated, forming composites with various architectures. Although some of these investigations were effective, fundamental gaps still persisted. Take segmentation for example, despite being widespread in nature, a thorough understanding of its underlying mechanics and possible failure modes in different systems is still lacking. Such understanding is required before embarking into complex geometries, material combinations or hierarchal structuring. Here in this thesis, the effect

of segmentation is isolated by studying a simple row of idealized segmented beam. In addition, several studies focused on osteomorphic morphology. However, osteomorphic morphology is essentially a series of 2D polynomial function that includes low and high order terms. In other words, a series of enrichments are performed to blocks geometry where each of which deserves mechanistic investigation. Finally, interfaces are a fundamental aspect in architected materials. Nevertheless, the effect of fracture toughness of these interfaces on the behavior of materials is not well understood. The above are some aspects that this thesis addresses through accomplishing the following objectives:

- Explore the effect of segmentation on architected materials.
- Develop analytical models for the mechanics of architected beams.
- Develop computational models to assess the performance of more complex designs of architected beams.
- Explore the effect of block geometry on strength, toughness, deformation and overall behavior of architected beams.
- Find a metric for block geometry and relate it to strength and toughness of architected beams.
- Find optimum block morphology for architected beams.
- Develop design guidelines for architected beams and plates.
- Understand the effect of fracture toughness of interfaces in architected materials.
- Endow thick glass panels with toughness and damage tolerance using designed interfaces.
- Develop a nondestructive framework for assessing damage in transparent materials.

## 1.7 Thesis organization

This thesis is a manuscript based and consists of five chapters. Chapter 1 which is the current part of the thesis presents a brief overview of history of materials. It discusses the evolution of materials from 10,000 B.C.E up until today. It describes how advancements in microcopy and fabrication are at the forefront of a new age in material design. Materials are to be built from the bottom up,

from nano- to macro-scale levels, with architectures and material combinations that are precisely tuned for several functions.

Chapter 2 filled a gap in the literature. Segmentation is a fundamental element of architected materials. Underlying mechanics of segmentation is not well understood yet. This chapter establishes the foundation of segmented beams through experiments, analytical modeling and finite element modeling (FEM). An idealized row of cubes is used here to study segmented systems. The performance of this system is assessed using transverse loading, which is a typical load on beams and panels. Using FEM model, the behavior of a more complex system is predicted where the blocks of the beam are enriched with round contact faces. Such systems are akin to vertebrae of reptiles. The investigation generated comprehensive failure maps and design guidelines for segmented beams.

Chapter 3 presents a study of the effect of various enrichments on the mechanics of architected beams. A simple row of five cubes is first modeled and validated with experiments and verified with analytical models. The blocks are first enriched by rounding their corners and edges. Then the blocks were progressively enriched using 2D polynomial function, up to third order terms. Unlike the literature where complex shapes such as osteomorphic morphology are used without compelling design need, in other words it was mainly spurred by the prominence of osteomorphic design in nature. Here instead, complex geometries were formed by combining individual polynomial terms. Resulting in incremental enrichment of blocks into curved and wavy geometries. Such designs lead to more mechanical hardening than flatter ones. A simple metric based on the mean ratio of second order derivatives to divergence of the functions governing the contact faces between blocks shows a strong linear relationship with hardening. Optimum designs were found based on the different strength of blocks. Optimum designs of blocks were fabricated in ceramic glass using laser cutter. They were assembled into architected beams, tested experimentally and compared against monolithic samples.

Chapter 4 focuses on toughening glass by generating 3D networks of weak interfaces using laser engraving. The main difference from current studies in the literature is that the interfaces are not fully cut. They have a finite strength and blocks are still attached to each other; therefore they hold the structure together. Careful control over the parameters of laser engraving is therefore required. Laser induced microcracks and the engraved interfaces were first characterized nondestructively

using confocal microcopy. The toughness of interfaces is controlled by varying the microcrack spacing. The fracture toughness at different microcrack spacing was measured using fracture tests on bend samples. Fractographic analysis of fracture surfaces were followed to characterize the crack propagation upon breakage of interfaces. A grid network was engraved in borosilicate panels, thereby forming architected panels. These panels were tested under impact loading and they were monitored by highspeed imaging to capture all stages of deformation. Architected panels absorbed more energy than monolithic ones, but at the expense of strength. To mitigate this decrease in strength, front and back plain glass layers were used to confine the architected layer. This approach improved both strength and toughness of glass.

Finally, chapter 5 presents conclusions and research contributions of this thesis. Some guidelines on future directions were also proposed.

## 1.8 References

1. Hummel, R.E., *Understanding Materials Science: History, Properties, Applications, Second Edition*. 2004: Springer Science & Business Media. 484.
2. Kuzmin, Y.V., et al., *Obsidian use at the Ushki Lake complex, Kamchatka Peninsula (Northeastern Siberia): implications for terminal Pleistocene and early Holocene human migrations in Beringia*. *Journal of Archaeological Science*, 2008. **35**(8): p. 2179-2187.
3. Solecki, R.S., *A Copper Mineral Pendant from Northern Iraa*. *Antiquity*, 1969. **43**(172): p. 311-314.
4. Ashby, M., *Materials—a brief history*. *Philosophical Magazine Letters*, 2008. **88**(9-10): p. 749-755.
5. Macfarlane, A. and G. Martin, *A World of Glass*. *Science*, 2004. **305**(5689): p. 1407-1408.
6. Srinivasan, S., *Ultrahigh-carbon “wootz” from crucible carburization of molten iron: Hypereutectoid steel from “Tamil Nadu Process” at Mel-siruvalur*. *Materials and Manufacturing Processes*, 2017. **32**(7-8): p. 909-915.
7. Ashby, M.F., *Materials Selection in Mechanical Design*. 5 edition ed. 2017, Cambridge, MA: Butterworth-Heinemann. 660.
8. Needham, J. and T. Tsuen-Hsui, *Science and Civilisation in China: Volume 5, Chemistry and Chemical Technology, Part 1, Paper and Printing*. 1985: Cambridge University Press. 520.
9. Verhoeven, J.D., A.H. Pendray, and W.E. Dauksch, *The key role of impurities in ancient damascus steel blades*. *JOM*, 1998. **50**(9): p. 58-64.
10. Fleck, N.A., V.S. Deshpande, and M.F. Ashby, *Micro-architected materials: past, present and future*. *Proceedings of the Royal Society A: Mathematical, Physical and Engineering Sciences*, 2010. **466**(2121): p. 2495-2516.
11. Crespy, D., M. Bozonnet, and M. Meier, *100 Years of Bakelite, the Material of a 1000 Uses*. *Angewandte Chemie International Edition*, 2008. **47**(18): p. 3322-3328.

12. Wachtman, J.B., W.R. Cannon, and M.J. Matthewson, *Mechanical Properties of Ceramics*. 2009: John Wiley & Sons. 498.
13. Huang, H., et al., *U-involved sphere-dispersed metallic glass matrix composites*. *Materials & Design*, 2018. **157**: p. 371-376.
14. Krstic, V.V., P.S. Nicholson, and R.G. Hoagland, *Toughening of Glasses by Metallic Particles*. *Journal of the American Ceramic Society*, 1981. **64**(9): p. 499-504.
15. Munch, E., et al., *Tough, Bio-Inspired Hybrid Materials*. *Science*, 2008. **322**(5907): p. 1516-1520.
16. Wegst, U.G.K., et al., *Bioinspired structural materials*. *Nature Materials*, 2015. **14**(1): p. 23-36.
17. Barthelat, F., *Architected materials in engineering and biology: fabrication, structure, mechanics and performance*. *International Materials Reviews*, 2015. **60**(8): p. 413-430.
18. Ashby, M.F., *Hybrids to fill holes in material property space*. *Philosophical Magazine*, 2005. **85**(26-27): p. 3235-3257.
19. Ashby, M.F., et al., *Metal Foams: A Design Guide*. 2000: Elsevier. 267.
20. Courtney, T.H., *Mechanical Behavior of Materials, 2/E*. 2 edition ed. 2005: Waveland Press. 752.
21. Ritchie, R.O., *The conflicts between strength and toughness*. *Nature Materials*, 2011. **10**(11): p. 817-822.
22. Liu, Z., et al., *Functional gradients and heterogeneities in biological materials: Design principles, functions, and bioinspired applications*. *Progress in Materials Science*, 2017. **88**: p. 467-498.
23. Counselling. *Free Image on Pixabay - Shell, Beach, Oyster*. 2019/11/26/20:31:30; Available from: <https://pixabay.com/photos/shell-beach-oyster-mother-of-pearl-456564/>.
24. Barthelat, F., et al., *On the mechanics of mother-of-pearl: A key feature in the material hierarchical structure*. *Journal of the Mechanics and Physics of Solids*, 2007. **55**(2): p. 306-337.
25. Géraudie, J., et al., *Teratogenic and morphogenetic effects of retinoic acid on the regenerating pectoral fin in zebrafish*. *Journal of Experimental Zoology*, 1994. **269**(1): p. 12-22.
26. Bester, C. *Tooth Types & Patches*. Florida Museum 2017; Available from: <https://www.floridamuseum.ufl.edu/discover-fish/fish/anatomy/tooth-types-patches/>.
27. Molnar, J.L., et al., *Morphological and functional changes in the vertebral column with increasing aquatic adaptation in crocodylomorphs*. *Open Science*, 2015. **2**(11): p. 150439.
28. Barthelat, F., *Biomimetics for next generation materials*. *Philosophical Transactions of the Royal Society of London A: Mathematical, Physical and Engineering Sciences*, 2007. **365**(1861): p. 2907-2919.
29. Barthelat, F., Z. Yin, and M.J. Buehler, *Structure and mechanics of interfaces in biological materials*. *Nature Reviews Materials*, 2016. **1**(4): p. 16007.
30. Huang, W., et al., *Multiscale Toughening Mechanisms in Biological Materials and Bioinspired Designs*. *Advanced Materials*. **0**(0): p. 1901561.
31. Currey, J.D., *Bones: Structure and Mechanics*. 2002: Princeton University Press. 464.
32. Rho, J.-Y., L. Kuhn-Spearing, and P. Zioupos, *Mechanical properties and the hierarchical structure of bone*. *Medical Engineering & Physics*, 1998. **20**(2): p. 92-102.

33. Gibson, L.J., et al., *The mechanics of two-dimensional cellular materials*. Proceedings of the Royal Society of London. A. Mathematical and Physical Sciences, 1982. **382**(1782): p. 25-42.
34. Rabiei, R., S. Bekah, and F. Barthelat, *Failure mode transition in nacre and bone-like materials*. Acta Biomaterialia, 2010. **6**(10): p. 4081-4089.
35. Gibson, L.J., *The mechanical behaviour of cancellous bone*. Journal of Biomechanics, 1985. **18**(5): p. 317-328.
36. Tang, Z., et al., *Nanostructured artificial nacre*. Nature Materials, 2003. **2**(6): p. 413-418.
37. Wang, R.Z., et al., *Deformation mechanisms in nacre*. Journal of Materials Research, 2001. **16**(9): p. 2485-2493.
38. Abid, N., M. Mirkhalaf, and F. Barthelat, *Discrete-element modeling of nacre-like materials: Effects of random microstructures on strain localization and mechanical performance*. Journal of the Mechanics and Physics of Solids, 2018. **112**: p. 385-402.
39. Abid, N., J.W. Pro, and F. Barthelat, *Fracture mechanics of nacre-like materials using discrete-element models: Effects of microstructure, interfaces and randomness*. Journal of the Mechanics and Physics of Solids, 2019. **124**: p. 350-365.
40. Alben, S., P.G. Madden, and G.V. Lauder, *The mechanics of active fin-shape control in ray-finned fishes*. Journal of the Royal Society Interface, 2007. **4**(13): p. 243-256.
41. Porter, M.E., R.H. Ewoldt, and J.H. Long, *Automatic control: the vertebral column of dogfish sharks behaves as a continuously variable transmission with smoothly shifting functions*. The Journal of Experimental Biology, 2016. **219**(Pt 18): p. 2908-2919.
42. Fratzl, P., et al., *The mechanics of tessellations - bioinspired strategies for fracture resistance*. Chemical Society Reviews, 2016. **45**(2): p. 252-267.
43. Summers, A.P., *Stiffening the stingray skeleton — an investigation of durophagy in Myliobatid stingrays (Chondrichthyes, Batoidea, Myliobatidae)*. Journal of Morphology, 2000. **243**(2): p. 113-126.
44. Oxland, T.R., *Fundamental biomechanics of the spine—What we have learned in the past 25 years and future directions*. Journal of Biomechanics, 2016. **49**(6): p. 817-832.
45. Troxell, E.L., *Mechanics of Crocodile Vertebrae*. GSA Bulletin, 1925. **36**(4): p. 605-614.
46. Dorodnitsyn, V. and B. Van Damme, *Two-dimensional fluid-filled closed-cell cellular solid as an acoustic metamaterial with negative index*. Physical Review B, 2016. **93**(13): p. 134302.
47. Dyskin, A.V., et al., *Toughening by Fragmentation—How Topology Helps*. Advanced Engineering Materials, 2001. **3**(11): p. 885-888.
48. Dyskin, A.V., et al., *Topological interlocking of platonic solids: A way to new materials and structures*. Philosophical Magazine Letters, 2003. **83**(3): p. 197-203.
49. Mirkhalaf, M. and F. Barthelat, *Design, 3D printing and testing of architected materials with bistable interlocks*. Extreme Mechanics Letters, 2017. **11**: p. 1-7.
50. Mirkhalaf, M., et al., *Toughness by segmentation: Fabrication, testing and micromechanics of architected ceramic panels for impact applications*. International Journal of Solids and Structures, 2018.
51. Siegmund, T., et al., *Manufacture and Mechanics of Topologically Interlocked Material Assemblies*. Applied Mechanics Reviews, 2016. **68**(4): p. 040803-040803.
52. Djumas, L., et al., *Deformation mechanics of non-planar topologically interlocked assemblies with structural hierarchy and varying geometry*. Scientific Reports, 2017. **7**(1): p. 11844.

53. Estrin, Y., et al., *Architected Materials in Nature and Engineering: Archimats*. Springer Series in Materials Science. 2019: Springer International Publishing.
54. Kolednik, O., et al., *Improvements of strength and fracture resistance by spatial material property variations*. Acta Materialia, 2014. **68**: p. 279-294.
55. Hutchinson, J.W. and Z. Suo, *Mixed Mode Cracking in Layered Materials*. Advances in Applied Mechanics, 1991. **29**: p. 63-191.
56. Barthelat, F., M. Mirkhalaf, and A.K. Dastjerdi, *Method for increasing toughness and resistance to impact of material, involves engineering predetermined property of material by introduction of weak interfaces into materials*. 2015.
57. Mirkhalaf, M., J. Tanguay, and F. Barthelat, *Carving 3D architectures within glass: Exploring new strategies to transform the mechanics and performance of materials*. Extreme Mechanics Letters, 2016. **7**: p. 104-113.
58. Dyskin, A.V., et al., *A new concept in design of materials and structures: assemblies of interlocked tetrahedron-shaped elements*. Scripta Materialia, 2001. **44**(12): p. 2689-2694.
59. Khor, H.C., et al., *Mechanisms Of Fracturing In Structures Built From Topologically Interlocked Blocks*. ResearchGate, 2004.
60. Brocato, M. and L. Mondardini, *Parametric analysis of structures from flat vaults to reciprocal grids*. International Journal of Solids and Structures, 2015. **54**: p. 50-65.
61. Khandelwal, S., et al., *Transverse loading of cellular topologically interlocked materials*. International Journal of Solids and Structures, 2012. **49**(18): p. 2394-2403.
62. Ashby, M.F. and Y.J.M. Bréchet, *Designing hybrid materials*. Acta Materialia, 2003. **51**(19): p. 5801-5821.
63. Klingner, R.E., *Masonry Structural Design*. 2010, New York, USA, United States: McGraw-Hill Professional Publishing.
64. Martini, R., Y. Balit, and F. Barthelat, *A comparative study of bio-inspired protective scales using 3D printing and mechanical testing*. Acta Biomaterialia, 2017. **55**: p. 360-372.
65. Campbell, T., et al. *Could 3D Printing Change the World?* Atlantic Council 2011; Available from: <http://www.atlanticcouncil.org/publications/reports/could-3d-printing-change-the-world>.
66. Valashani, S.M.M. and F. Barthelat, *A laser-engraved glass duplicating the structure, mechanics and performance of natural nacre*. Bioinspiration & Biomimetics, 2015. **10**(2): p. 026005.
67. Sarhosis, V., S.W. Garrity, and Y. Sheng, *Influence of brick–mortar interface on the mechanical behaviour of low bond strength masonry brickwork lintels*. Engineering Structures, 2015. **88**: p. 1-11.

---

## Chapter 2

### Strength and stability in architected spine-like segmented structures

---

# Chapter 2: Strength and stability in architected spine-like segmented structures

Ahmed S. Dalaq and Francois Barthelat\*

Department of Mechanical Engineering, McGill University, 817 Sherbrooke Street West,  
Montreal, QC H3A 2K6, Canada

\*Corresponding author. E-mail address: francois.barthelat@mcgill.ca

## 2.1 Abstract

Architected and segmented material designs have recently emerged as a powerful approach to increasing the strength and toughness of brittle materials. Architected materials are made of regular building blocks that can collectively slide, rotate, separate or interlock, providing a wealth of tunable mechanisms and properties. In this work we have used experiments and modeling to explore the mechanical response of idealized segmented systems made of a linear array of cubes subjected to axial pre-compression and to a transverse force. From simple tabletop experiments with playing dice with instrumented tests on 3D printed cubes and simple models, we highlight the effects of axial pre-compression, number of blocks, friction coefficient and surface morphology on strength, energy absorption (toughness) and stability (catastrophic vs. graceful failure). We identified two failure modes in this segmented system: a sliding mode where one or more blocks slide on one another, and a “hinging” mode where some interfaces open and rotate about hinge points. The failure mode transition between hinging and sliding was established, to assist the design of modern architected structures and materials. Finally, we demonstrate that enriching the morphology of the cubes with curved interfaces (akin to the vertebrae in the spine of reptiles) delays hinging and improves stability.

**Keywords:** Architected materials, segmented materials, structural stability, topologically interlocking materials (TIMs)

## 2.2 Introduction

Specific microstructures, heterogeneities or hybrid compositions are now widely used in modern materials to generate high performance [1]. These concepts are now pushed to the extreme with architected materials, which contain highly controlled structures and morphological features at length scales intermediate between the microscale and the size of the component. Architected materials include composites [2, 3] and the now well-studied lattice materials [4-7], which contain only a small fraction of solid. In contrast, the much less studied dense architected materials are fully solid and are made of building blocks of well-defined size and shape, arranged in two or three dimensions [8-11]. The building blocks are stiff so their deformation remains small and within elastic limits, but the interfaces between the blocks can channel cracks and generate nonlinear deformations by frictional sliding. Building blocks can therefore collectively slide, rotate, separate or interlock, providing a wealth of tunable mechanisms and properties [9]. These information-rich materials can be designed with specific architectures, geometries and interfaces to generate unusual and attractive combinations of properties and functionalities. For example architecture can be used to combine high strength and toughness (two properties which are mutually exclusive in traditional engineering materials [12, 13], Figure 2-1a, b), or enhance impact resistance [10] and ballistic performance [14] in glasses or ceramics. Mechanical response is largely governed by the interactions between the blocks, which can be captured using load line analysis [15], finite elements [16], or discrete element methods [17, 18]. Some of these concepts and mechanisms were inspired from masonry, where the fabrication of large structures was made possible by block by block assembly. Stiff building blocks with weaker interfaces also lead to crack deflection and to the containment of damage in large structures [9, 19-22]. Interestingly, nature has been making use of architected materials for millions of years. In bone, teeth or mollusk shells, the interplay between the shape, size, properties and arrangement of the building blocks generates, together with non-linear behavior (resulting from viscoplastic, friction and contact based deformations) at the interfaces, powerful combinations of stiffness, strength and toughness [9, 22, 23]. At larger length scales the segmentation of stiff elements which can move with respect to one another generates unusual combination of properties in hard surfaces with prismatic architectures to resist wear in teeth [24] or segmented armor in scales and osteoderms for flexible protection [25-29]. The spines of vertebrae is in essence a linear arrangement of stiff elements with controlled shape [30, 31], size

and interfaces that allows controlled flexural deformations. For example the vertebral column of dogfish sharks can behave like a spring or a brake depending on tailbeat frequency (or bending frequency) [32]. Fins and shark vertebrae are linear arrays of bony segmented mineralized blocks arranged linearly and connected by a collagenous membrane (Figure 2-1c) [32-34]. The morphology of the interfaces between vertebrae plays an important role in the overall mechanics of the spine. Some reptiles have concave and/or convex round interface articulation between their vertebrae [35-37]. These ball-and-socket like interfaces are prominent in animals that require a high range of motion with a combination of strength, toughness, and flexibility such as crocodiles, dinosaurs and lizards (Figure 2-1d) [37-39]. The depth of concave-convex joints varies along the spine, and is generally deeper in the neck because it is the most flexible section of the spine. To date, only a few biomimetic materials have successfully incorporated these concepts [19, 40, 41]. Despite recent efforts in unifying designs [42-44] and optimization [45, 46], there are still no comprehensive guidelines to select optimum architectures for given applications and requirements. This chapter presents a systematic mechanical analysis of linear segmented systems. We examine the strength and stability of a row of cubic idealized stiff elements under axial confinement and subjected to transverse loading. We established deformation and failure maps as function of friction coefficient and number of cubes, and we assess the effect of simple geometric enrichment on the mechanics and stability of this type of systems.

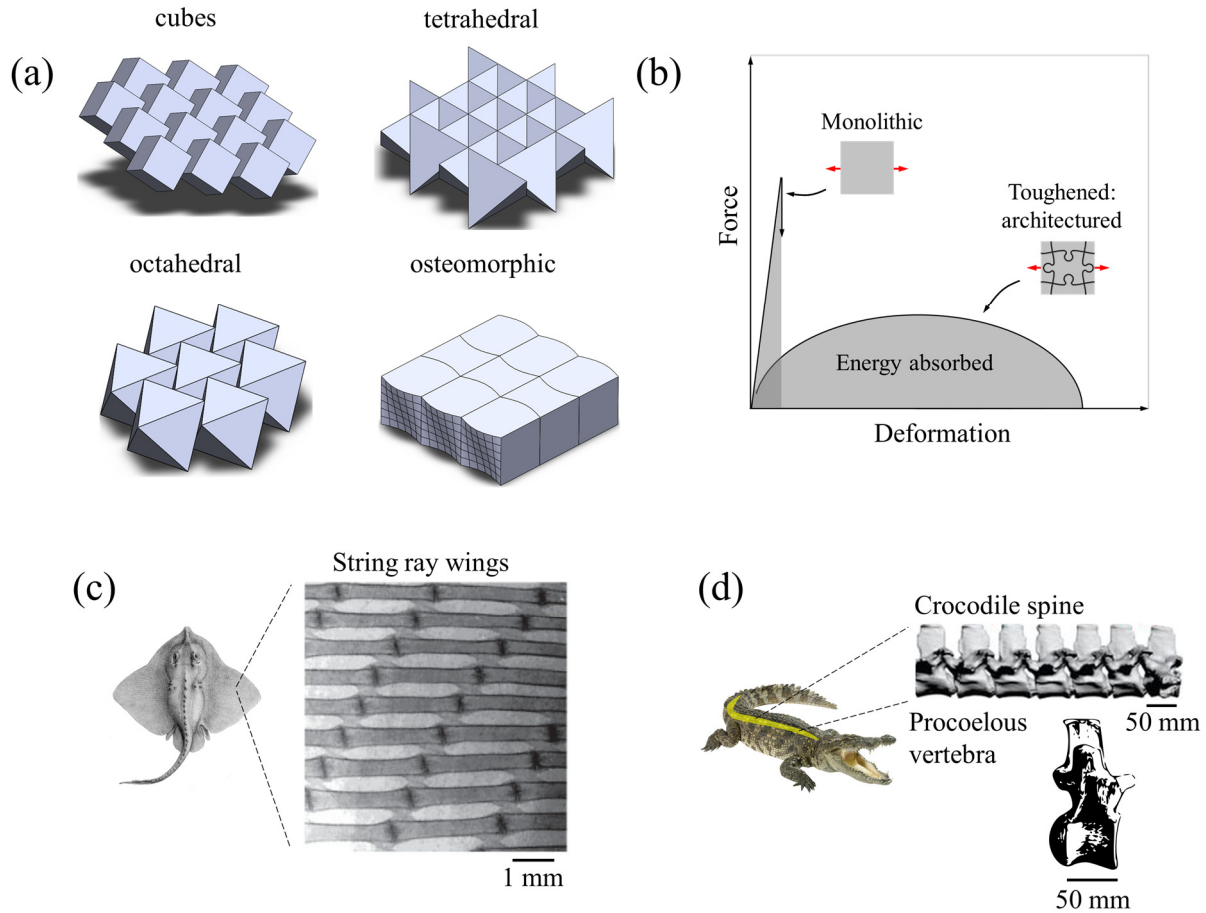


Figure 2-1: Examples of synthetic and natural architected materials: (a) Topologically interlocked materials (TIMs); (b) typical force-displacement response of architected materials versus monolithic materials. Linearly segmented architected materials in nature: (c) wings of a stingray fish: *Pteromylaeus asperimus* (adapted from [33]) and (d) concavo-convex vertebrae in the crocodile spine (adapted from [38]).

### 2.3 “Tabletop” experiments with dice

Some of the basic deformation mechanisms and mechanical stability of linear assemblies of blocks can be captured with arrays of dice. Two playing dice can be easily lifted from a table by pressing them together (Figure 2-2). It is also relatively easy to pick up a row of three, four and up to about six dice in the same manner, provided that the axial force exerted by the fingers is high enough to prevent the dice from slipping on one another. In these examples fingers confine the blocks together and act as an “external ligament”, akin to rigid frames in TIMs [8, 11, 47] or ligaments

in spine [30]. Picking up longer rows of dice up to nine dice is possible, but requires special care to align the dice and to distribute the axial pressure evenly. Using two hands to apply end pressures, rows of up to 12-13 dices can be lifted from a flat surface, but the row is very unstable even with perfect alignment of the dice. The stability of a row of dice, once it has been picked up, may be assessed by applying a transverse force half-way along its length (Figure 2-2). The amount of force required to collapse the row of dice may then be used as a measure of stability. By this measure, rows with  $N=2$  are very stable. In rows of  $N=3, 4$  or  $5$  dice, the center dice (or couple of dice if  $N$  is even) slide on one another to about  $1/3$  of their width, after which the system fails catastrophically. When a transverse force is applied on rows with  $N > 6$ , no sliding occurs and instead, dices near the center of the row separate and form a hinge. The two sections of the row rotate until a critical displacement is reached, leading to catastrophic collapse. All experiments suggest that long rows of dice (large  $N$ ) are much less stable than shorter rows. For example, for  $N=10$  the critical transverse force is very small, even when a large axial force is applied. These seemingly simple systems and experiments indicate that the stability, transverse strength of a row of cubes are governed by load transfer and interface mechanisms which are not trivial.

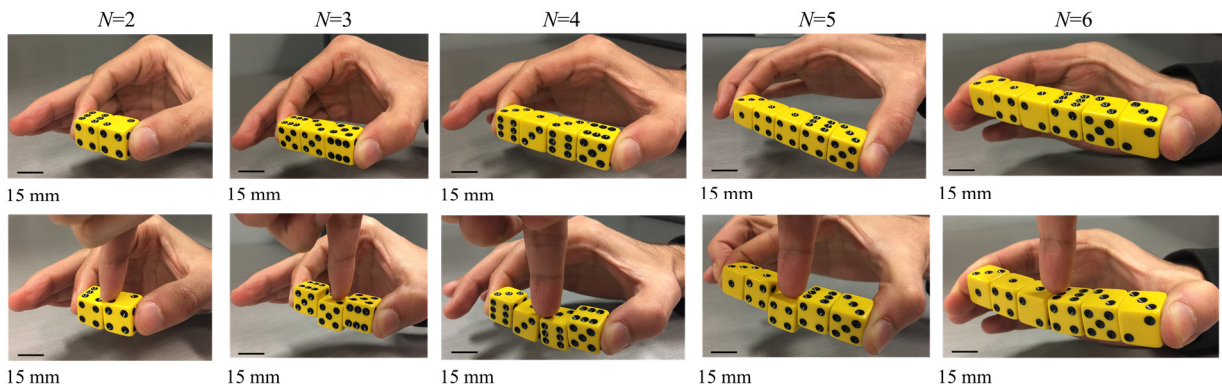


Figure 2-2: Simple experiments with rows of dice ( $N = 2$  to  $6$ ). An axial pre-compression is applied with thumb and index fingers. The failure mode and the stability of the system can be assessed by applying a transverse force half-way along the dice row.

## 2.4 Instrumented experiments

We developed better controlled experiments with instrumentation that duplicated the “dice” experiments discussed above (Figure 2-3a). Individual cubes ( $L^3 = 5 \text{ mm} \times 5 \text{ mm} \times 5 \text{ mm}$ ) were

3D printed using the Digital Light Processing (DLP) technology (Micro HiRes Machine, EnvisionTech) with an ABS UV-curable polymer (3DM-X Green). We used 3D printing to fabricate the cubes because with this method the geometry of the blocks can easily be enriched (as discussed in the last section of this chapter). The DLP printing method also enables high spatial resolution ( $\sim 80 \mu\text{m}$ ), a critical requirement for reproducibility, smooth surfaces and high morphological control [48]. In addition, DLP produces materials that are pore-free, homogenous and isotropic [49, 50] ensuring uniform and consistent elastic and frictional properties. The elastic modulus of the fully cured material is  $E=1.48 \pm 0.05 \text{ GPa}$  (measured using a standard tensile test).

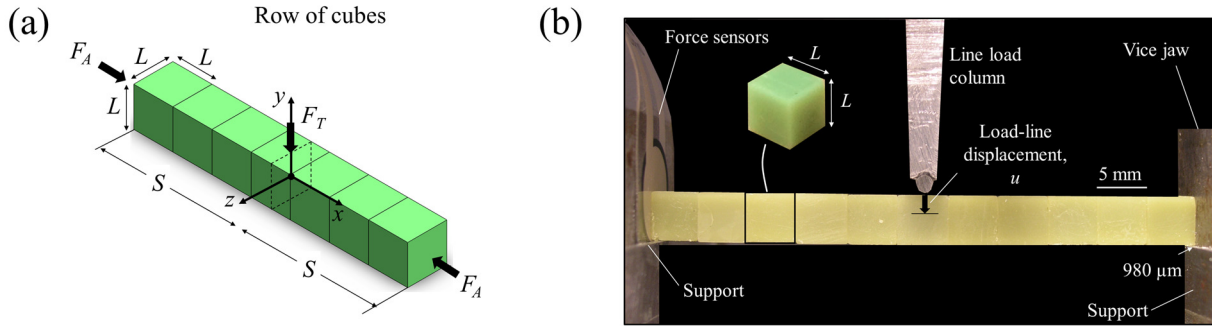


Figure 2-3: A segmented beam model and the experimental setup: (a) a row of cubes with sides of  $L \times L \times L$ , compressed from both ends with a force  $F_A$  and loaded halfway along the span  $S$  with a transverse force  $F_T$ ; (b) 3D printed cubes made from ABS polymer ( $L=5 \text{ mm}$ ) arranged linearly and pre-compressed axially. A loading machine is then used to impose a transverse displacement half-way along the system and to record the corresponding force.

We measured the friction coefficient between the ABS cubes using a standardized method (ASTM (D1894) [51]). The sliding force displayed the typical characteristics of friction, with an initial peak to initiate sliding from the static case (providing a “static” friction coefficient  $f_s$ ), and a sliding force fluctuating around an average value which provides a “dynamic” friction coefficient  $f_d$ ). For dry interfaces we measured coefficients of friction  $f_s=0.18\pm 0.02$  and  $f_d=0.12\pm 0.02$ . There was some fluctuations in force in the sliding regime corresponded to slick-slip, a common phenomenon for dry polymeric surfaces [52, 53]. We explored the effects of lower friction at the interfaces between the cubes by lubrication with white sulfonated grease. These interfaces showed no stick-slip, with a lower coefficient of friction equal to  $f_s=f_d=0.11\pm 0.01$ . On the other hand, we also explored the effects of increasing friction coefficient, by treating the surfaces with an anti-slip spray (Rust-

Oleum speckle spray) which produced coefficients of friction  $f_s=f_d=0.23\pm 0.03$ . For the stability experiments, 3D printed cubes were arranged and aligned into a segmented beam of  $N$  cubes. The beam was mounted on a vise used to apply an axial compressive force  $F_A$  at the ends of the row (Figure 2-3b).  $F_A$  was measured with a low-profile force sensor (FlexiForce®, Tekscan). We used different values for  $F_A$  ( $F_A = 10$  to  $200$  N), making sure that these axial forces were well below the force to plastically deform individual cubes ( $F_Y \approx 1600$  N). The compressed segmented beam was then placed in a dual column loading stage (Admet, model eXpert 5000, MA US), and a round nozzle ( $R=1.5$  mm) fixed to the crosshead was used to impose a displacement  $u$  in the direction transverse to the beam, at a rate of  $10 \mu\text{m}/\text{sec}$ . The transverse force  $F_T$  was measured using a 150 lbf load cell. Figure 2-4 shows a set of representative force-displacement curve  $F_T - u$  obtained from beams made of  $N=3$  to  $N=10$  cubes. In all cases the transverse force  $F_T$  initially increased linearly with displacement. In that linear regime, the segmented beam behaved like a homogenous, continuous elastic beam, and as a result the initial stiffness was lower for higher  $N$  (i.e. longer beams). When the number of cube was small ( $N < 7$ ), the linear region ended with a series of sudden drops at a critical sliding force  $F_T^{(s)}$  and at a displacement of about  $u^{(s)} \approx 0.3$  mm (the superscript  $^{(s)}$  denotes the onset of sliding). The stiff vise maintained constant axial displacement during experiments. The contact area between the cubes decreased linearly with sliding distance, resulting in a linear decrease of  $F_A$  and therefore in the observed linear decrease of  $F_T$  with sliding distance.  $F_T$  vanished at  $u \approx 4$  mm, at which point the beam collapsed. Throughout the sliding of cubes, large fluctuations of forces were associated with stick slip, a typical phenomenon for materials where the dynamic friction coefficient  $f_d$  is lower than the static friction coefficient  $f_s$  [52, 53]. The amplitude of the stick-slip force fluctuations was larger for higher  $N$ , because the larger volume of elastically deformed material stored more strain energy between each slip pulse.

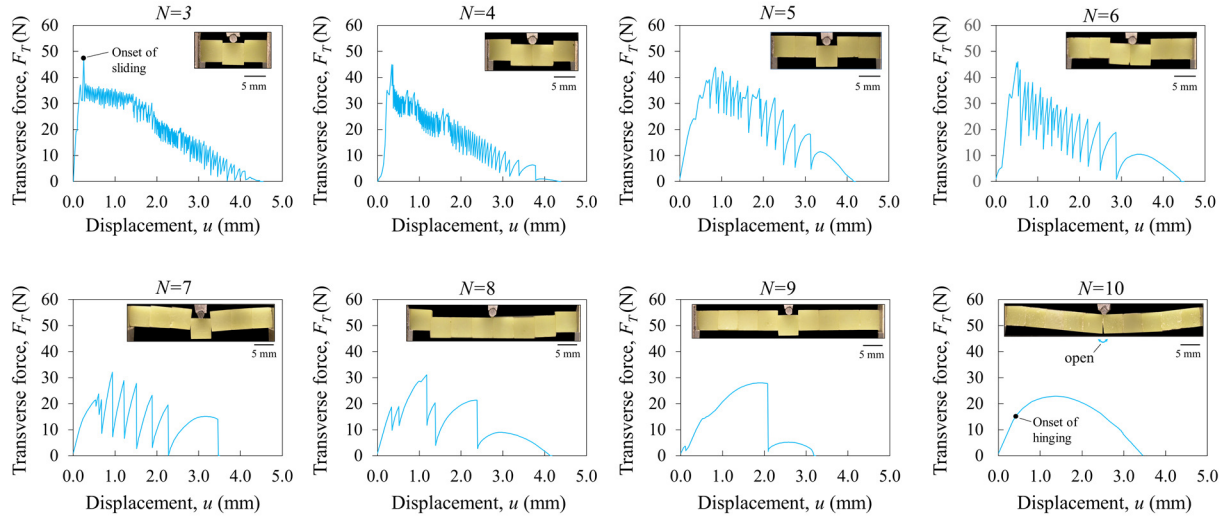


Figure 2-4: Experimental force-displacement  $F_T - u$  curve for the segmented cubes with different number of cubes ( $N=3$  through 10), for  $f_s=0.18\pm0.02$ ,  $f_d=0.12\pm0.02$  and with axial pre-compression  $F_A=150$  N. The failure mode transitions from sliding to hinging as  $N$  is increased.

The segmented beams with  $N = 7$  to 10 cubes produced a very different type of response. The  $F_T - u$  curve showed a nonlinear region before the cubes started to slide (if any sliding took place at all), which corresponded to the progressive opening and loss of contact of the interfaces, together with the relative rotations of individual cubes. In the case  $N=7$  and  $N=8$  sliding was still observed, but with much less stick-slip. For  $N=9$ , only one long slip was recorded for each experiment and for  $N=10$  no sliding was observed. In that case the  $F_T - u$  curve had a parabolic shape, and the only failure mode being the opening of the central interface, the formation of a hinge underneath the loading pin and of two additional hinge points at the ends of the beam. In the softening region of the curve, the two segments of beam rotated about these hinge points. With the case  $N=10$  we confirmed that the point at which the  $F_T - u$  curve deviated from a linear response matched the onset of hinging (Figure 2-4,  $N=10$ ), occurring at the critical hinging force  $F_T^{(h)}$  where the superscript  $^{(h)}$  denotes the onset of hinging.

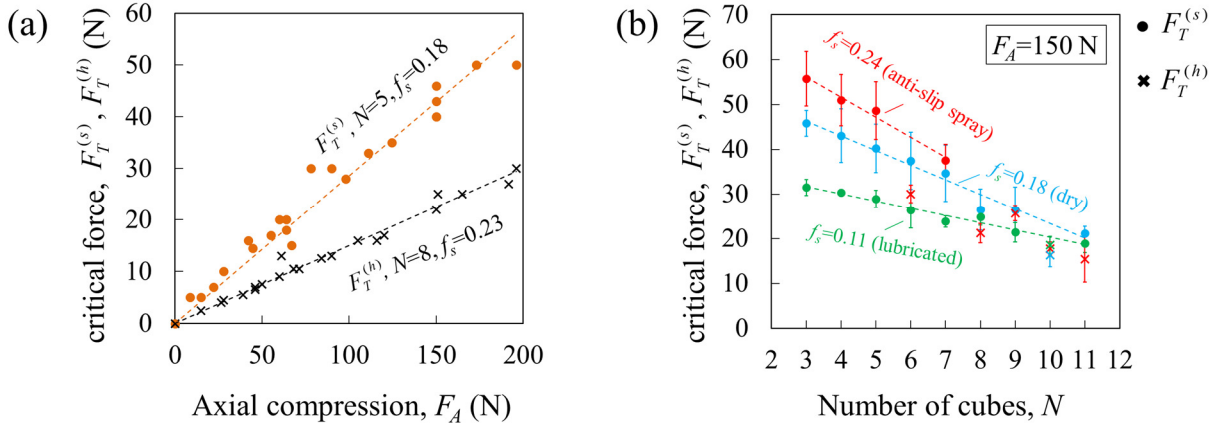


Figure 2-5: Critical sliding force  $F_T^{(s)}$  and hinging force  $F_T^{(h)}$  as function of (a) axial pre-compression  $F_A$  and (b) number of cubes  $N$ .

We found that the critical sliding force and the hinging force are both proportional to the axial pre-compression  $F_A$ . Figure 2-5a shows an example of these results for a sliding case ( $N=5$  with  $f_s=0.18$  on Figure 2-5a) and for a hinging case ( $N=8$  with  $f_s=0.23$  on Figure 2-5a). The experiments also confirmed that the critical force at sliding  $F_T^{(s)}$  decreases linearly with increasing  $N$ , and also that the critical force decreases when  $f_s$  is decreased (Figure 2-5b). Cases were hinging dominated, plotted as crosses on figure 2-5b, occurred at the highest friction coefficient. The critical force for hinging also decreases with  $N$  and is independent of  $f_s$  (Figure 2-5b). From these experiments we captured the trends and the effect of  $f_s$ , of both critical forces at sliding and hinging. These experiments guided the assumptions to be made for predicting  $F_T^{(s)}$  and  $F_T^{(h)}$  in section 2.5 and 2.6. The prominent failure mode is found by comparing the predicted onsets of sliding  $F_T^{(s)}$  and hinging  $F_T^{(h)}$ . If  $F_T^{(s)} < F_T^{(h)}$ , sliding prevails and if  $F_T^{(s)} > F_T^{(h)}$ , hinging prevails.

## 2.5 Modelling the onset of sliding

An analysis based on Coulomb's frictional force (stable friction dynamics) predicts that sliding starts when the shear force between the blocks reaches  $f_s F_A$  [53]. This simple approach predicts that any of the cubes is a candidate for sliding, and that the critical transverse force for sliding does

not depend on the number of cubes. The experimental observations contradict both predictions. In the experiments, only certain cubes on the beam actually slide (near the loading nose and near the supports), and the critical transverse force decreases when  $N$  is increased (Figure 2-5b). Capturing the mechanics of sliding in the segmented beam therefore requires a more detailed analysis. We consider a segmented beam of length  $S=NL$  made of  $N$  cubes of size  $L \times L \times L$  (Figure 2-6). The material of the cubes is modeled as homogenous and isotropic, and it is assumed to follow linear elasticity with an elastic modulus  $E$  and Poisson's ratio  $\nu$ . An axial compressive force  $F_A$  is applied along the  $x$ -axis, and a transverse force  $F_T$  is exerted exactly half-way along the beam and along the  $y$ -axis. The effect of gravity is neglected because the magnitudes of the applied forces are significantly higher than the gravitational body forces. The ends of the beam are assumed to be clamped, giving rise to a pair of reaction forces  $R$  and reaction couples  $M_R$  acting at both ends (Figure 2-6). The system is symmetric in terms of geometry and loading about the center of the beam. The moments along the beam are written (Appendix section 2.11.1):

$$\frac{M(x)}{2SF_T} = \frac{1}{8} \left( 1 - 2 \frac{|x|}{S} \right) \quad \text{for} \quad -1 \leq \frac{x}{S} \leq 1 \quad (2.1)$$

The bending moment along the  $x$ -direction is minimum at the two ends:  $M_{\min}/2F_T S = -1/8$  at  $x/S = -1.0$  and  $x/S = 1.0$  and is maximum  $M_{\max}/2F_T S = 1/8$  at the center  $x/S = 0$  (Figure 2-6).

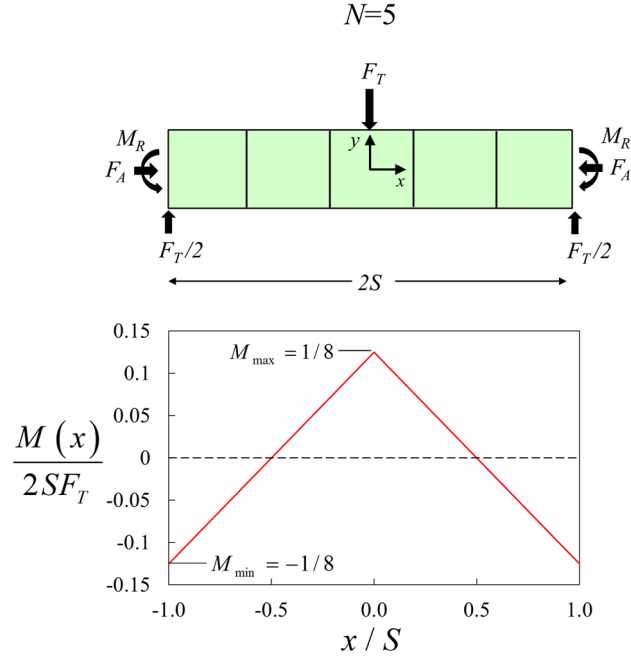


Figure 2-6: Load analysis for a row of 5 cubes showing the distribution of bending moment.

The bending moment  $M(x)$  and the (compressive) axial force  $F_A$  both give rise to an axial stress  $\sigma_{xx}$  which can be obtained by superposition, since the system is linear before the cubes start sliding (Appendix section 2.11.2):

$$\frac{L^2 \sigma_{xx}}{F_A} = 3 \frac{y}{L} \frac{F_T}{F_A} \frac{2S}{L} \left( -\frac{1}{2} + \frac{|x|}{S} \right) - 1 \quad \text{for} \quad -1 \leq \frac{x}{S} \leq 1 \quad (2.2)$$

$$\frac{L^2 \tau_{xy}}{F_A} = \pm 3 \frac{F_T}{F_A} \left[ \left( \frac{y}{L} \right)^2 - \frac{1}{4} \right] \quad \text{for} \quad \frac{x}{S} < 0 \quad \text{and} \quad \frac{x}{S} > 0 \quad (2.3)$$

where  $2S/L$  is the number of cubes  $N$ . A microslip occur when the shear stress at a point along an interface reaches or exceeds the local “frictional” strength:  $\tau_{xy} \geq f_s \sigma_{xx}$  [54-57]. Therefore, the criterion for microslip is based on the ratio:

$$\frac{1}{f_s} \left| \frac{\tau_{xy}}{\sigma_{xx}} \right| = \frac{1}{f_s} \frac{3 \left[ \left( \frac{y}{L} \right)^2 - \frac{1}{4} \right]}{3 \frac{y}{L} \frac{2S}{L} \left( -\frac{1}{2} + \frac{|x|}{S} \right) - \frac{F_A}{F_T}} \quad \text{provided} \quad \frac{x}{S} \neq 0 \quad (2.4)$$

Figure 2-7 shows a contour plot of  $\left| \tau_{xy} \geq f_s \sigma_{xx} \right|_{\max}$  at the onset of microslip,  $\left| \tau_{xy} \geq f_s \sigma_{xx} \right|_{\max} = 1$  when  $F_T/F_A=0.131$  for  $N=5$  and  $F_T/F_A=0.128$  for  $N=8$ . Figure 2-7 also shows the tendency of sliding in each interface by showing the ratio  $\left| \tau_{xy} \geq f_s \sigma_{xx} \right|_{\max}$  for odd case ( $N=5$ ) and even case ( $N=8$ ). This plot compares the tendency of sliding at each interface, where interfaces that satisfy  $\left| \tau_{xy} \geq f_s \sigma_{xx} \right|_{\max} = 1$  first are the “critical interfaces” that will slide and govern the failure mode of the segmented beam. Because of symmetry about the center ( $x=0$ ), these critical interfaces come in pairs and are located at  $x/L=-0.5, 0.5$  (odd) and  $x/L=-3, -1, 1, 3$  (even) which can be generalized as  $x/L=-0.5, 0.5$  (first row of Figure 2-7a) and  $x/L=1-N/2, -1, 1, 1+N/2$  (first row of Figure 2-7b) for odd and even cases, respectively. Critical interfaces for even cases have the same  $\left| \tau_{xy} \geq f_s \sigma_{xx} \right|_{\max}$  ratio because they are subjected to the same shear forces and moments (Figure 2-6). The last row in Figure 2-7 shows the snapshots taken during experiments for odd and even cases that sled. Sliding interfaces in the experimental snapshots match the predicted critical interfaces (i.e. the one with the highest  $\left| \tau_{xy} \geq f_s \sigma_{xx} \right|_{\max}$ ). These “critical interfaces” predictions are not limited to the two cases shown on Figure 2-7, we compared these predictions to up to 15 cubes cases, the predictions are also in agreement with the snapshots shown on Figure 2-4.

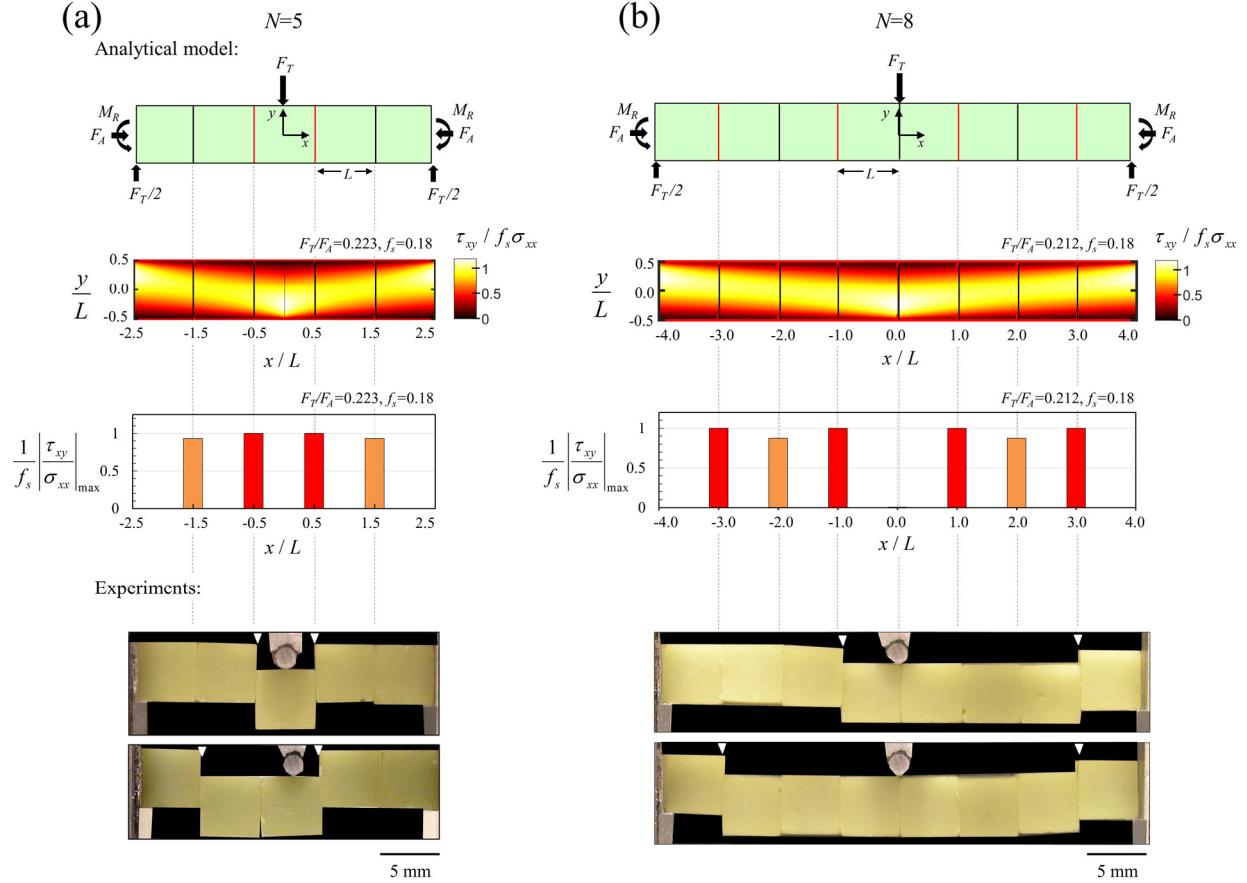


Figure 2-7: Maps of sliding ratio:  $\left| \tau_{xy} \geq f_s \sigma_{xx} \right|_{\max}$ , locations of the critical interfaces and experimental snapshots of the sliding cubes for (a) an odd case ( $N=5$ ) and (b) an even case ( $N=8$ ).

A general interface having  $f_d < f_s$  will experience multiple microsliPs (and stick-slip). If  $f_d$  is low enough to allow for a large microsliP distance, the sliding is catastrophic and the onset of microsliP cascades into the sliding of the entire interface [55-59]. For dry friction it is common to have  $f_d < f_s$  and therefore we expect the stick slip behavior seen earlier (Figure 2-4). Since sliding interfaces matched that of the catastrophic onset of sliding and  $f_d < f_s$  we considered the onset of the first microsliP as the onset of sliding,  $\left| \tau_{xy} \geq f_s \sigma_{xx} \right|_{\max} = 1$ .

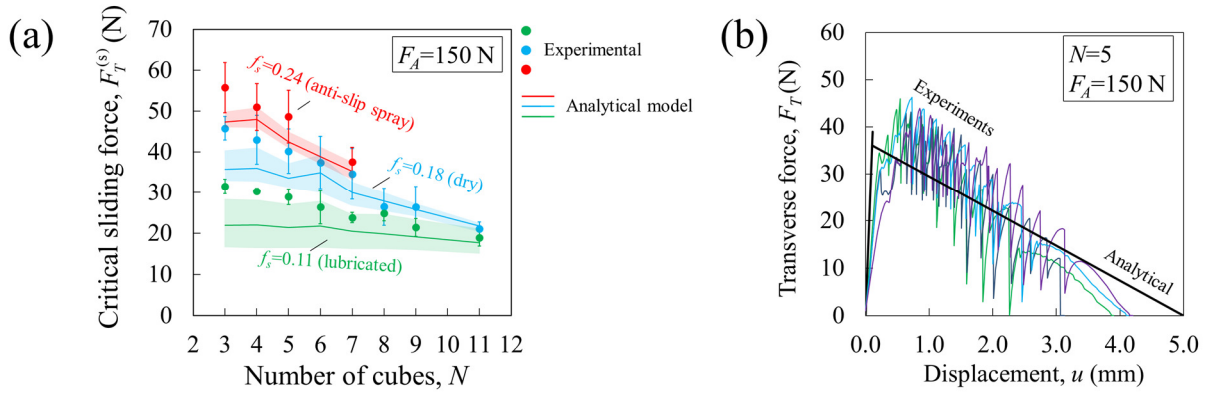


Figure 2-8: Comparisons of model predictions with experiments: (a) critical sliding force as function of the number of cubes and friction coefficient; (b) Force-displacement ( $F_T - u$ ) curves.

Now using the onset of sliding condition:  $\left| \tau_{xy} \geq f_s \sigma_{xx} \right|_{\max} = 1$  and solving for the transverse force  $F_T$  we get the critical sliding force  $F_T^{(s)}$  for both odd and even cases as follows,

$$\frac{F_T^{(s)}}{F_A} = \frac{16f_s}{3(4 + f_s^2(N-2)^2)} \quad \text{at } \frac{x}{L} = 0.5 \quad \text{for (odd case)} \quad (2.5)$$

$$\frac{F_T^{(s)}}{F_A} = \frac{16f_s}{3(4 + f_s^2(N-4)^2)} \quad \text{at } \frac{x}{L} = 1 \quad \text{for (even case)} \quad (2.6)$$

The analytical model predicts that the critical force  $F_T^{(s)}$  is proportional to the axial force  $F_A$ , which is consistent with the experiments (Figure 2-5a). Figure 2-8a compares the predicted critical sliding force  $F_T^{(s)}$  with the experimental results. The analytical model properly captures the decrease in  $F_T^{(s)}$  with increasing  $N$  (Figure 2-8a), and the predicted trends follow the experimental results closely. However the experimental results are about 18% higher than the prediction, because the experimental critical force for sliding may be the results of several microslips (while the analytical result only predict the onset of the first microslip) [56, 57, 59]. The analytical model can be extended to capture the full force-displacement  $F_T - u$  curve for the segmented beam. The  $F_T - u$  curve before the onset of sliding corresponds to the elastic deformation of the beam and it is given by (Appendix section 2.11.3):

$$F_T = \frac{16EL}{N^3}u \quad \text{for} \quad 0 \leq u \leq u^{(s)} \quad (2.7)$$

where  $u^{(s)}$  is the displacement at the onset of sliding. The force after the onset of sliding is governed by friction, and can be written (Appendix section 2.11.4):

$$\frac{F_T}{F_A} = 2f_d \left(1 - \frac{u}{L}\right) \quad \text{for} \quad u^{(s)} \leq u \leq L \quad (2.8)$$

Figure 2-8b compares this model with experimental  $F_T - u$  curves for  $N=5$ . The analytical model prediction is in good agreement with the experimental results. Discrepancies in initial modulus were attributed to non-perfect contact between the cube and to “interface compliance”, as well the end conditions in the experiments which may be more compliant than the perfectly clamped conditions assumed in the model. The area under  $F_T - u$  can be written as  $U / LF_A \approx f_d$  where  $U$  represents and estimates the energy dissipated during sliding which also represents the toughness of the segmented beam.

## 2.6 Modelling the onset of hinging

In the configurations with large  $N$ , the experiments showed that the interfaces between the cubes may lose contact and form hinge points. This type of failure mode, shown for  $N=10$  in Figure 2-4, occurs when the initial compressive stress from the axial force  $F_A$  is completely offset by tensile stresses from the bending moment. Since the interfaces cannot carry tensile stresses they will open and form hinges at certain points in the system where:

$$\frac{\sigma_{xx}}{F_A / L^2} = 0 \quad (2.9)$$

Recalling equation (2.2), this criterion can be written:

$$1 + \frac{L^2 \sigma_{xx}}{F_A} = 3 \frac{y}{L} \frac{F_T}{F_A} \frac{2S}{L} \left( -\frac{1}{2} + \frac{|x|}{S} \right) \quad (2.10)$$

This criterion is illustrated in Figure 2-9 as a contour plot at the onset of hinging when  $F_T/F_A=0.19$  for  $N=9$  and  $F_T/F_A=0.16$  for  $N=8$ . We monitor the criterion  $1 + \frac{\sigma_{xx}}{F_A/L^2}$  where value of 1 means that the interface opens at that point (to be consistent with the sliding criterion presented above). The contour plot shows region of higher tensile stress near the upper ends of the beam, and in the lower side of the center regions.

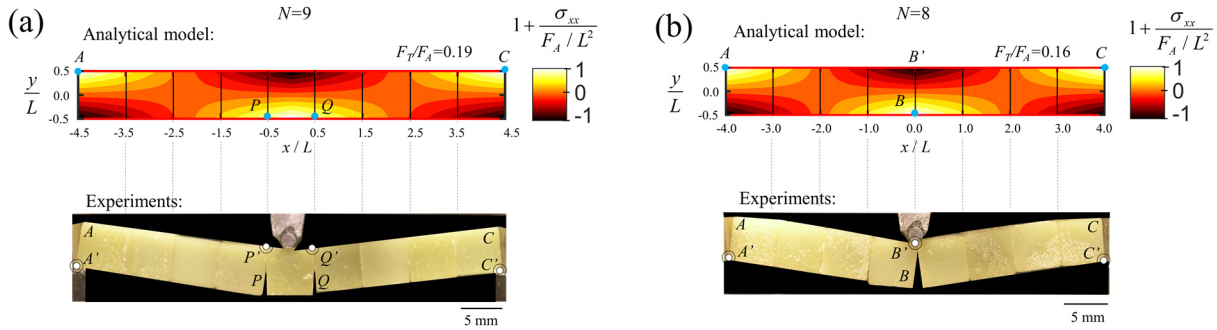


Figure 2-9: Distribution of the interface opening criterion:  $1 + \sigma_{xx}L^2/F_A$  across the whole beam for (a) odd and (b) even cases. Snapshots of the experiment during hinging is shown below the contour plots to compare it with analytical predictions for the hinging points.

The regions of highest stresses in this contour map can be matched with the positions of the interfaces to predict which interfaces will open first. For example for the case shown in figure 2-9a (odd number of cubes), the points that are going to open are  $A, P, Q$  and  $C$ , forming hinges at point  $A', P', Q'$  and  $C'$ . For the case shown in figure 2-9b (even number of cubes), the points that are going to open are  $A, B$  and  $C$ , forming hinges at point  $A', B'$  and  $C'$ . Snapshots from our experiments confirm these predictions. Solving for the force that satisfies the opening criterion at these points we find the critical force  $F_T^{(h)}$  that causes these points to open:

$$\frac{F_T^{(h)}}{F_A} = \frac{4}{3N} \quad \text{for} \quad (\text{even case: point } A, B \text{ and } C \text{ open}) \quad (2.11)$$

$$\frac{F_T^{(h)}}{F_A} = \frac{4}{3(N-2)} \quad \text{for} \quad (\text{odd case: point } A, P, Q \text{ and } C \text{ open}) \quad (2.12)$$

Figure 2-10a shows the experimental and analytical critical force at hinging  $F_T^{(h)}$  as function of the number of cubes.  $F_T^{(h)}$  decreases rapidly when  $N$  increases because the bending stresses increase with  $N$ .  $F_T^{(h)}$  is lower for even cases and therefore it is easier to hinge an even number of cubes case than an odd case. For even cases,  $F_T^{(h)}$  is lower because the critical points are subjected to higher moments than that of the odd case (Figure 2-6). The analytical model captures the decreasing trend quite well but consistently predicts higher  $F_T^{(h)}$  in comparison to the experimental measurements, reaching up to 16% error. This deviation can be attributed to non-perfect contact between the cubes where the interfaces can be more compliant than the bulk material. In addition, the end condition in the experiment may be more compliant than the model where perfectly clamped conditions are assumed. The apparent elastic modulus at the interfaces can be slightly lower due to local point contact at the hinging points (e.g.  $P'$ ,  $Q'$  or  $B'$  on Figure 2-9) in the case of hinging.

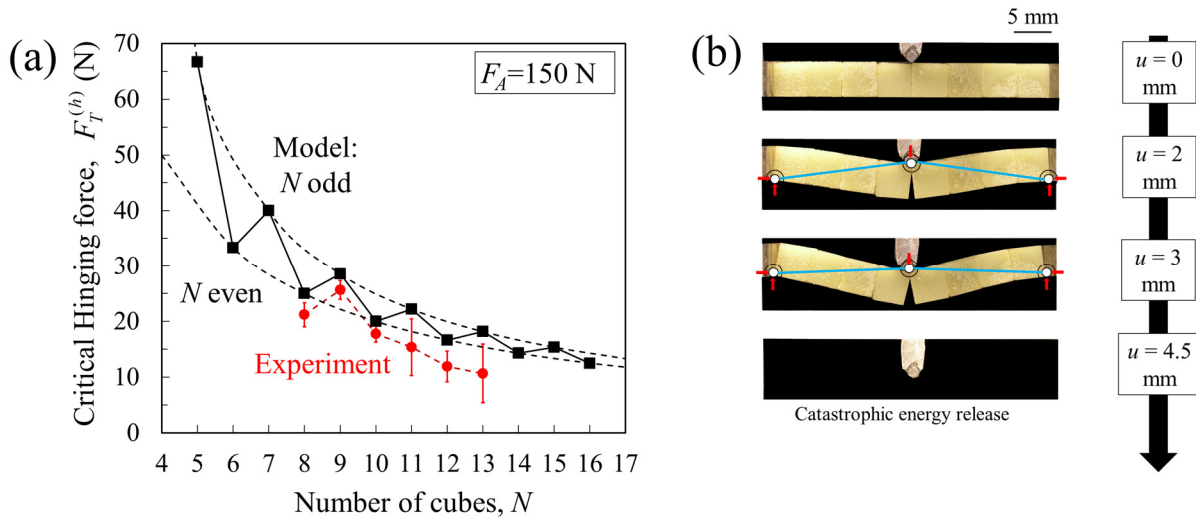


Figure 2-10: (a) Critical hinging force  $F_T^{(h)}$  as function of number of cubes, model prediction and experiments; (b) snapshots of the hinging process, with the load lines highlighted.

The mechanical response that follows the onset of hinging may be captured with a thrust line analysis [8, 15, 17]. The rotating section of the beams are confined axially and therefore develop compressive stresses from the geometric jamming. These compressive stresses are channeled in each section of beam through two hinge points which only transmit forces, and therefore each

section can be considered as a two dimensional two–force member (or thrust member) for the purpose of the analysis (Figure 2-10b). While this idealization is simple, the detailed force-deflection curve can be difficult to obtain because of geometric nonlinearities in the system (large rotations and non-linear contact stiffness at the hinges). Nevertheless, the thrust line analysis can provide two useful insights: first, unlike sliding failure mode that dissipates energy, the hinging deformation mode only involves elastic deformation and therefore it does not dissipate energy. Second, the hinging deformation mode is stable as long as the compressed thrust line can carry the applied force. When these lines become horizontal they cannot balance the applied force and the system becomes unstable (Figure 2-10b). This threshold marks the point of instability causing the system to release all the stored energy catastrophically, which ejects the cubes in all directions.

## 2.7 Failure modes competition: sliding versus hinging

The previous two sections provided the criteria for the onset of sliding and for the onset of hinging. We now examine and discuss which of the two failure modes may occurs first when the transverse force  $F_T$  is increased. The critical forces for sliding  $F_T^{(s)}$  and for hinging  $F_T^{(h)}$  only depend on the number of cubes  $N$  and on the friction coefficient  $f_s$  between the cubes, and therefore one can build a deformation map that depicts the failure mode as function of  $N$  and  $f_s$ . On this map, the transition between sliding and hinging corresponds to the condition  $F_T^{(s)} = F_T^{(h)}$ . Using equations (2.5), (2.6), (2.11) and (2.12), the equations for the transition lines are:

$$4f_s^2(N/4-1)^2 - f_s N + 1 = 0 \quad \text{for} \quad (\text{even case}) \quad (2.13a)$$

Which can be solved to give:

$$f_s = \frac{2N - 4\sqrt{2}\sqrt{N-2}}{(N-4)^2} \quad \text{for} \quad N \neq 4 \quad (2.13b)$$

$$f_s = 0.25 \quad \text{for} \quad N = 4 \quad (2.13c)$$

$$f_s^2(N/2-1)^2 - 2f_s(N/2-1) + 1 = 0 \quad \text{for} \quad (\text{odd case}) \quad (2.14)$$

For the cases where  $N$  is odd, the transition line equation is solved numerically because equation (2.14) does not have real roots. In these cases the critical sliding force and the critical hinging force cannot strictly be equal  $F_T^{(s)} \neq F_T^{(h)}$  because when  $F_T = F_T^{(h)}$  the “critical interface” (sliding ones) will lose contact (open) which mean that  $|\tau_{xy} / \sigma_{xx}|_{\max} \rightarrow \infty$ . For the cases where  $N$  is even, the interfaces that lose contact (Figure 2-9b) are different than the sliding “critical interfaces” (Figure 2-7b). Figure 2-11 shows deformation map resulting from these models. As expected sliding prevails for small number of cubes and small friction coefficient, while hinging prevails for large number of cubes and larger friction coefficient. The failure mode transition also depends on whether  $N$  is odd or even, but these predictions converge at large  $N$ . We emphasize that the transition between sliding and hinging is independent of the axial compressive force  $F_A$ . Interestingly, segmented beams made from cubes with low friction ( $f_s < 0.08$ ) will not hinge (Figure 2-11a). We found very good agreement between the theoretical prediction of the failure mode and the experimental observation over the range of  $f_s$  and  $N$  explored in this work (Figure 2-11b, 11c). In the next section we explore another way of manipulating the failure mode by tuning the shape of the cubes.

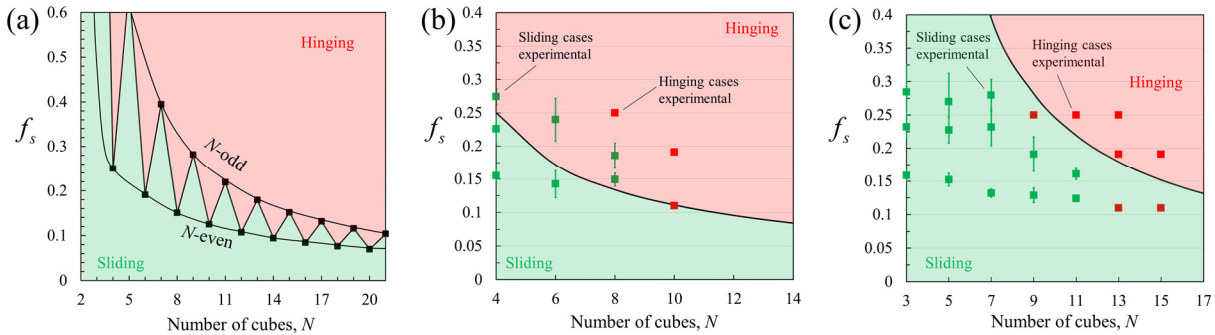


Figure 2-11: Deformations maps as function of the friction coefficient  $f_s$  and the number of cubes  $N$ ; (a) deformation map for odd and even cases; (b-c) comparison of the different combination of  $(N, f_s)$  with the actual experimental measurements at the onset of sliding for even cases and odd cases.

## 2.8 Geometrical enrichments

In terms of structural response, the sliding mode of failure is more beneficial than hinging: Sliding is stable, dissipates energy and only slightly decreases the structural integrity of the beam. In

contrast, hinging does not dissipate energy, it is unstable and it weakens the entire system since the forces are transmitted only through a few contact points ( $A'$ ,  $B'$ ,  $C'$ ,  $P'$  and  $Q'$  on Figure 2-9). Segmentation is primarily used to toughen brittle materials, so these contact points which localizes stresses may result in contact fracture. In this section we explore how the geometry of the cubes can be enriched to delay hinging and promote sliding. More specifically, we enrich the geometry of the contacting faces to generate progressive interlocking while at the same time channeling deformations in desired modes. A simple choice that fulfills these requirements is to design contact surfaces with a single curvature of radius  $R$ , with  $L/2 \leq R \leq +\infty$  (Figure 2-12a). The curved faces can be more conveniently described by a non-dimensional curvature  $CL=L/R$  with  $0 \leq CL \leq 2$ . In this study we considered  $CL=0$  (flat surface),  $CL=1/2$ ,  $CL=2/3$ ,  $CL=1$ ,  $CL=3/2$  and  $CL=2$  (maximum curvature, which corresponds to half a circle, Figure 2-12a). We tested these different geometries using the same experimental setup described above under a lower axial pre-compression of  $F_A=30$  N to prevent possible yielding at the sharp corners and edges of the blocks. Figure 2-12a shows snapshots of the deformation and failure modes for different surface curvatures.  $CL=0$  corresponds to the flat case considered above, where the center block slides. All cases with  $CL>0$  showed a different failure mode where half of the beam rotated collectively in one block. Figure 2-12b shows the effect of increasing the curvature on the  $F_T-u$  curves. Initially, the curves show a linear elastic rise, showing few drops while rising marking the onset of sliding. During sliding, the volume of material subjected to axial compressive stresses decrease, so that the axial compression  $F_A$  decreases. As a result the frictional forces decrease so  $F_T$  also decreases progressively. The benefits of curved surfaces become more evident for large number of blocks. Figure 2-13 shows the results for  $N=10$ , flat and curved interface with  $CL=1/2$ . The flat interface led to a hinging type of failure, with a characteristic parabolic shape (Figure 2-13b). The energy is stored within the beams, and it is released in a catastrophic failure mode. In contrast, the case  $N=10$  with curved interfaces ( $CL=1/2$ ) failed by sliding, with frictional energy dissipation and graceful, progressive failure.

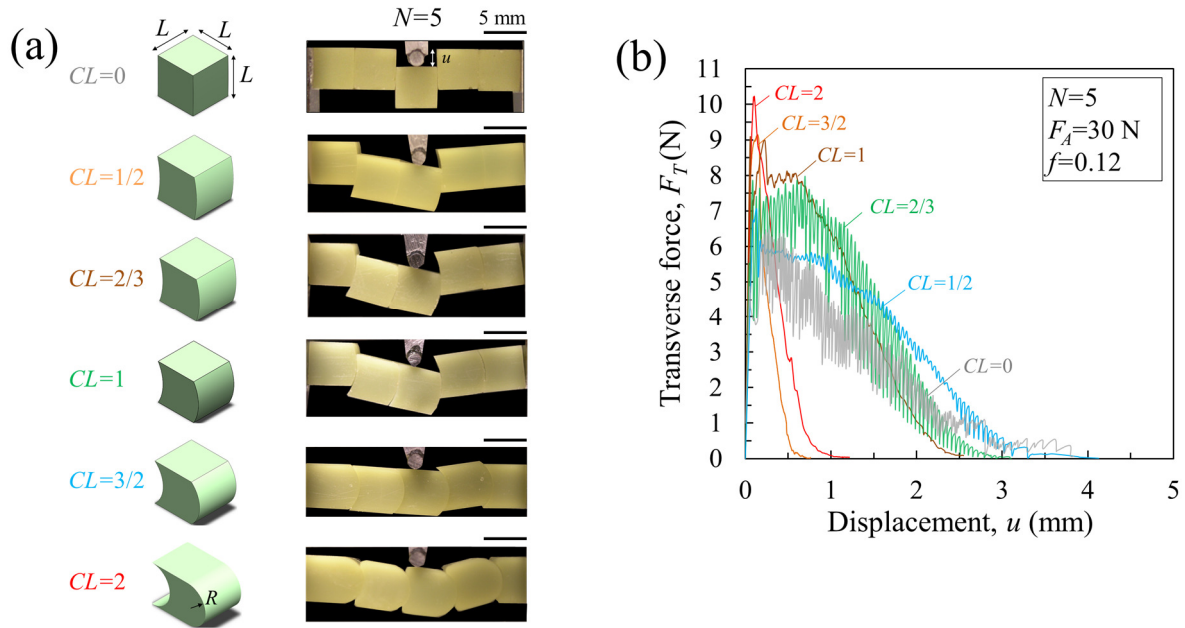


Figure 2-12: (a) Enrichment of the blocks with curved contact surfaces with various values of  $CL$  (schematics of individual blocks and with corresponding 3D printed samples tested under transverse loading); (b) Force-deflection ( $F_T - u$ ) curves for different curvatures:  $CL=L/R=0, 1/2, 2/3, 1, 3/2, 2$ .

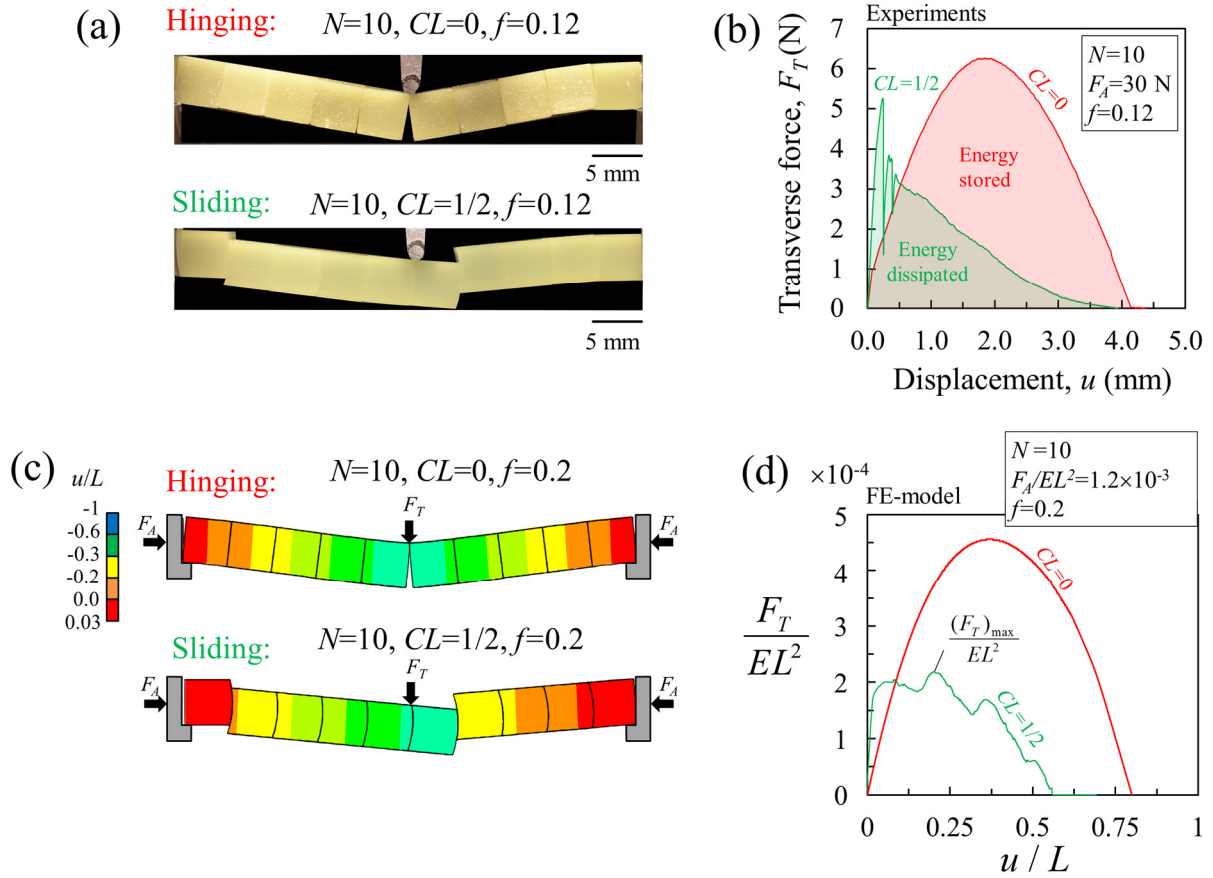


Figure 2-13: (a) Example of a contact surface enrichment that prevents hinging in the case  $N=10$ ; (b) Corresponding  $F_T-u$  curve for flat case (hinged) and curved case (sliding); (c) deformed architected beam obtained using finite element method (FE) for the cases in (a); (d)  $F_T-u$  curves obtained from FE.

The mechanical modeling of arrays of blocks with non-planar contact surfaces is challenging because deformation involves multiple contact points and interlocking of the blocks. Here we capture the transition from hinging to sliding modes using finite element (FE) models (Appendix section 2.11.5, Figure 2-16). The FE model was first validated with experiments (Figure 2-16b) and then used to simulate the sliding and hinging failure modes (Figure 2-13b).  $F_T-u$  curves from the FE model captured the sliding trend of  $CL=1/2$  and the characteristic parabolic shape of hinging failure mode well (Figure 2-13c). From the simulated  $F_T-u$  curves we obtained the maximum force  $(F_T)_{\max}$  (strength) (Figure 2-13d). Both experiments and the model show that hinging can improve strength. Hinging becomes advantageous when the system is made from tough blocks (ductile

blocks) as in the case of polymer blocks in our experiments. In addition, because hinging depends on the elasticity of the system the strength can be improved by increased  $E$  [15].

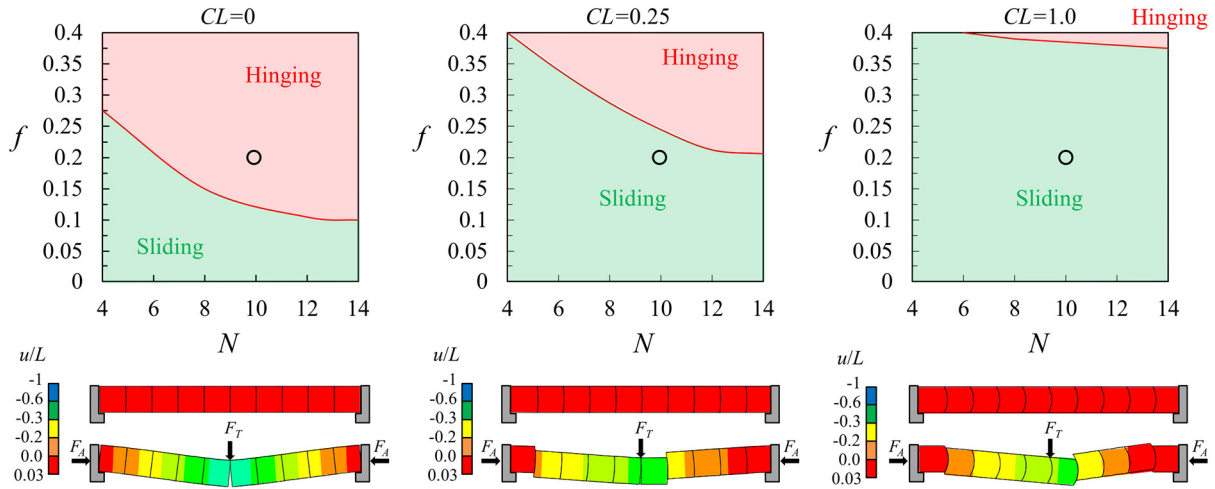


Figure 2-14: Deformations maps obtained from FE simulations for different  $(N, f)$ . Increasing the curvature  $CL$  delays hinging. For each curvature, a deformed beam simulated using FE is shown for  $(N=10, f=0.2)$ .

We used the FE model to capture the transition between sliding and hinging as function of number of blocks (focusing on even cases with  $N=4, 6, 8, 10, 12, 14$ ), as function of friction coefficient ( $f=0$  to  $0.4$ ), and as function of surface curvature ( $CL=0, 0.25, 1.0$ ), for a total of 144 simulations. Figure 2-14 shows the resulting deformation maps for the three different curvatures. Increasing the curvature  $CL$  clearly shift the failure transition mode to promote sliding (green region, Figure 2-14). The FE models shown for the case  $N=10, f=0.2$  and for each curvature clearly shows how the curved surface induced sliding and jam the blocks. In addition, the overall strength of the beam depends on the efficacy of the jamming mechanism, which is directly proportional to  $E$ . This dependence on  $E$  for jamming, is actually similar to hinging which shows that improved strength by storing elastic energy is not exclusive to hinging and that enriched systems that fail by sliding can do so by jamming. However, curved contact surfaces have the added benefit of maintaining contact between blocks which allows sliding that dissipates energy (Figure 2-14). Our simulations show that the strength increases with  $CL$  (Figure 2-15), even with no friction at the interfaces ( $f=0$ ).

For high friction,  $f=0.4$ , and low curvature ( $CL=0$  and  $0.25$ ), the blocks interlock and show signs of hinging shortly after sliding which explain the high strength values.

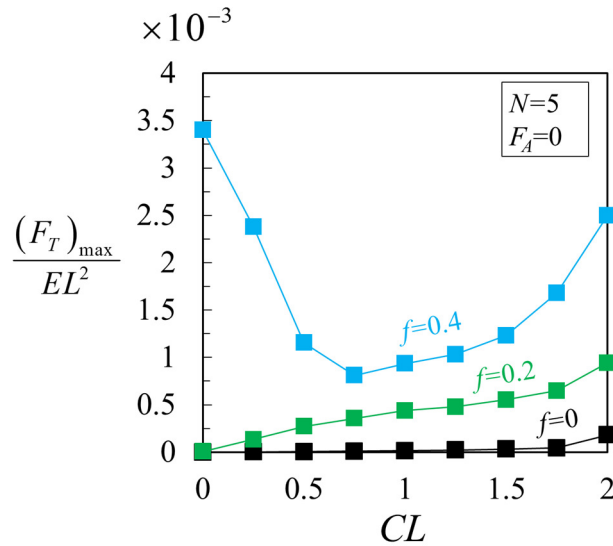


Figure 2-15: Strength  $(F_T)_{\max} / EL^2$  as function of curvature  $CL$  and for different friction coefficients  $f$ .

## 2.9 Summary

We have used experiments and modeling to explore the strength of stability of linear segmented systems made of simple cubes that interact through contact and friction. Using simple tabletop experiments with playing dice, instrumented tests on 3D printed cubes and simple models, we have highlighted the effects of axial pre-compression, number of blocks, friction coefficient and surface morphology on strength and stability. Our main conclusions are as follows:

1. Short segmented beams fail by sliding that depends on the friction coefficient  $f_s$ . Long and slender segmented beams exhibit nonlinear failure mode where three or four interfaces open into a “hinging” failure mode, with a strength which is independent of  $f_s$ .
2. The critical transverse force for sliding  $F_T^{(s)}$  decreases linearly with increasing  $N$  and nonlinearly increases with increasing friction  $f_s$ . To properly capture this effect it is necessary to consider the profile of the axial compressive stress as a superposition of the

initial axial compressive stresses and of the flexural stresses. A local criterion for the onset of micro-slips at the interface can capture the experimental results.

3. The hinging mode of failure only involves elastic deformation no sliding and poor transmission of forces between the blocks. These effects were clearly observed in the beams tested here, and are also present in topologically interlocked panels [8, 11, 15] although their direct observation is more difficult.
4. In the context of energy dissipation, toughness and stability, sliding must be promoted over hinging.
5. Relatively simple criteria for the onset of sliding or hinging were developed to predict the critical force at sliding  $F_T^{(s)}$  and hinging  $F_T^{(h)}$ . These models capture experimental results quite well. The critical sliding and hinging forces are both proportional to the initial compressive force  $F_A$ . The transition between hinging and sliding is strongly dependent on the number of blocks  $N$  and on the friction coefficient  $f_s$ , but it does not depend on the axial force  $F_A$ .
6. The morphology of the interfaces between the blocks can be enriched to delay hinging and promote sliding. Here we explored interfaces with simple curvature, which we show maximize contact between the blocks, induce sliding and progressively jam the system. These effects can be captured using finite element models. The curvature of the contact surface is an added design parameter that can be used to optimize its mechanical performance.

These findings can serve as guidelines to design tougher, stronger, reliable and damage tolerant architected beams and plates. Similar to the flat case (cube), the behavior of some architected panels are usually governed by the sliding, tilting, or jamming of the indented block (the block under the load pin). Whereas, for enriched blocks, a group of blocks slide along a designed sliding path. This study also provides insight on the mechanics of spines and helps to understand the interaction of vertebrae during transverse and axial loads. Onset of hinging and sliding may provide a mean to assess the stresses sustained by the intervertebral discs and help determine the effect of flexions (compressive bending) and extensions (tensile bending) [30]. Severe flexural deformation may cause hinging which localizes stresses and increases the likelihood of intervertebral discs herniation, as well as stretching the disc in the tensile side causing disc disruption. Besides, the spine of most reptiles is flexible [37], subjected to lower stresses [36], and

as this study may suggest is also less prone to hinging than the spines of flatter vertebrae. Finally, this study provides an example of how lateral confinement and friction (analogous to mortar shear strength) may form reliable unreinforced masonry beams. As well as predict the out of plane response of shear walls and the maximum capacity of the mortar between bricks.

## 2.10 Acknowledgements

This work was supported by a Strategic Grant (STPGP 479137-5) from the Natural Sciences and Engineering Research Council of Canada and by a Team Grant (191270) from the Fonds de Recherche du Québec – Nature et Technologies. A.D. was partially supported by a McGill Engineering Doctoral Award.

## 2.11 Appendix

### 2.11.1 Load analysis

The system in hand (Figure 2-3a) can be modeled as built in continuous beam. Consider the origin to be at the center of the beam where the shear and moment are symmetric about the origin, the moment along the beam can be written as [60],

$$\frac{M(x)}{2SF_T} = \frac{1}{8} \left( 1 - 2 \frac{|x|}{S} \right) \quad \text{for} \quad -1 \leq \frac{x}{S} \leq 1 \quad (2.11.1)$$

The magnitude of the bending moment at these locations is  $M_{\max} = F_T S / 4$  (Figure 2-6). These are the locations at which bending stresses are maximum in the beam and where the interfaces between cubes are most prone to opening.

### 2.11.2 Stress analysis

The axial stresses in the  $x$ -direction  $\sigma_{xx}$  results from the bending stress induced by the moment in the beam  $M(x)$  and from the axial compression  $F_A$ . Since the system is linear we use superposition to write  $\sigma_{xx}$  and using equilibrium equations to find the shear stress  $\tau_{xy}$ . Consider the square cross section with moment of inertia ( $I = L^4 / 12$ ) the stresses are [61]:

$$\frac{L^2 \sigma_{xx}}{F_A} = 3 \frac{y F_T}{L F_A} \frac{2S}{L} \left( -\frac{1}{2} + \frac{|x|}{S} \right) - 1 \quad \text{for} \quad -1 \leq \frac{x}{S} \leq 1 \quad (2.11.2a)$$

$$\frac{L^2 \tau_{xy}}{F_A} = -3 \frac{F_T}{F_A} \left[ \left( \frac{y}{L} \right)^2 - \frac{1}{4} \right] \quad (2.11.2b)$$

$L^2 \tau_{xy} / F_A$  follows the well-known parabolic profile, with a maximum value of  $\left( L^2 \tau_{xy} / F_A \right)_{\max} = 3F_T / 4F_A$ . Applying only axial compression  $F_A$  to the segmented system without any transverse force applied ( $F_T=0$ ) subjects the interfaces to compressive normal stress only  $L^2 \sigma_{xx} / F_A = -1$ .

### 2.11.3 Pre-sliding behavior

To find the force-displacement curve before the onset of sliding, the stresses  $\sigma_{xx}$  and  $\tau_{xy}$  can be substituted into the constitutive model (Hooke's law) of the material to find the strain components  $\varepsilon_{xx}$ ,  $\varepsilon_{yy}$  and  $\gamma_{xy}$ . Integrating the strains and applying boundary conditions we obtain the displacement along  $y$ -direction (deflection) [60],

$$u_y = \frac{3F_T}{EL^4} (|x| + S)^2 \left( \frac{S}{6} - \frac{|x|}{3} \right) \quad \text{for} \quad \partial u_y / \partial x (x = S, y = 0) = 0 \quad (2.11.3)$$

the deflection of the beam along the applied load  $F_T$  at  $x=0$  is given by

$$F_T = \frac{16EL}{N^3} u_y = \frac{16EL}{N^3} u \quad (2.11.4)$$

deflection at which sliding begins  $u=u^{(s)}$  can be expressed as

$$u^{(s)} = \frac{F_T^{(s)} N^3}{16EL} \quad (2.11.5)$$

#### 2.11.4 Post sliding behavior

The system lateral axial force relaxes when sliding start, which reduces the initial lateral compressive force  $F_A$ . The whole system losses compressive traction at the trailing edge of the sliding cubes while part of interface that are still in contact with the adjacent cube retain compressive stress. Therefore, the portion of material held in between the cubes is subjected to decreasing compressive stress of  $\sigma = F_A / L(L-u)$ . Using the constitutive relation (Hooke's law), the strain is found to be  $\varepsilon = F_A / L(L-u) = 2\Delta / NL$ , where  $\Delta$  is the axial displacement due to axial compression. Realizing that the cubes resemble spring in series, the equivalent stiffness of the system can be described by:  $K_{eq} = \frac{E(L-u)}{N}$ , using the equivalent spring equation:

$F_A = K_{eq} 2\Delta$  we get:

$$F_A(u) = \frac{F_A(L-u)}{L} \quad \text{for} \quad u^{(s)} \leq u \leq L \quad (2.11.6)$$

Setting  $u=0$  in equation (2.11.6) returns the “initial” axial compressive force (precompression)  $F_A$ . After the onset of sliding, Coulomb’s sliding criterion ( $F_{\text{interface}}^{(s)} = f_d F_A$ ) is used to capture the onset of incremental sliding at varying compressive force as function of displacement,  $F_A(u)$ . Accordingly, the force–displacement curve is described by  $F_T=2f_d F_A$  giving:

$$\frac{F_T}{F_A} = 2f_d \left(1 - \frac{u}{L}\right) \quad \text{for} \quad u^{(s)} \leq u \leq L \quad (2.11.7)$$

where  $f_d$  is the dynamic friction coefficient.

### 2.11.5 Finite element model of curved interfaces

To test the effect of interface enrichment, we modeled the architected beam using finite element (FE) (Figure 2-16). The blocks are modeled based on continuum with linear elastic behavior with Young's modulus,  $E$  and poisson's ratio  $\nu=0.2$ . The blocks are meshed using 8 nodes quadratic plane stress elements (PLANE183 [62]). The blocks are separated by contact elements (CONTA 172, [63]), that consider contact deformation and contact friction. The beam rests on rigid supports modeled as rigid contact elements (TARGE 169, [63]), the beam is subjected to axial pre-compression  $F_A$  applied at both ends ( $x=\pm L/2, y=0$ ) and to a transverse force  $F_T$  applied at  $x=0, y=L/2$ . The FE model will be used to obtain  $F_T-u$  curve for different  $CL, f, N$ . Mesh is refined until results are mesh independent, in addition it is compared with experiments for validation (Figure 2-16b).

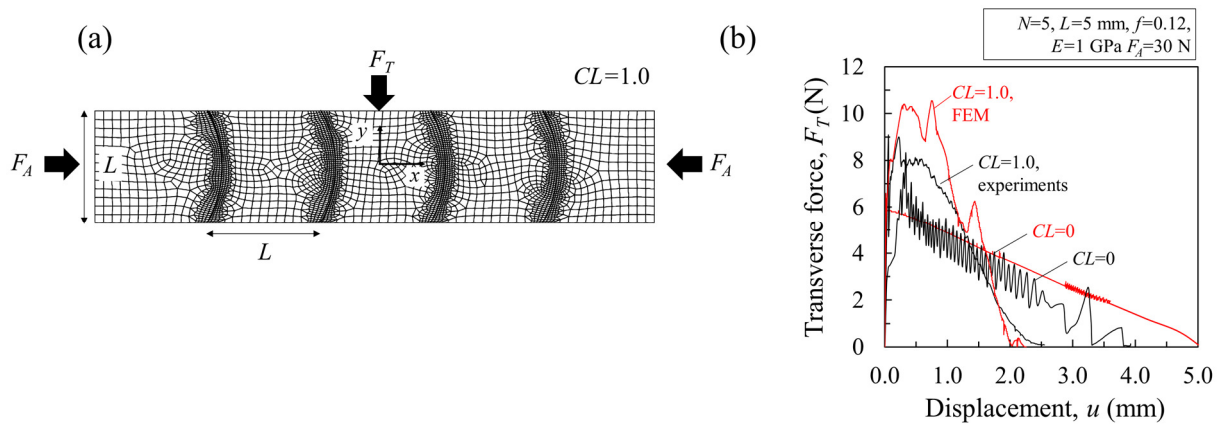


Figure 2-16: Finite element model (FE). (a) meshed beam under axial pre-compression  $F_A$  and transverse force  $F_T$ ; (b) compare FE results with experiments for validation.

### 2.12 References

1. Ashby, M.F., *Hybrids to fill holes in material property space*. Philosophical Magazine, 2005. **85**(26-27): p. 3235-3257.
2. Dalaq, A.S., D.W. Abueidda, and R.K. Abu Al-Rub, *Mechanical properties of 3D printed interpenetrating phase composites with novel architected 3D solid-sheet reinforcements*. Composites Part A: Applied Science and Manufacturing, 2016. **84**: p. 266-280.
3. Ashby, M.F., *Hybrids to fill holes in material property space*. Philosophical Magazine, 2005. **85**(26-27): p. 3235-3257.
4. Ashby, M.F., *The properties of foams and lattices*. Philosophical Transactions of the Royal Society A: Mathematical, Physical and Engineering Sciences, 2006. **364**(1838): p. 15-30.
5. Ashby, M.F., et al., *Metal Foams: A Design Guide*. 2000: Elsevier. 267.

6. Gibson, L.J., et al., *The mechanics of two-dimensional cellular materials*. Proceedings of the Royal Society of London. A. Mathematical and Physical Sciences, 1982. **382**(1782): p. 25-42.
7. Abueidda, D.W., et al., *Effective conductivities and elastic moduli of novel foams with triply periodic minimal surfaces*. Mechanics of Materials, 2016. **95**: p. 102-115.
8. Siegmund, T., et al., *Manufacture and Mechanics of Topologically Interlocked Material Assemblies*. Applied Mechanics Reviews, 2016. **68**(4): p. 040803-040803.
9. Barthelat, F., *Architected materials in engineering and biology: fabrication, structure, mechanics and performance*. International Materials Reviews, 2015. **60**(8): p. 413-430.
10. Mirkhalaf, M., J. Tanguay, and F. Barthelat, *Carving 3D architectures within glass: Exploring new strategies to transform the mechanics and performance of materials*. Extreme Mechanics Letters, 2016. **7**: p. 104-113.
11. Mirkhalaf, M., T. Zhou, and F. Barthelat, *Simultaneous improvements of strength and toughness in topologically interlocked ceramics*. Proceedings of the National Academy of Sciences, 2018. **115**(37): p. 9128-9133.
12. Ritchie, R.O., *The conflicts between strength and toughness*. Nature Materials, 2011. **10**(11): p. 817-822.
13. Dyskin, A.V., et al., *Toughening by fragmentation - How topology helps*. Advanced Engineering Materials, 2001. **3**(11): p. 885-888.
14. Wadley, H.N.G., et al., *Effect of core topology on projectile penetration in hybrid aluminum/alumina sandwich structures*. International Journal of Impact Engineering, 2013. **62**: p. 99-113.
15. Khandelwal, S., et al., *Transverse loading of cellular topologically interlocked materials*. International Journal of Solids and Structures, 2012. **49**(18): p. 2394-2403.
16. Dugué, M., et al., *Indentation of interlocked assemblies: 3D discrete simulations and experiments*. Computational Materials Science, 2013. **79**: p. 591-598.
17. Zhu, H.P., et al., *Discrete particle simulation of particulate systems: A review of major applications and findings*. Chemical Engineering Science, 2008. **63**(23): p. 5728-5770.
18. Mirkhalaf, M., A.K. Dastjerdi, and F. Barthelat, *Overcoming the brittleness of glass through bio-inspiration and micro-architecture*. Nature Communications, 2014. **5**.
19. Dyskin, A.V., et al., *Toughening by Fragmentation—How Topology Helps*. Advanced Engineering Materials, 2001. **3**(11): p. 885-888.
20. Ming-Yuan, H. and J.W. Hutchinson, *Crack deflection at an interface between dissimilar elastic materials*. International Journal of Solids and Structures, 1989. **25**(9): p. 1053-1067.
21. Barthelat, F., Z. Yin, and M.J. Buehler, *Structure and mechanics of interfaces in biological materials*. Nature Reviews Materials, 2016. **1**(4): p. 16007.
22. Wegst, U.G.K., et al., *Bioinspired structural materials*. Nature Materials, 2015. **14**(1): p. 23-36.
23. Escobar de Obaldia, E., et al., *Competing mechanisms in the wear resistance behavior of biomineralized rod-like microstructures*. Journal of the Mechanics and Physics of Solids, 2016. **96**: p. 511-534.
24. Yang, W., et al., *Natural Flexible Dermal Armor*. Advanced Materials, 2013. **25**(1): p. 31-48.
25. Szewciw, L., D. Zhu, and F. Barthelat, *The nonlinear flexural response of a whole teleost fish: Contribution of scales and skin*. Journal of the Mechanical Behavior of Biomedical Materials, 2017. **76**: p. 97-103.

26. Martini, R., Y. Balit, and F. Barthelat, *A comparative study of bio-inspired protective scales using 3D printing and mechanical testing*. Acta Biomaterialia, 2017. **55**: p. 360-372.
27. Martini, R. and F. Barthelat, *Stretch-and-release fabrication, testing and optimization of a flexible ceramic armor inspired from fish scales*. Bioinspiration & Biomimetics, 2016. **11**(6): p. 066001.
28. Chintapalli, R.K., et al., *Fabrication, testing and modeling of a new flexible armor inspired from natural fish scales and osteoderms*. Bioinspiration & Biomimetics, 2014. **9**(3): p. 036005.
29. Oxland, T.R., *Fundamental biomechanics of the spine—What we have learned in the past 25 years and future directions*. Journal of Biomechanics, 2016. **49**(6): p. 817-832.
30. Dunn, I.F., M.R. Proctor, and A.L. Day, *Lumbar spine injuries in athletes*. Neurosurgical Focus, 2006. **21**(4): p. E4.
31. Porter, M.E., R.H. Ewoldt, and J.H. Long, *Automatic control: the vertebral column of dogfish sharks behaves as a continuously variable transmission with smoothly shifting functions*. The Journal of Experimental Biology, 2016. **219**(Pt 18): p. 2908-2919.
32. Schaefer, J.T. and A.P. Summers, *Batoid wing skeletal structure: novel morphologies, mechanical implications, and phylogenetic patterns*. Journal of Morphology, 2005. **264**(3): p. 298-313.
33. Alben, S., P.G. Madden, and G.V. Lauder, *The mechanics of active fin-shape control in ray-finned fishes*. Journal of the Royal Society Interface, 2007. **4**(13): p. 243-256.
34. *Haplocanthosaurus* | Sauropod Vertebra Picture of the Week.
35. Fronimos, J.A., J.A. Wilson, and T.K. Baumiller, *Polarity of concavo-convex intervertebral joints in the necks and tails of sauropod dinosaurs*. Paleobiology, 2016. **42**(4): p. 624-642.
36. Troxell, E.L., *Mechanics of Crocodile Vertebrae*. GSA Bulletin, 1925. **36**(4): p. 605-614.
37. Molnar, J.L., et al., *Morphological and functional changes in the vertebral column with increasing aquatic adaptation in crocodylomorphs*. Open Science, 2015. **2**(11): p. 150439.
38. Robert, L.M., *A Comprehensive Classification of Shape-Variants of Vertebrae*. Turtox News, 1960. **38**(9).
39. Chen, L., et al., *Bioinspired micro-composite structure*. Journal of Materials Research, 2007. **22**(1): p. 124-131.
40. Dimas, L.S., et al., *Tough Composites Inspired by Mineralized Natural Materials: Computation, 3D printing, and Testing*. Advanced Functional Materials, 2013. **23**(36): p. 4629-4638.
41. Naleway, S.E., et al., *Structural Design Elements in Biological Materials: Application to Bioinspiration*. Advanced Materials, 2015. **27**(37): p. 5455-5476.
42. Barthelat, F., Z. Yin, and M.J. Buehler, *Structure and mechanics of interfaces in biological materials*. Nature Reviews Materials, 2016. **1**(4).
43. Fratzl, P., et al., *The mechanics of tessellations - bioinspired strategies for fracture resistance*. Chemical Society Reviews, 2016. **45**(2): p. 252-267.
44. Barthelat, F., *Designing nacre-like materials for simultaneous stiffness, strength and toughness: Optimum materials, composition, microstructure and size*. Journal of the Mechanics and Physics of Solids, 2014. **73**: p. 22-37.
45. Begley, M.R., et al., *Micromechanical models to guide the development of synthetic 'brick and mortar' composites*. Journal of the Mechanics and Physics of Solids, 2012. **60**(8): p. 1545-1560.

46. Mirkhalaf, M., et al., *Toughness by segmentation: Fabrication, testing and micromechanics of architected ceramic panels for impact applications*. International Journal of Solids and Structures, 2018.
47. *EnvisionTEC | Desktop, Professional and Industrial 3D Printers*. EnvisionTEC 2018/04/20/20:18:21; Available from: <https://envisiontec.com/>.
48. Dawood, A., et al., *3D printing in dentistry*. British Dental Journal, 2015. **219**(11): p. 521-529.
49. Studart, A.R., *Additive manufacturing of biologically-inspired materials*. Chemical Society Reviews, 2016. **45**(2): p. 359-376.
50. Tumbleston, J.R., et al., *Continuous liquid interface production of 3D objects*. Science, 2015. **347**(6228): p. 1349-1352.
51. ASTM, *Standard Test Method for Static and Kinetic Coefficients of Friction of Plastic Film and Sheeting ( D1894 )*. 1894, ASTM.
52. Berman, A.D., W.A. Ducker, and J.N. Israelachvili, *Origin and Characterization of Different Stick–Slip Friction Mechanisms*. Langmuir, 1996. **12**(19): p. 4559-4563.
53. Menezes, P., et al., *Tribology for Scientists and Engineers: From Basics to Advanced Concepts*. 2013, New York: Springer-Verlag.
54. Johnson, K.L., *Contact Mechanics*. 1987: Cambridge University Press. 472.
55. Ben-David, O. and J. Fineberg, *Static friction coefficient is not a material constant*. Physical Review Letters, 2011. **106**(25): p. 254301.
56. Ben-David, O., G. Cohen, and J. Fineberg, *The Dynamics of the Onset of Frictional Slip*. Science, 2010. **330**(6001): p. 211-214.
57. Rubinstein, S.M., G. Cohen, and J. Fineberg, *Detachment fronts and the onset of dynamic friction*. Nature, 2004. **430**(7003): p. 1005-1009.
58. Kammer, D.S., et al., *Linear Elastic Fracture Mechanics Predicts the Propagation Distance of Frictional Slip*. Tribology Letters, 2015. **57**(3): p. 23.
59. Scheibert, J. and D.K. Dysthe, *Role of friction-induced torque in stick-slip motion*. EPL (Europhysics Letters), 2010. **92**(5): p. 54001.
60. Ross, C.T.F., T.I.J. Case, and A. Chilver, *Strength of Materials and Structures*. 1999: Elsevier. 721.
61. Timoshenko, S. and J.N. Goodier, *Theory of Elasticity, by S. Timoshenko and J.N. Goodier, ... 2nd Edition*. 1951: McGraw-Hill Book Company. 506.
62. ANSYS, *ANSYS Mechanical APDL Modeling and Meshing Guide*. 2013, ANSYS, Release 15.0.
63. ANSYS, *ANSYS Mechanical APDL Contact Technology Guide*. 2013, ANSYS, Release 15.0.

## Link between chapter 2 and chapter 3

In chapter 2, some fundamental aspects of segmented beams were explored. Possible failure modes are highlighted and a round shape enrichment for individual blocks is proposed. More specifically, rounding at the contact faces improved strength and changed the overall behavior and the failure mode of architected beams. The geometry of the blocks may therefore be a major parameter for designing tougher and stronger architected beams. Until this point, the possibility of fracture of individual blocks was ignored and it was assumed that the blocks had infinite strength. The next chapter is a journal article which is currently under review for the journal: *Materials & Design*. This chapter explores the effect of geometry of blocks by parametrizing the contact faces of blocks with 2D polynomial functions. Therefore, the blocks are incrementally enriched, starting with a constant term (a flat contact face), up to third order terms. This approach transformed contact faces of blocks from a flat face (cube design), tilted planar faces, curved (round) to wavy contact faces. The model also incorporates the fracture of individual blocks from local stresses at the points of contact. The model can predict the strength, toughness and the onset of fracture of the system, which is then used to find optimum designs and compare with experiments.

---

## Chapter 3

Manipulating the geometry of architected beams for  
maximum toughness and strength

---

# Chapter 3: Manipulating the geometry of architected beams for maximum toughness and strength

Ahmed S. Dalaq<sup>1</sup>, Francois Barthelat\*<sup>1,2</sup>

1: Department of Mechanical Engineering, McGill University, 817 Sherbrooke Street West,  
Montreal, QC H3A 2K6, Canada

2: Department of Mechanical Engineering, University of Colorado, 427 UCB, 1111 Engineering  
Dr, Boulder, CO 80309, United States

## 3.1 Abstract

Dense architected materials are made of blocks that can slide, rotate, interlock and jam in powerful mechanisms that can generate simultaneous strength and toughness. Nature abounds of examples of such architected materials, for example in the segmented structure of vertebrate spines. In this study we consider segmented beams made of stiff blocks and submitted to a transverse force. We start with simple cubes as a geometrical reference, which we then enrich by using two-dimensional polynomial functions. The flexural response of the beam is simulated using finite element modeling (FE-model) to predict strength, toughness and maximum local stresses. Using this procedure we identified the most efficient interface geometries and interlocking mechanisms within a set of polynomial functions and for a given strength of the individual blocks. To illustrate these results, we fabricated segmented beams of ceramic glass using a laser engraver. Experiments on these architected glass revealed how enriched blocks turned the catastrophic brittle failure of monolithic glass into graceful progressive deformation. Resulting in a tougher response than the monolithic by 370 times and preserved 40% of strength of that of the monolithic.

**Keywords:** Architected materials, segmented materials, structural stability, topologically interlocking materials (TIMs)

## 3.2 Introduction

Toughness and strength are mutually exclusive properties in engineering materials. For example ceramics are hard and strong against deformation, but they can only undergo small deformation and they are brittle. For many applications there is a pressing need to combine strength and toughness in one material, especially when materials are subjected to unanticipated loads. Weight is an equally important property to minimize in order to reduce carbon emissions of vehicles, produce more slender structures and allow for bolder outer space explorations. For reducing weight, many brittle materials such as glass, clay and some ceramics are relatively light and inexpensive [1]. While these materials are brittle they are also relatively stiff, corrosion resistant, abrasion resistant and have low thermal expansion [2, 3]. Some of these materials, for example glasses, are also transparent. The toughening of these brittle materials is a major challenge which may allow their use as structural components: beams, shock absorbers, trusses and frames. Architected and segmented materials are powerful approaches to toughen brittle materials (Figure 3-1a). Segmentation is prominent in masonry structures, particularly in monuments, shear walls and domes [4, 5]. In addition, the field of pavement design is rich with design templates and tessellations applicable to architected materials [6]. Masonry structures have recently inspired topologically interlocked materials (TIMs) which rely on the geometrical interlocking of relatively stiff blocks [7-9]. TIMs can contain cracks and improve toughness [7-13]. The shapes of individual blocks range from simple cubes, tetrahedrons, octahedron to more complex osteomorphic blocks [11, 14, 15] (Figure 3-1b). Individual blocks are relatively stiff, and their deformations are typically small and within elastic limits. However the interfaces between the blocks are more compliant and weaker, so they can channel deformations and arrest cracks [16-19]. The blocks can also rotate (hinge), slide, separate, interlock and jam, generating powerful mechanisms for improving toughness and strength [11, 20, 21]. The blocks may be held together and confined by external ligaments such as stiff frames, internal tension cables, springs or pre-compressed supports to manipulate contact and friction forces [9, 22-25]. Architected materials and structures are information-rich and highly tunable (e.g. dimensions, shapes, elastic modulus, surface friction and number of blocks), a feature which suits itself to optimization.

Interestingly, hard natural materials such as wood, mollusk shells, bone, teeth or even entire skeletons are also made of stiff but brittle “building blocks” with remarkably uniform geometries

and arrangements [17, 26, 27]. The interaction of shape, size, composition, orientation, arrangement of blocks, interface geometry along with soft protein bonding at the interfaces which can generate nonlinear viscoelastic and contact-based deformations, lead to remarkable combinations of stiffness, strength and toughness. The arrangement of the blocks vary from linear arrays as in fish fins and spines [28-31] (Figure 3-1c) to 2D arrangement like the tesserae in sharks [32] to more complex decussations of mineralized rods in teeth enamel [17]. Both fish fins and vertebrate spines are composed of mineralized blocks arranged linearly and bonded with soft collagenous membranes (Figure 3-1c, d, e) [28-31]. The shape of the blocks, and specifically the geometry of the interface, may vary across species and biological components, giving rise to specific properties and functionalities (Figure 3-1c, d, e, f). The geometry of the interface may vary from straight interfaces as in fish fins and vertebrae of orcas (Figure 3-1c, d), to slightly curved interfaces in crocodiles (Figure 3-1e) to complex serrated sutures between blocks in ammonites (Figure 3-1f) [34, 35]. Some reptiles including crocodiles have concave and/or convex round interfaces between their vertebrae [36-38], which allows for a high range of motion for their spine. Direct applications of segmented systems include armor, glass facades, shields, robotic arms, deployable and anti-seismic structures [17, 25, 39].

Previous studies applied strategies of nature in architected materials achieved some improvements, but at the expense of strength [9, 12, 40]. In particular, linearly segmented materials similar to spines have not been studied extensively to this day. In a previous study, we found that the behavior of a segmented beam depends on the number of blocks, friction and interface designs between blocks [41]. In a previous study we found how the segmentation of glass panel into rectangular prisms with flat interfaces improves toughness, strength and the damage tolerance of glass [39]. In addition to segmentation, an equally important aspect of segmented materials is the geometry and arrangement of the blocks (architecture). Upon studying the effect of blocks geometry, we also discovered that round interfaces (concavo-convex) affect failure modes (e.g. sliding or rotation of blocks), they induce curved sliding of blocks with jamming during deformation [41]. Although that previous study indicated the key parameters governing the failure mode of segmented systems, the study was limited to two-dimensional geometries and to an interface with a single curvature. In addition, this previous study ignored internal stresses in individual blocks and their potential failure. It is also unclear, from the existing literature, how incorporating 3D-geometrical enrichments of contact surfaces (2D-parameterized surfaces) affects

the behavior of segmented systems including strength, failure modes and mechanical stability. Here in this study we systematically enrich the geometry of the interfaces between the blocks to explore and optimize its effect on stability, combined stiffness, strength and toughness. This systematic enrichment of contact interfaces provides general guidelines for the strength and toughness of sliding segmented systems based on a general geometric parameter.

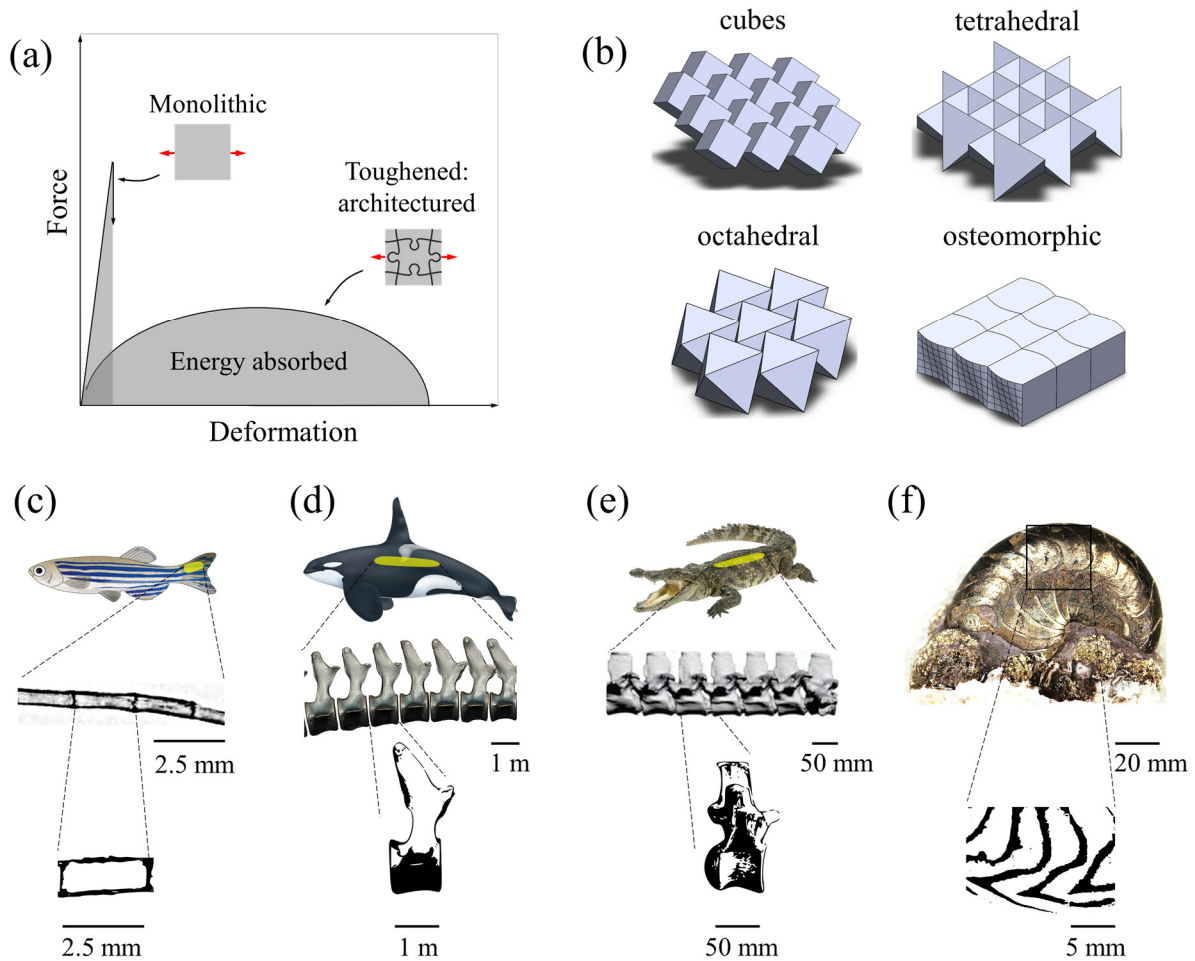


Figure 3-1: (a) Typical force–displacement curves of architected materials versus monolithic materials; (b) topologically interlocked materials (TIMs). Linearly segmented architected materials in nature: (c) fish fins of zebrafish (adapted from [40]), (d) vertebrae of orca (adapted from [32]), (e) concavo-convex vertebrae in the spines of crocodiles (adapted from [37]) and (f) goniatite (adapted from [34]).

### 3.3 Model setup and enrichment of cubes with fillets

For this study we considered idealized segmented beams composed of  $N=5$  identical blocks with dimensions  $L \times L \times L$ . The blocks are aligned in a single row between two rigid supports (Figure 3-2a). They are modeled as linear elastic (modulus  $E$ , Poisson's ratio  $\nu$ ), with contact elements inserted at the interfaces between the blocks, and also between the end blocks and the rigid supports. The end supports are used to impose a pre-compression force  $F_A$  that holds the row of blocks in place by dry friction (friction coefficient  $f$ ). To assess the strength and stability of this segmented beam we apply a transverse displacement  $u$  at the center of the beam (coordinates  $(5L/2, L/2, L/2)$ ) that is progressively increased until collapse of the system. The corresponding reaction force is the transverse force  $F_T$  which is recorded at each increment of the transverse displacement  $u$ .

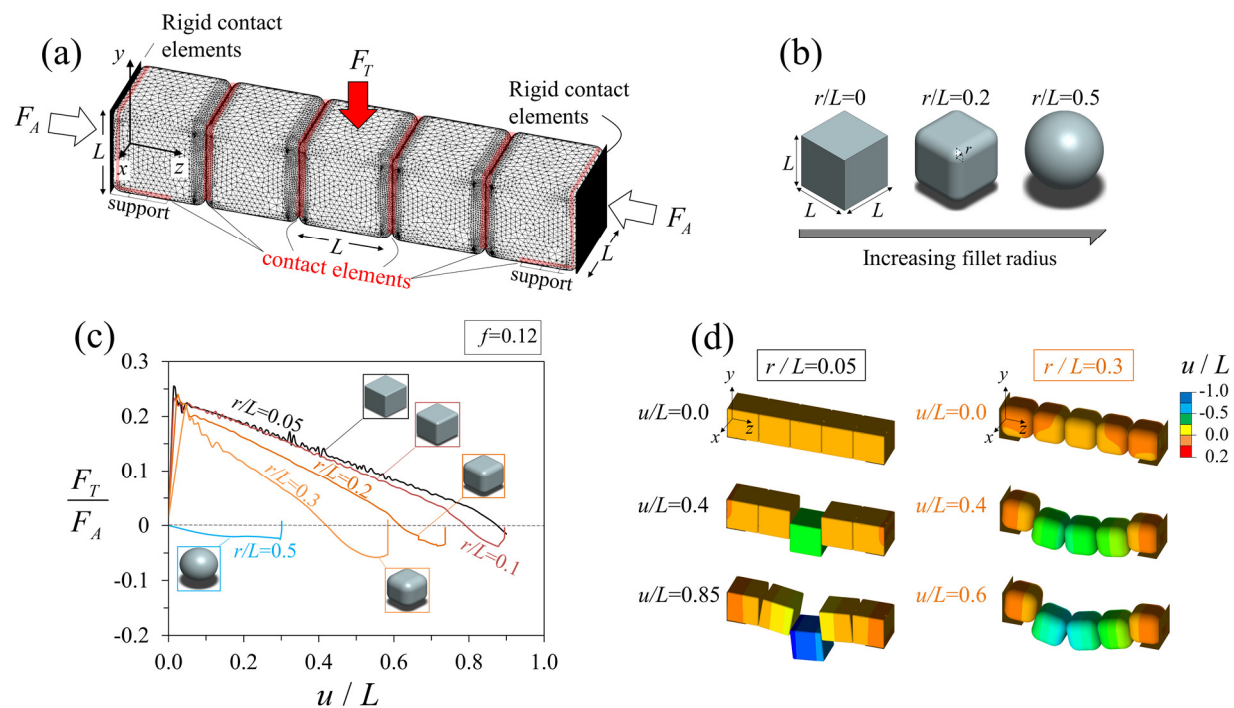


Figure 3-2: (a) Finite element model: blocks are meshed and mesh refinement is applied at edges and corners; (b) the cube is enriched by rounding the edges and corners with fillets from  $r/L=0$  to  $r/L=0.5$  where finally the cube is transformed into a sphere. Effect of applying fillets  $r/L$  on (a)  $F_T-u$  curves and (b) deformation.

A simple starting point for this study is a segmented beam made of cubes, a system we recently investigated to reveal the importance of friction and number of blocks on overall strength, failure

mode and stability [41]. 3D finite element models (FE-model) with different fillet radii were automatically generated and simulated using a combination of Matlab and Ansys-APDL (Appendix 3.9.1). Mesh convergence was verified in all the results presented in this chapter. Since the state of stress in the system have no particular length scale, all dimensions were normalized by the size of the blocks  $L$ . It is known from the contact mechanics of elastic punches [22, 23] that the contact stresses at the corners of cubes are infinite. To prevent the stress from reaching these singularities and for a more realistic model, we rounded all edges and corners of the cubes with a fillet of radius  $r/L$  (Figure 3-2b). These fillets enabled stress convergence at the edges and corners of the cubes, and also ensured mesh independent results. Rounding of the corners and edges of the blocks acted as a first level of geometrical enrichment for the cube-based segmented beams, with significant impact on the strength and stability of the architected beam. To assess the effect of fillet radius  $r/L$  we ran FE-models for beams made of blocks with  $r/L=0.05, 0.1, 0.2, 0.3, 0.5$ . The sliding of the blocks is governed by frictional forces, which are in turn governed by the pre-compression  $F_A$ . More specifically, we verified that the transverse force is proportional to the axial pre-compression, so that the results can be displayed as normalized force  $F_T/F_A$  without loss of generality. The force-displacement curves,  $F_T-u$  for different  $r/L$  show a linear increase in transverse force  $F_T$  (for  $r/L<0.5$ ) until a maximum  $F_T$  is reached at the onset of sliding (Figure 3-2c). After this linear elastic part, the block(s) start sliding progressively (Figure 3-2d), which is associated with a decrease of the compressive force  $F_A$ : sliding the blocks reduces the volume of elastically deformed material held between rigid supports which in turn decreases the axial stiffness of the beam. As a result of the decrease of axial force the friction force at the interface decreases, and  $F_T$  decreases almost linearly with increasing  $u$  (Figure 3-2c). At a critical displacement the sliding block(s) completely loses contact and the center block is being pushed out (first column on Figure 3-2d for  $u/L=0.85$ ). At this point the transverse force becomes compressive ( $F_T < 0$ ) which indicates the tendency of the sliding blocks(s) to “eject” out of the system. This general  $F_T-u$  behavior was observed for all radii  $0.1 < r/L \leq 0.5$ , but the specific overall properties of the beam varied with  $r/L$ . Increasing  $r/L$  led to a significant decrease in initial stiffness, to a slight decrease in strength, and to a more rapid instability in the system. For example, increasing the fillet radius from  $r/L=0.1$  to  $r/L=0.3$  decreased the maximum displacement by 50% (Figure 3-2c). For  $r/L=0.3$ , a group of blocks sled and gradually started rotating, which are signs that the system is transitioning from a sliding failure mode into a “hinging” failure mode [41]

(second column on Figure 3-2d). Sphere-based beams ( $r/L=0.5$ ) are highly unstable and the transverse force is negative over the entire simulation. In these simulations we also monitored the maximum tensile stresses  $(\sigma_1)_{\max}$  occurring within the blocks, in order to predict damage and fracture (we assumed brittle blocks). A typical snapshot from FE-model of the maximum (principal) stress contours for  $r/L=0.3$  and at  $u/L=0.5$  is shown on Figure 3-3a. As expected from the contact mechanics of frictional sliding, the maximum tensile stress occurs at the trailing edge of the contact area. Figure 3-3b shows the evolution of the maximum tensile principal stress during deformation for different  $r/L$ . We verified that the maximum stress  $(\sigma_1)_{\max}$  is always proportional to  $F_A$ , so we used  $(\sigma_1 L^2 / F_A)_{\max}$  as a non-dimensional number to characterize the maximum principal stresses in the blocks. These stresses increase linearly with  $u/L$  until the onset of sliding at  $u/L=0.035$  marking the first peak, after which  $(\sigma_1)_{\max}$  falls sharply. The stresses then increased gradually as the contact area decreased and the contact pressure increased. The maximum stress reached another maximum value well into the sliding of the blocks at  $u/L>0.4$  (marked with a red dot on Figure 3-3b). Afterward the stress decreased continuously until complete failure. In general the maximum stress was the highest for small  $r/L$ , except for the extreme case  $r/L=0.5$  (sphere) where the maximum stresses were comparatively very high.

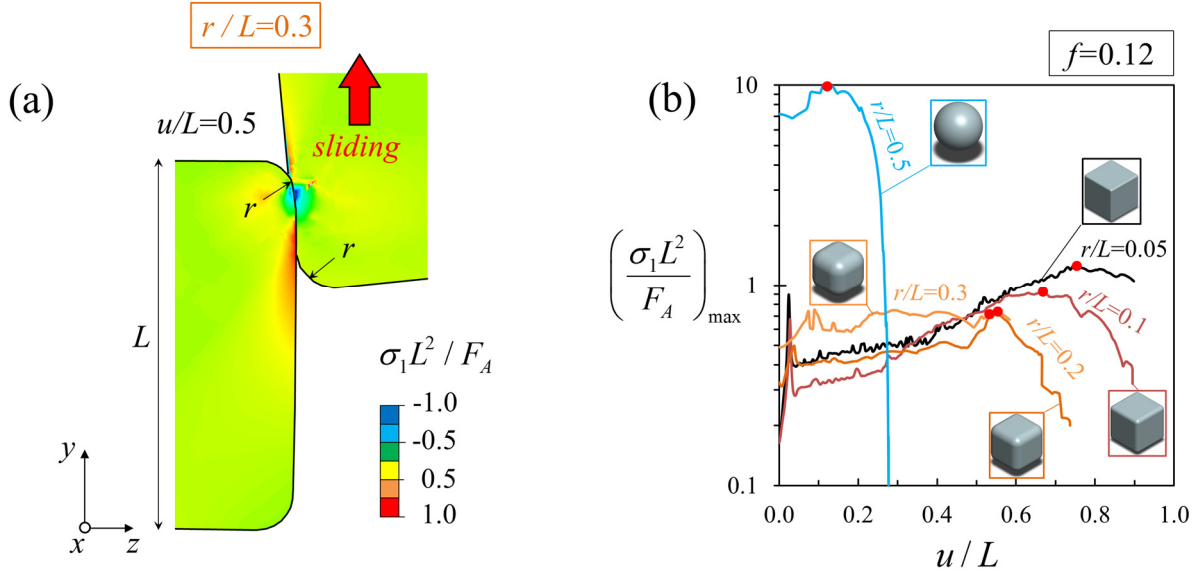


Figure 3-3: Normalized maximum principal stresses in the segmented beam during deformation; (a) stress contours in the blocks at  $u/L=0.5$  for  $r/L=0.3$ ; (b) maximum principal stress variation during deformation,  $(\sigma_1)_{\max} - u$  curves, the point of maximum stress is denoted by a red dot marker.

Assuming that the blocks are made of a brittle material, we used a simple failure criterion: the blocks fractured when the maximum principal stress exceeds the tensile strength  $\sigma_s / E$ . We therefore truncated the  $F_T - u$  curves at the point at which  $(\sigma_1)_{\max} / E \geq \sigma_s / E$ , and the remaining first part of these curves were used to compute the toughness  $U_{\max}$  and the strength  $F_{\max}$  (Appendix 3.9.2, Figure 3-15). Figure 3-4 shows a toughness-strength map for segmented beams made of blocks with different rounding. The case with no rounding ( $r/L=0$ ) and perfectly sharp cubes is a theoretical case where the stresses are infinite, and where the blocks immediately fracture upon sliding. As a result the toughness and strength are zero for  $r/L=0$  (Figure 3-4b). For  $r/L=0.025$ , the stresses are high, the blocks therefore fracture which results in a truncated  $F_T - u$  curve with little deformation. Conversely, for  $r/L=0.05$ , the stresses are lower than  $r/L=0.025$  where the beam deformed without fracture, resulting in the highest toughness and highest strength. For  $0.1 \leq r/L < 0.3$ , the inherent lower maximum force and displacement of these cases result in lower strength and toughness than  $r/L=0.05$ . According to Figure 3-4 the optimum values are  $r/L=0.025$  and  $r/L=0.05$  for highest strength and toughness respectively.

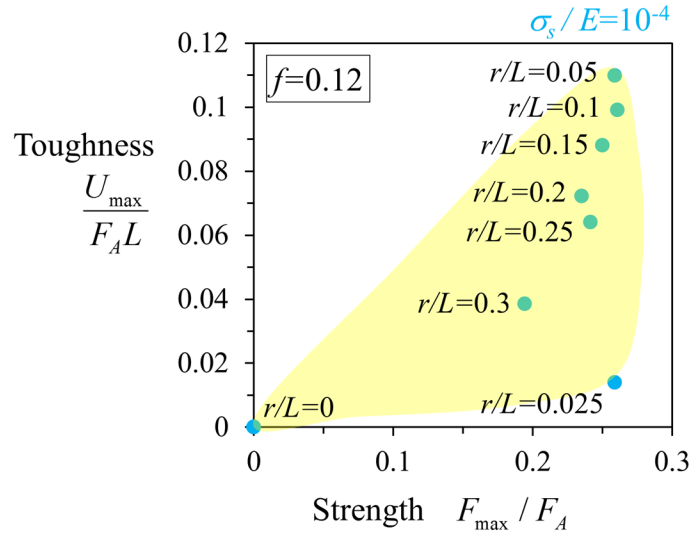


Figure 3-4: Toughness–strength map for segmented beams made of blocks with different rounding.

### 3.4 Geometrical enrichments with polynomial functions

Using the same approach for model generation, finite element modeling and data processing we then considered more complex geometric enrichments for the blocks. One objective was to generate progressive interlocking between the blocks, in order to achieve better combinations of strength and toughness. To enrich the geometry of the blocks we considered contact surfaces that followed polynomial equations of the form:

$$z(x, y) = \sum_{i,j} a_{i,j} x^i y^j \quad (3.1)$$

The contacting surfaces of every block followed equation (3.1), which ensured that the initial contact surfaces were conformal. Individual terms and their combinations can be visualized with the Pascal’s triangle shown on Figure 3-5. The curvature and waviness of the blocks are clearly more pronounced as the order of the monomial  $i+j$  is increased. Enrichments that are a single function of  $x$  or  $y$  transform contact faces along a single direction resulting in a curved “extruded-like” designs, while multivariable monomials transform the contact faces in both directions resulting in more wavy designs. Both the deformation and  $F_T-u$  curves generated by the finite element model was validated with experiments before conducting a full study on all designs (Appendix, 3.9.1, Figure 3-14).

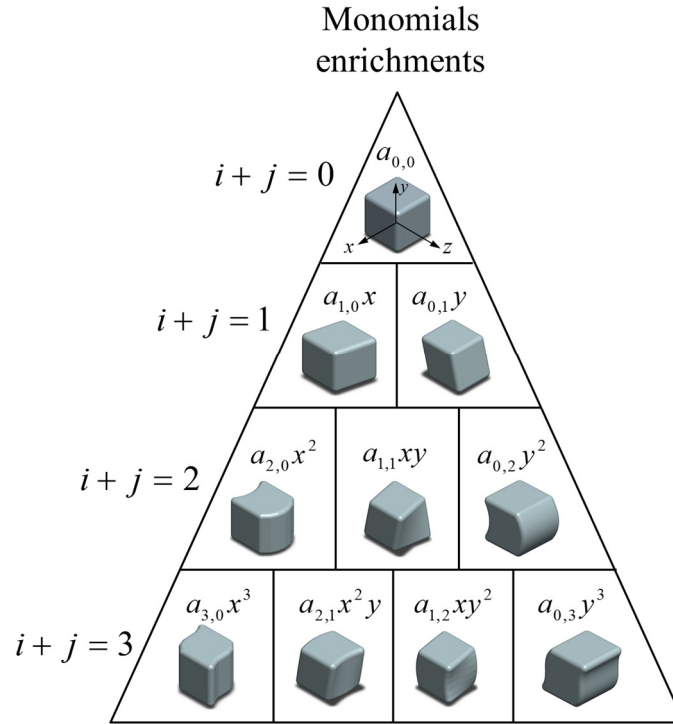


Figure 3-5: Enriching the contact surfaces between blocks with 2D-monomial functions. Pascal triangle depicting individual terms; the degree of the polynomial  $i+j$  increases from top to bottom.

Additional shapes can be generated by combining the monomials of Figure 3-5. Because of the high computational cost of the densely meshed 3D-models we limited this study to binomials. We did not pursue single variable monomials along  $x$  as  $z(x) = a_{i,0}x^i$  because they do not provide interlocking. Likewise, we excluded the hyperbolic-paraboloid:  $z(y) = a_{1,1}xy$  which are unstable for large  $a_{1,1}$ . Asymmetric designs about  $y$ - $z$  plane like  $z(y) = a_{1,2}xy^2$  undergo extremely high stresses and allow for little sliding (limited deformation). In addition, the contact faces of the asymmetric designs channel forces along  $x$ -direction where there is no contact-based resistance at end supports to hold the structure together and maintain stability. We therefore excluded these asymmetric designs and considered only symmetric ones which are a total of 4 designs. We explored all possible combinations of these symmetric monomials. The order in combining these monomials is irrelevant therefore all possible combinations are given by;  $C(2,4)$  combinations which results in a total of:  $C(2,4) = 4! / 2!(4-2)! = 6$  combinations, where  $C$  represents combinations and  $(!)$  represents the factorial. Figure 3-6 shows the monomials we combined to

form different binomials. The resulting binomial functions are shown above each design. The coefficients  $a_{i,j}$  of the polynomial function can be varied to change the amplitude of the surface  $A$ , which can be found with:

$$A = |z(x_{max}, y_{max}) - z(x_{min}, y_{min})| \quad (3.2)$$

where  $x_{min}$ ,  $y_{min}$ ,  $x_{max}$ , and  $y_{max}$  are the  $x$ ,  $y$  location of the maximum and minimum points of  $z(x, y)$ . The coefficient  $a_{i,j}$  are varied such that the amplitude is  $A/L \leq 0.5$ . The edges and corners of all designs were rounded with a fillet radius of  $r/L = 0.1$ .

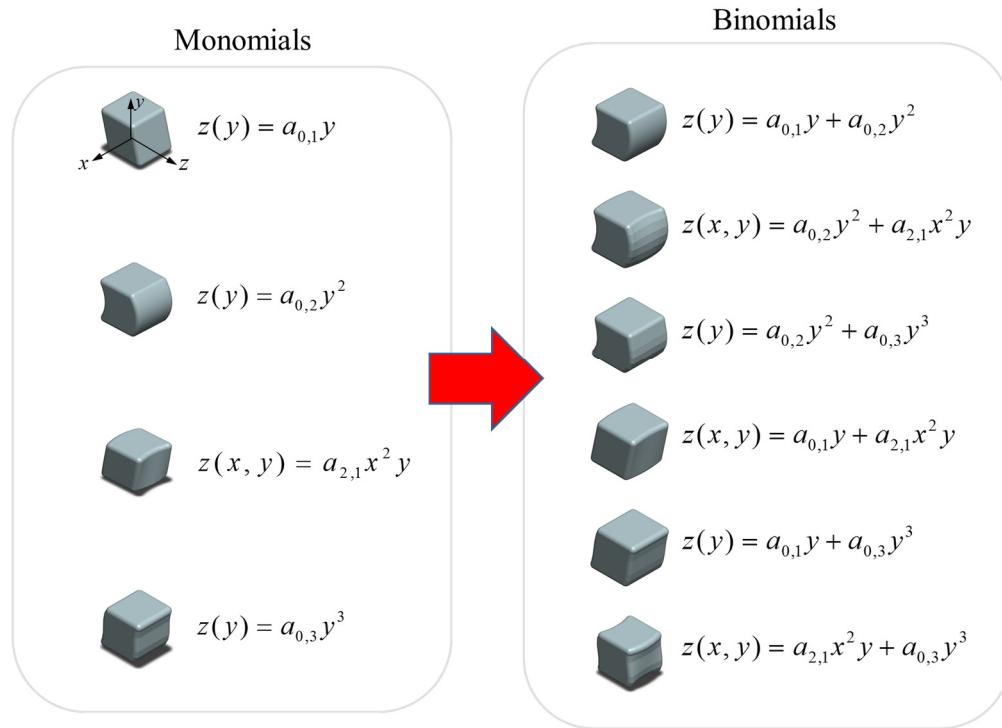


Figure 3-6: Combining monomials to form binomials.

Figure 3-7 shows some examples of  $F_T-u$  curves for the enriched designs. Figure 3-7a is a design with  $z(x) = a_{2,0}x^2$ , a profile that produces little interlocking along the sliding direction and which produces a response comparable to the cube cases described above. Designs that included terms that are a function of  $y$  were more successful: they generated a progressive interlocking that increased  $F_T$  during deformation (Figure 3-7b). The axial compressive force decreases as the

blocks slide, which decreases the efficacy of jamming between blocks. There is a competition between geometric hardening and softening during the loss of contact which results in a maximum force, followed by softening until complete failure. The progressive interlocking is more pronounced for the multivariable monomial:  $z(x, y) = a_{1,2}xy^2$  (Figure 3-7c), which is a wavy contact face. In addition, this multivariable monomial shows a more stable response, resulting in a maximum displacement that is 1.5 times higher than  $z(y) = a_{0,2}y^2$  for  $a_{i,j} = 0.4$ . Adding a plane term:  $z(y) = a_{0,1}y$  to the  $z(y) = a_{0,2}y^2$  forms a tilted-parabolic profile for the contact faces that improved stability by prolonging the progressive interlocking during deformation (Figure 3-7d). Finally, adding the cubic profile:  $z(y) = a_{0,3}y^3$  to  $z(x, y) = a_{1,2}xy^2$  generated more interlocking which increased the maximum force (strength) (Figure 3-7e). For all cases, increased amplitude (higher  $a_{i,j}$ ) increased strength, but at the expense of maximum displacement (i.e. stability).

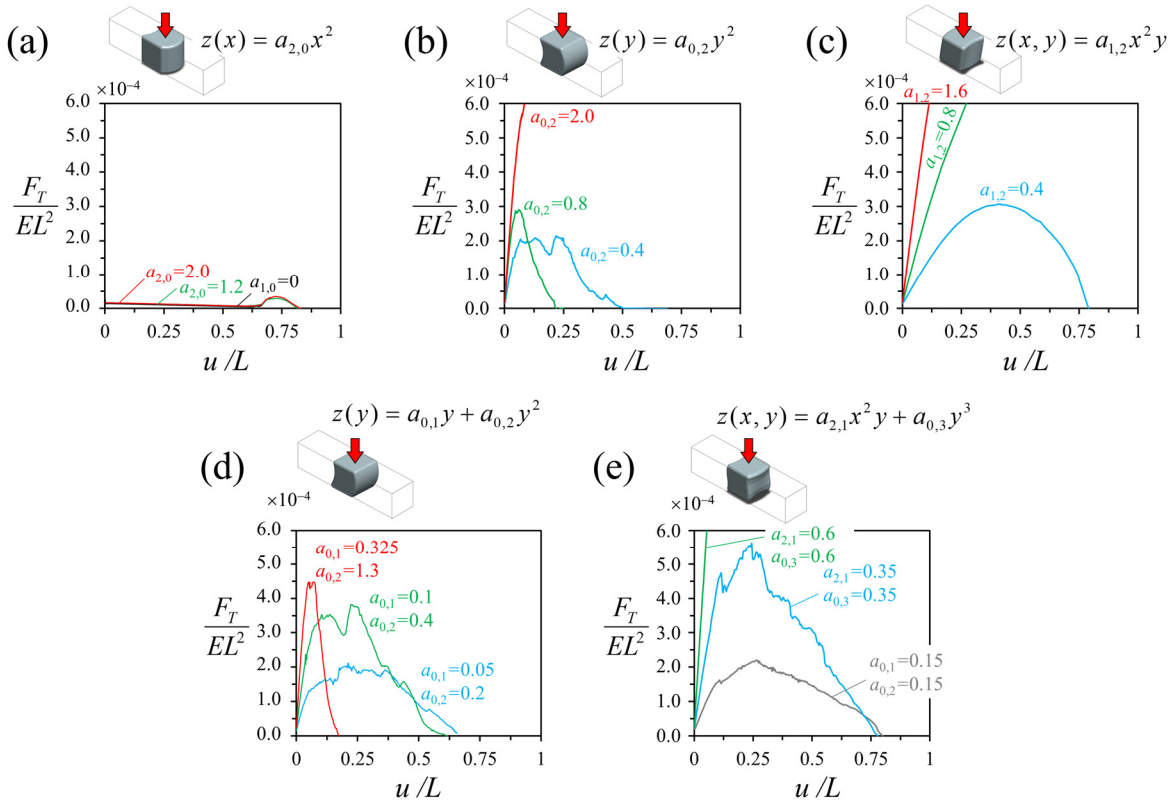


Figure 3-7: Force–displacement,  $F_T$ – $u$  curves for (a)  $z(x) = a_{2,0}x^2$ , (b)  $z(y) = a_{0,2}y^2$  and (c)  $z(x, y) = a_{1,2}xy^2$ , (d)  $z(y) = a_{0,1}y + a_{0,2}y^2$  and (e)  $z(x, y) = a_{2,1}x^2y + a_{0,3}y^3$ ; the plots are reported for  $f=0.12$ .

Figure 3-7 highlights the profound effect of surface geometry on the mechanical response of the architected beams. It is then possible to rank the efficacy of these particular designs by strength, by toughness (total area under the  $F_T-u$  curve), or by a combination of the two. Importantly we note that both  $F_{\max}$  and  $U_{\max}$  are directly proportional to the friction coefficient  $f$ , provided that  $0 < f \leq 0.3$  and that the structures fail by sliding. Therefore, we normalized both  $F_{\max}$  and  $U_{\max}$  by  $f$ . Figure 3-8a shows the maximum normalized strength and toughness for each design considered here. The cube-based designs produced the lowest strength and energy absorption, while the wavy design  $z(x, y) = a_{2,1}x^2y + a_{0,3}y^3$  produced the highest strength and toughness. We previously studied round interfaces (concavo-convex geometry [41]) which generated improvement in strength and toughness. This simple round design (denoted by filled circular marker) underperformed compared to almost all multivariable wavy designs. For example it only achieved 0.07 the strength and toughness produced by blocks with waviness  $z(x, y) = a_{2,1}x^2y + a_{0,3}y^3$ . Figure 3-8a shows that there is a strong correlation between strength and toughness for the designs tested here. The results suggest that wavier designs produced higher strength and toughness in comparison to flat and less curved designs. This observation may be confirmed quantitatively by considering a single geometric parameter to characterize the degree of “waviness” in the design. Here we define a normalized surface curvature  $\phi L$ , computed from derivatives of the surface in both directions, and which echoes the definition of curvature for 1D functions [43]:

$$\phi L = \frac{\frac{1}{L} \left\langle \frac{\partial^2 z}{\partial y^2} + \frac{\partial^2 z}{\partial y \partial x} \right\rangle}{\left\langle \frac{\partial z}{\partial y} + \frac{\partial z}{\partial x} \right\rangle} \quad (3.3)$$

The chevrons  $\langle \rangle$  denote mean values computed over the entire surface. The numerator of equation (3.3) puts a stronger emphasis on variations along  $y$  to capture waviness along the loading direction. We calculated  $\phi L$  for different designs and Figure 3-8b shows how wavier and curvier contact faces translate into higher  $\phi L$  values, and therefore we used  $\phi L$  as a metric for geometrical waviness of the different designs. It is then useful and instructive to assess how the single waviness parameter  $\phi L$  governs the mechanical performance of the architected beam.

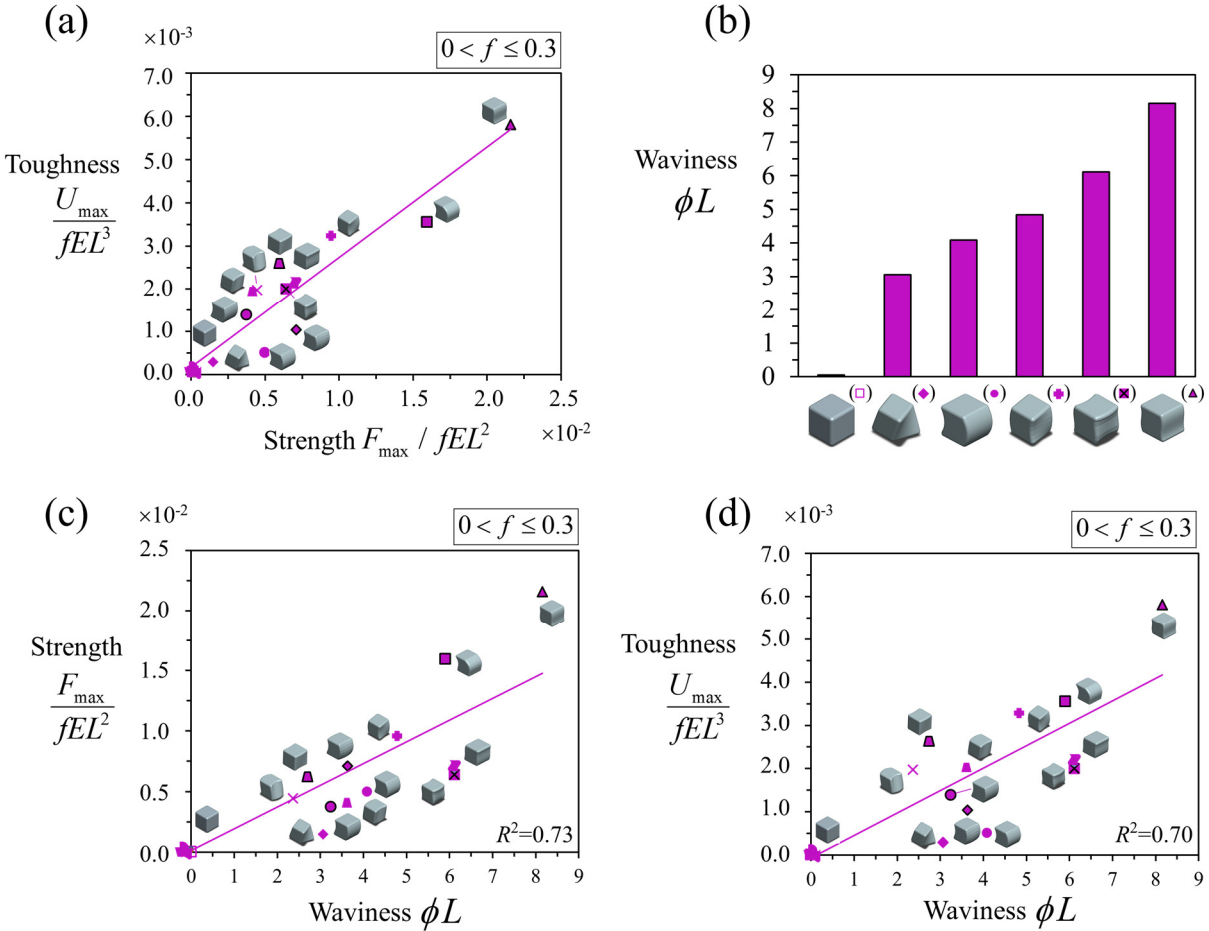


Figure 3-8: (a) Normalized maximum strength  $F_{max}$  and toughness  $U_{max}$ ; (b) the geometric metric  $\phi L$  for different designs. Normalized (c) strength relationship and (d) toughness with  $\phi L$ .

Figure 3-8c and 3-8d show the strength and toughness plotted as function of  $\phi L$  for the different designs explored here. The plots show that the waviness parameter  $\phi L$  can be used as an approximate predictor of strength and toughness for the architected beam. This feature can be useful to predict the efficacy of other designs without recourse to FE analysis. The scatter in the plots was attributed to the inherent instability of certain shapes. The friction coefficient  $f$  and the number of blocks  $N$  are the main contributors to changing the failure mode of such structures [41], therefore for sliding cases the waviness parameter  $\phi L$  may be general and applicable for

predicting both toughness and strength of such architected beams. Further studies are needed to assess the applicability of  $\phi L$  for different enrichment types and/or different loading conditions.

### 3.5 Optimization of monomials and binomials for finite strength of blocks

A limiting factor in the amount of interlocking between the blocks is the strength of the blocks themselves. In order to bring this factor into the design of the blocks we tracked the stresses during the entire simulations. Figure 3-9 shows the maximum principal stress  $(\sigma_1)_{\max}$  during deformation for three designs. For the case  $z(x) = a_{1,0}x$ , the absence of interlocking along the loading direction leads to negligible stresses (Figure 3-9a). For the curved design  $z(x) = a_{2,0}x^2$ , the maximum stress increases with interlocking, and once the interlocking diminishes, the maximum stress in the blocks diminishes as well (Figure 3-9b). For  $z(x, y) = a_{1,2}xy^2$ , sharper features at the contact faces (high  $\phi L$ ) lead to more interlocking between blocks but also to high contact stresses.

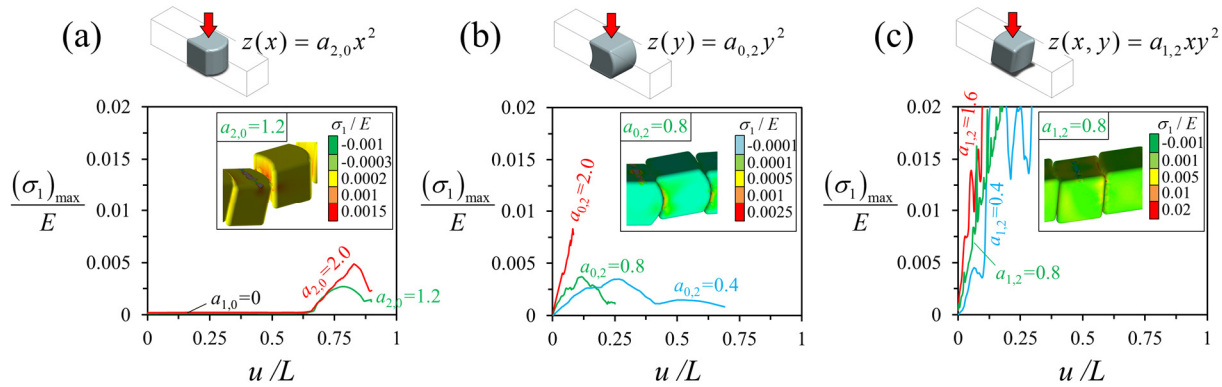


Figure 3-9: Maximum principal stress during deformation for (a)  $z(x) = a_{2,0}x^2$ , (b)  $z(y) = a_{0,2}y^2$  and (c)  $z(x, y) = a_{1,2}xy^2$ . The plots are reported for  $f=0.12$ .

The performance of each design depends not only on interlocking, but also on the strength of the blocks  $\sigma_s / E$ . Like section 2, we truncated the  $F_T-u$  curves at the point at which

$(\sigma_1)_{\max} / E \geq \sigma_s / E$ , and the remaining first part of these curves were used to compute the toughness  $U_{\max}$  and the strength  $F_{\max}$  (Appendix 3.9.2, Figure 3-15). For each design we explored about 25 combinations of different constants (i.e. different amplitudes, Appendix 3.9.3, Figure 3-16b). The maximum strength and toughness were computed for three different strength levels  $\sigma_s / E$ , resulting in a total of 75 simulations for each design. For both monomials and binomials, the optimum design was found by plotting the data on  $F_{\max}-U_{\max}$  space (Appendix 3.9.3, Figure 3-16). Figure 3-10 shows the performance for two examples, the cubic:  $z(y) = a_{0,3}y^3$  and the monkey-saddle:  $z(x, y) = a_{2,1}x^2y + a_{0,3}y^3$ . For each geometry we considered three levels of strength:  $\sigma_s / E = 10^{-4}, 10^{-3}, 10^{-2}$ . The plots include the cube design  $a_{i,j} = 0$  (flat contact faces) for comparison. The higher the  $\sigma_s / E$ , the higher the strength and toughness, because the blocks can withstand more stresses, and therefore they can undergo more interlocking and sliding during deformation. For each value of  $\sigma_s / E$ , there is an optimum design; a particular  $a_{i,j}$  value on  $F_{\max}-U_{\max}$  space that outperforms other designs. For each value of  $\sigma_s / E$ , the shape of the optimum design is shown adjacent to each optimum point along with the optimum  $a_{i,j}$  value(s).

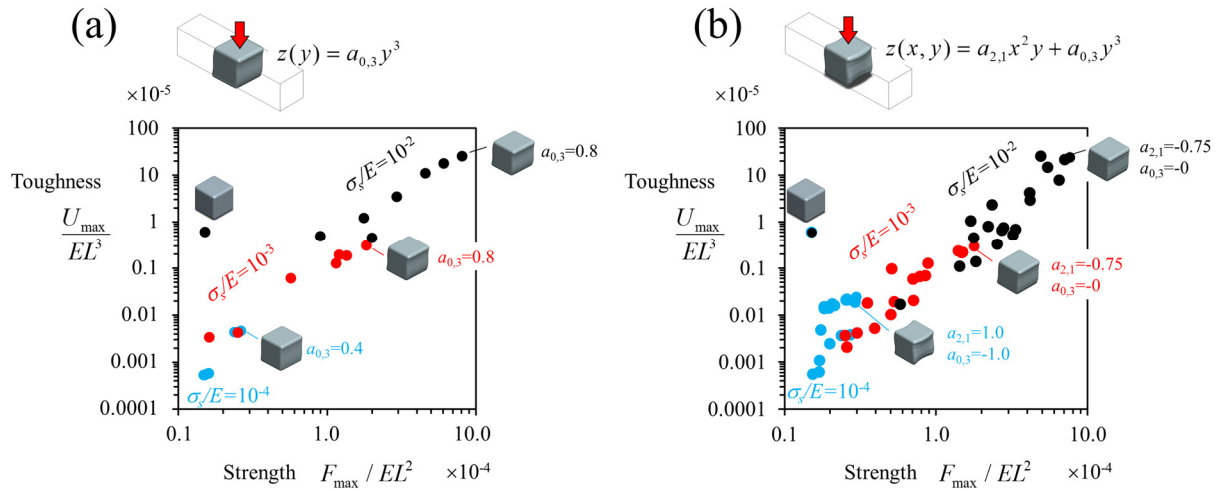


Figure 3-10: Optimization of (a) a monomial:  $z(y) = a_{0,3}y^3$  and (b) a binomial:  $z(x, y) = a_{2,1}x^2y + a_{0,3}y^3$  for  $\sigma_s/E = 10^{-4}, 10^{-3}$  and  $10^{-2}$ . The plots are reported for  $f=0.12$ .

For each geometrical design and strength, we could therefore identify the optimum amplitudes  $a_{i,j}$ . The results are displayed on an Ashby plot for  $\sigma_s / E = 10^{-4}, 10^{-3}, 10^{-2}$ , designated by blue, red and grey respectively (Figure 3-11). For comparison, simulation results for a monolithic beam with the same dimensions, under same mechanical loads, including the same axial precompression ( $F_A / EL^2 = 6 \times 10^{-5}$ ) and made of the same material are also shown (denoted by a “+” marker on each plot). We first note that none of the architected designs exceed the strength of the monolithic beam, but also that many of them exceed the monolithic case in terms of toughness. The designs with best combinations of strength and toughness are highlighted in yellow on Figure 3-11 within each of their strength groups. The distribution of these best designs indicates that there is a compromising relationship between strength and toughness that is more prominent for weak blocks  $\sigma_s / E = 10^{-4}$  (Figure 3-11a). For  $\sigma_s / E = 10^{-4}$  (weak blocks), the cubes (denoted by empty square marker) absorbed 280 times more energy than the monolithic but lost 60% of strength. For best toughness, the monomials that are function of only  $x$  ( $z(x)$ ) absorbed the highest energy. The absence of progressive interlocking in these monomials subjected their contact faces to lower stresses in comparison with the rest. Therefore, they deformed more, through which they absorbed more energy. For the tilted-cubic:  $z(y) = 0.125y - 1.0y^3$  (denoted by triangle with black outline), the blocks interlock along loading direction ( $y$ -direction) which induces mechanical hardening and as a result fail at a higher force than the rest. Because of this interlocking it lost only 16% of strength, achieving the highest strength relative to other designs and managed to improve toughness by 4 times. For slightly stronger blocks:  $\sigma_s / E = 10^{-3}$ , the beam can generally sustain higher stresses, and so wavier and more curved designs are among the best designs (Figure 3-11b). For highest toughness, the hyperbolic-paraboloid:  $z(x, y) = a_{1,1}xy$  (denoted by a filled diamond marker) absorbed the highest energy, about 13 times more than the monolithic. Although, the cube design performed well too, the twisted faces of hyperbolic-paraboloid guide the sliding in a twisting path along  $y$ -direction which jams the blocks and induces progressive interlocking (Appendix 3.9.2, Figure 3-15b). For best strength, we selected two designs; the tilted-cubic denoted by a triangular marker with black outline) and the tilted-parabolic:  $z(y) = 0.156y - 0.625y^2$  (denoted by a circular marker with black outline), both of which approached the strength of the monolithic. The tilted-parabolic contact face is a further enriched

version of the concavo-convex design (indicated by filled circle marker), the additional 0.156y term induced an additional interlocking that improved its performance. Both designs lost only 30% and 4% of strength respectively, moreover, they have absorbed 4 times more energy than that of the monolithic.

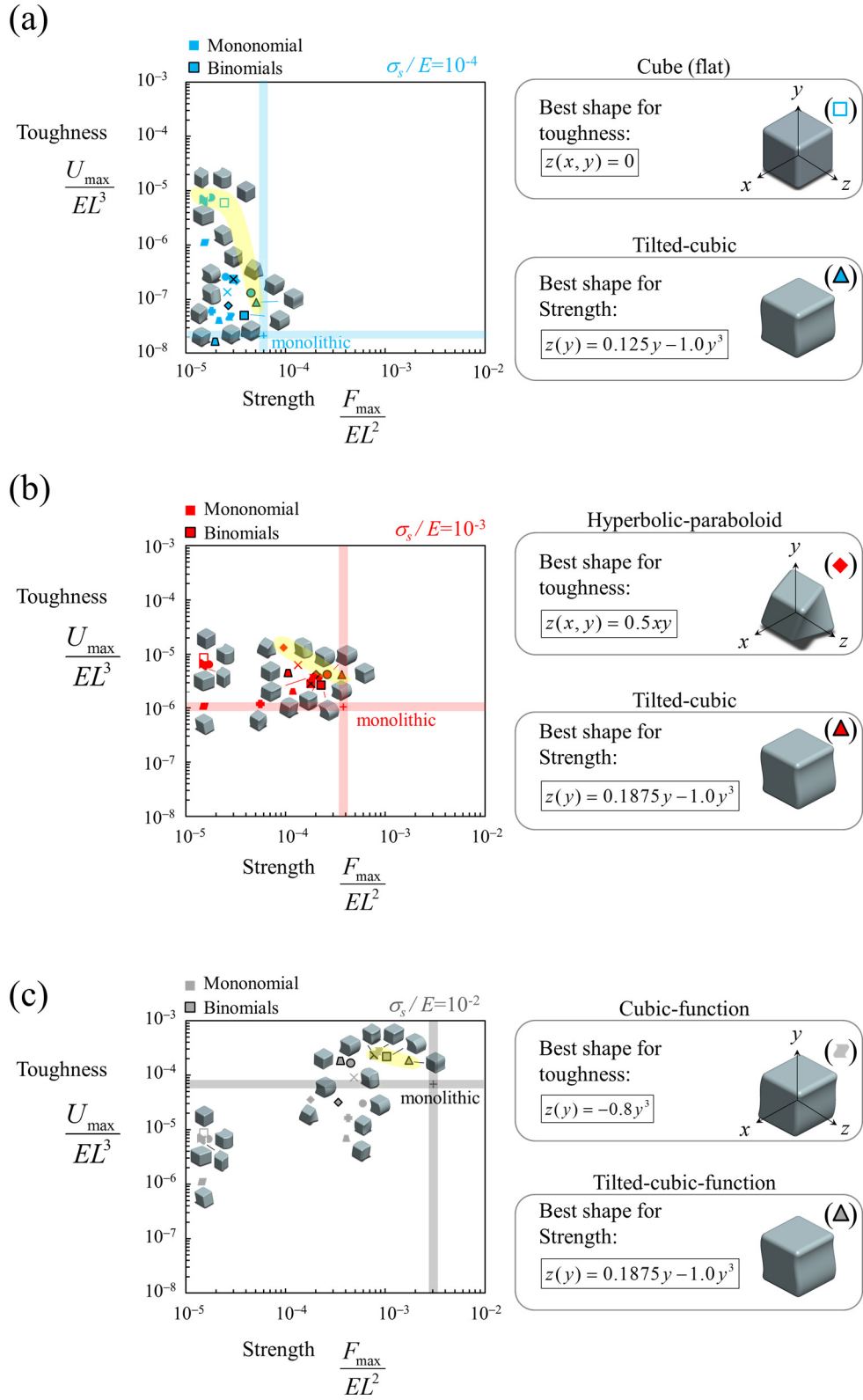


Figure 3-11: Strength and toughness in an Ashby-like plot for (a)  $\sigma_s/E=10^{-4}$  (blue), (b)  $\sigma_s/E=10^{-3}$ (red), and (c)  $\sigma_s/E=10^{-2}$  (grey). The plots are reported for  $f=0.12$ .

For strong blocks:  $\sigma_s / E = 10^{-2}$ , only six designs out of 16 surpassed the toughness of the monolithic beam. For highest toughness, the  $z(x, y) = -0.8y^3$  design (denoted by a curved solid square without outline) absorbed 3.5 more energy than that of the monolithic while losing 75% of strength. The tiled-cubic (denoted by a solid triangle with black outlines) was the strongest design, and absorbed 2.7 times more energy than the monolithic. These curved and wavy designs (highlighted in yellow) have also outperformed the concavo-convex design. Finally for comparison with recent studies in the literature, we added the performance of the osteomorphic blocks (Figure 3-1b) which in previous studies showed promising results [12, 14, 15]. Here however, the osteomorphic geometry (denoted by a cross, “ $\times$ ”) was outperformed by some designs for all values of  $\sigma_s / E$ . Its best performance was achieved for  $\sigma_s / E = 10^{-3}$  (Figure 3-11b), where it absorbed 6 times more energy than the monolithic and lost about 65% of strength.

For weak blocks (low  $\sigma_s / E$ ), toughness relies mainly on stability. As  $\sigma_s / E$  increases, toughness relies progressively more on interlocking (jamming of block). For very strong blocks, the designs reach their full potential by reaching their maximum deformation before fracture, so they mainly fail due to instability. As a result designs that generate the highest interlocking during deformation stand out.

### 3.6 Experimental testing of architected ceramic glass

In this part of the study, we fabricated and tested architected beams made of ceramic glass, a material with several attractive properties including transparency, high strength, low thermal expansion and low cost [1, 3]. The samples were cut from a monolithic ceramic glass beam ( $\sigma_s = 90 \pm 8.2$  MPa,  $E = 100$  GPa, so  $\sigma_s / E \approx 10^{-3}$ ) using a nanosecond pulsed laser (Model Vitrolux, Vitro Laser Solutions UG, Minden, Germany) (Appendix 3.9.4). We fabricated and tested monolithic (Figure 3-12a) and cubes-based (Figure 3-12b) beams as references. Both monolithic and architected samples were tested under same loads. We also fabricated and tested beams with the best three designs we identified for  $\sigma_s / E \approx 10^{-3}$  (Figure 3-11b): the hyperbolic-paraboloid (Figure 3-12c) (best for toughness), the tilted-parabolic (Figure 3-12d) (good for strength) and the tilted-cubic (Figure 3-12e) (best for strength). These architected beams were mounted on two

steel ( $E=200$  GPa) supports and pre-compressed along the axial direction ( $z$ -axis) by a stiff vise. The precompression force  $F_A$  was measured using a low-profile force sensor (FlexiForce®, Tekscan). All experimental tests were conducted for  $F_A=30$  N. The setup was placed under a dual column stage (Admet, model eXpert 5000, MA US), and an indenter with a nozzle head (with radius of 1.5 mm) imposed a displacement  $u$  along the transverse direction at a rate of 10  $\mu\text{m}/\text{sec}$  (Figure 3-17b). The transverse force  $F_T$  was measured using a 150 lbf load cell. Using this setup, we obtained the full  $F_T-u$  curves until complete failure as well as performed in-situ imaging to capture the deformation stages of the architected beam. Figure 3-12 shows the deformation stages of each design with increased displacement  $u$ .

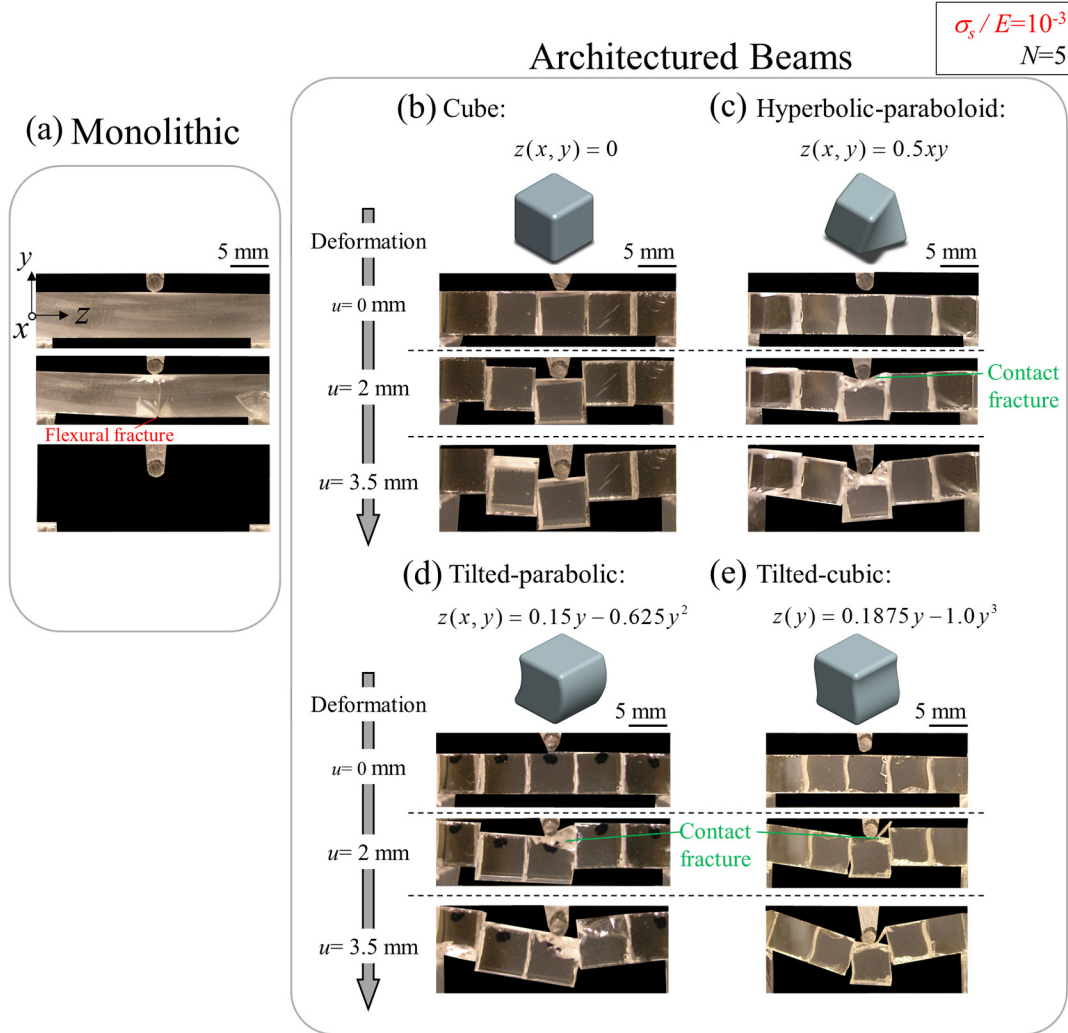


Figure 3-12: Deformations of ceramic glass beams during experiments for (a) monolithic beam and architected beams: (b)  $z(y) = 0$ , (c)  $z(y) = 0.5xy$ , (d)  $z(y) = 0.15y - 0.625y^2$  and (e)  $z(y) = 0.1875y - 1.0y^3$ .

The monolithic sample showed a sudden catastrophic failure from high flexural stresses in the region of the indenter and at the lower face of the beam (indicated on Figure 3-12a). For the case of cubes, the middle block(s) sled gracefully until it was fully pushed out (Figure 3-12b). We did not observe cracks or chip offs during deformation for the cube design because of the low stresses at the contact faces. The hyperbolic-paraboloid design progressively failed. The blocks followed a twisted sliding path which progressively jammed the blocks. In the tilted-parabolic and the tilted-cubic designs the curved contact faces induced strong jamming at the interface, so that groups of several blocks sled as one block [41](Figure 3-12d and e). The high contact stresses, that developed

because of jamming, generated cracks at the interfaces (Figure 3-12c, d and e). However these cracks propagated in a stable fashion with increasing load, and they were confined to individual blocks. Representative  $F_T-u$  curves from these experiments are shown on Figure 3-13a. As expected the monolithic beams showed a rapid linear increase in  $F_T$  that ended with sudden drop that reflects their catastrophic failure. The architected beams showed more jagged increases in forces, but sustained over much larger displacements compared to the monolithic case. This sustained but “noisy” increase in force corresponds to the progressive jamming of the blocks. During sliding the axial compressive force decreases continuously, which tend to decrease the efficacy of the jamming. The competition between geometric hardening and softening from the loss of contact area results in a maximum force, followed by softening until complete failure.

Architected samples sustained multiple force drops during loading, which demonstrates an effective capability of damage tolerance that is absent in monolithic samples. For architected samples, the initial drop(s) in force may not be considered as failure points because the structure can still maintain a progressive increase in load, maintain stability and deformation. Assuming the first drop(s) as failure point(s) overlooks the full potential of the architected sample in terms of strength, toughness and deformability. We therefore need to consider the full  $F_T-u$  curves to assess the full potential of architected samples. Certain applications may impose limits on strain or displacement. In such cases, the corresponding maximum strength and toughness are to be calculated based on these strain/displacement limits. Generally however architected materials achieve toughness through maximizing deformation [11, 41].

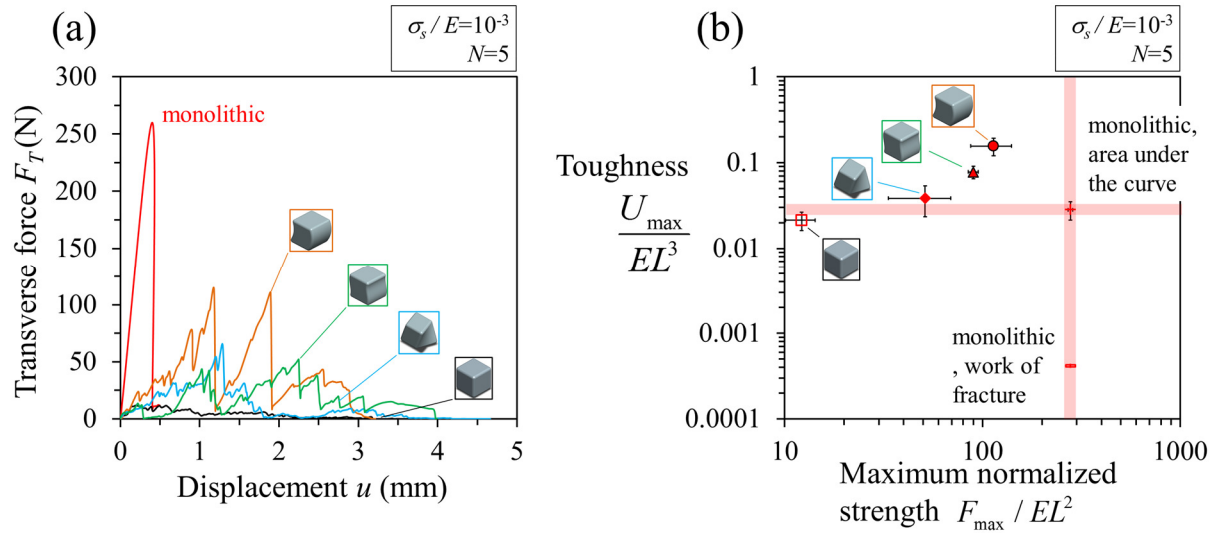


Figure 3-13: Experimental data of monolithic and architected beams. (a)  $F_T-u$  curves and (b) strength and toughness plotted in an Ashby-like chart. For monolithic data, toughness calculated by the total area under the  $F_T-u$  curve is denoted by a cross marker, and by the work of fracture it is denoted by a dash marker.

Using the entire experimental  $F_T-u$  curves we measured strength (maximum force) and toughness (total area under the curve) for each sample ( $N=5$  for each design). For the monolithic beam we added another measure for toughness, where we calculated the work of fracture (denoted by a dash marker, “-”) which is the energy required to grow a crack. If the energy release rate of ceramic glass is  $G=11.13 \text{ J/m}^2$  and the total area of the fracture surface is  $A \approx 1.5L^2$ , the work of fracture becomes  $U=GA=4.17 \times 10^{-4} \text{ J}$ , which is only 2% of the areas under the force-displacement curve [13]. Architected beams are compared with the monolithic using an Ashby like chart for strength and toughness (Figure 3-13b). Tilted-parabolic surpassed the toughness of the monolithic beam by 5.5 times, while preserving 40% of the monolithic strength. Compared to the work of fracture of the monolithic beam, the toughness of the tilted-parabolic was 370 times higher. The tilted-cubic achieved a toughness that is 2.8 times higher, while in terms of work of fracture it is 190 times higher than that of the monolithic and with strength that is 32% of the monolithic strength. The hyperbolic-paraboloid improved toughness by 1.35 times and lost 80% of strength. The flat cubes performed poorly in comparison: Their toughness was lower than the monolithic beam, and they lost 95% of its strength. Comparison of the experimental chart (Figure 3-13b) with corresponding simulations (Figure 3-11b) shows that the relative ranking for the cube (empty square marker),

hyperbolic-paraboloid (diamond marker) and the tilted cubic designs (filled triangle marker with black outline) matches simulations. However, for tilted-parabolic design (filled circle with black outline), experiments show a slightly higher strength and toughness than the tilted-cubic design (filled triangle with black outline) which is inconsistent with the ranking of simulations. This inconsistency is partly because while the FE-models captured the onset of damage, they do not capture post-damage stages (Appendix, 3.9.2, Figure 3-15). In the experiments, some of the designs (including the tilted-parabolic design) showed an increase in force following the onset of damage, which translated into better toughness and strength. FE-simulations therefore provided a conservative measure of relative performance for the architected beams. In addition, the rough contact faces of the blocks contribute to the discrepancy between model-experiments (comparing Figure 3-13b and Figure 3-11b). Damaged interfaces may also have lower effective Young's modulus at the contact between blocks [19], which is not the case in the simulation where we assumed constant elastic modulus for contact. Although simulations in section 8 suggested that the benefit of segmentation in comparison with monolithic beam diminishes with very large values of  $\sigma_s / E$ , experiments showed clearly that despite substantial damage at the surfaces, the structure can still withstand load and exhibit graceful deformation and failure.

### 3.7 Summary

In this study we have used finite element modeling and systematic geometrical enrichments to explore how interlocking and progressive jamming can be used to build strong and tough segmented beams. The simulations revealed that there are optimum shapes for the interfaces between the blocks, and that the optimum geometry depends on the normalized strength  $\sigma_s / E$  for the individual blocks. More specifically, the conclusions for this study are as follows:

1. Architected beams made from simple cubes with flat faces lack hardening because of the absence of jamming and/ or interlocking of blocks. Adding fillets at the corner of the cubes reduced local stresses, but decreased stability. Strength and toughness depended on  $r/L$ ; where optimum  $r/L$  values are  $r/L=0.05$  and  $0.025$  for highest toughness and strength respectively.

2. Interlocking of blocks and jamming can be generated by enriching the contact surface along the direction of loading (i.e. the surface followed the equations of the form  $z(y)$  or  $z(x,y)$ ) Geometric hardening can be tuned by increasing the “waviness” of the interface, but this increase also generated higher contact and frictional stresses.
3. We characterized the geometry of the blocks with a single waviness parameter  $\phi L = \frac{1}{L} \left\langle \frac{\partial^2 z}{\partial y^2} + \frac{\partial^2 z}{\partial y \partial x} \right\rangle \left/ \left\langle \frac{\partial z}{\partial y} + \frac{\partial z}{\partial x} \right\rangle \right.$ . Assuming infinite strength of the blocks, beam strength and toughness correlated well with this waviness parameter.
4. Overall strength and toughness of the architected beams depend on the strength of the individual blocks  $\sigma_s / E$ . Beams made of weak material can only achieve high toughness through deformation and negligible interlocking. Beams made of stronger blocks (higher  $\sigma_s / E$ ) can use more interlocking between blocks to achieve both high strength and toughness.
5. Experiments with ceramic glass beams made from tilted-parabolic:  $z(y) = 0.15y - 0.625y^2$  and tilted-cubic:  $z(y) = 0.1875y - 1.0y^3$  confirmed that these designs lead to graceful sliding and jamming of individual blocks. These designs improved toughness up to 370 times and 190 times respectively while preserving 40% and 32% of the strength of the monolithic beam respectively.

Future work may include investigating the waviness parameter  $\phi L$  in two dimensional architected panels. This study may also provide insights on the mechanics of spines and how vertebrae interact. For synthetic materials we seek ways to increase jamming of blocks to improve strength. However, the opposite is sought to prevent spine injuries, where we seek ways to reduce the stresses. For example, by reducing the amplitude of the articulation between vertebrae (by reducing  $a_{i,j}$ ), reducing the slenderness (by decreasing the number of blocks), reducing the gradients of contact faces (by decreasing  $\phi L$ ) and if geometrical changes are inaccessible, the vertebrae could be reinforced to increase its strength (higher  $\sigma_s / E$ ).

### 3.8 Acknowledgements

This work was supported by a Strategic Grant (STPGP 479137-5) from the Natural Sciences and Engineering Research Council of Canada and by a Team Grant (191270) from the Fonds de Recherche du Québec – Nature et Technologies. A.D. was partially supported by a McGill Engineering Doctoral Award.

### 3.9 Appendix

#### 3.9.1 Details of finite element model

A 3-dimensional (3D) finite element models are prepared to capture the mechanical response of various interface designs. A generic code was written in Matlab to automatically enrich the blocks with different interface geometries. The models are solved in ANSYS where displacements, forces and stresses are obtained and finally post processed using Matlab. The communication between ANSYS and Matlab is automated as a single function, where different combinations of friction  $f$ , different shapes (Figure 3-5 and 3-6) (different polynomial functions, equation (3.1)), different coefficients, precompression  $F_A$  and number of blocks  $N$  can be input and simulated. However, we have limited the study to 5 blocks ( $N=5$ ) because of expensive computational costs with larger  $N$ . The blocks are modeled as continuum with linear elastic model for the material with Young's modulus  $E$  and Poisson's ration  $\nu=0.2$  (typical for ceramics and brittle materials). We meshed the blocks using 20 nodes quadratic 3D element (SOLID186 [42]). The faces of the interfaces are meshed using quadratic contact elements (CONTA 172) which model contact deformations and dry contact friction. The beam rests on rigid supports. These rigid supports are meshed using rigid contact elements (TARGE 169, [43]). The blocks where pressed axially together by an axial force  $F_A$  applied at both ends ( $z=0$  and at  $z=5L$ ) (Figure 3-2). A transverse force  $F_T$  is applied at the center of the beam at ( $x=L/2$ ,  $y=L/2$  and  $z=5L/2$ ). Upon solving the model, we obtain the force displacement curve  $F_T-u$  and the maximum principle stress  $(\sigma_1)_{\max}$ . While tracking  $(\sigma_1)_{\max}$  we excluded the stresses under load  $F_T$  because the stress there approach extremely large values.  $F_T-u$  curves obtained from the FE model are validated against experiments for three cases of amplitude  $A/L=0$  (cube), 0.225, 0.5 (half a circle) for  $z(y)=a_{0,2}y^2$  (Figure 3-14a). In addition, the

deformation is compared with 3D printed blocks (Figure 3-14b). Figure 3-14 shows that FE simulations captured the force and the deformation of the experiments well.

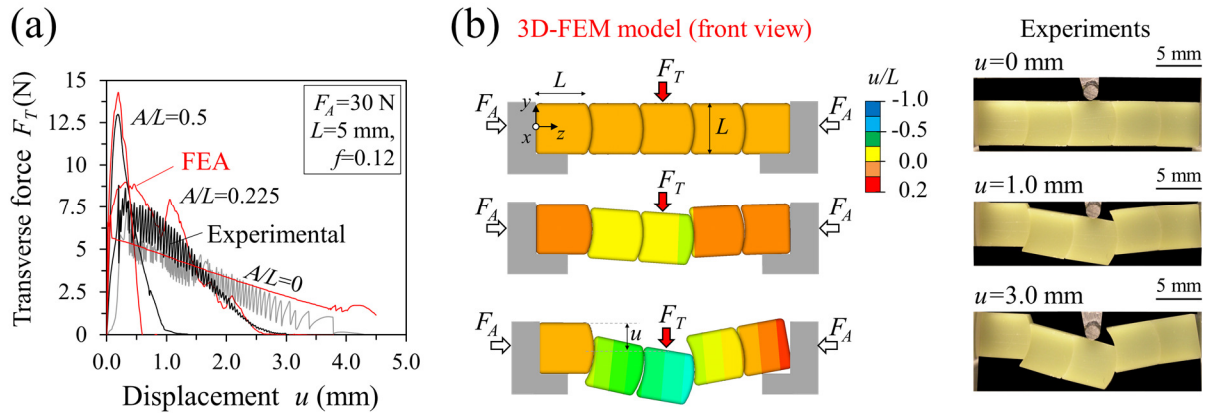


Figure 3-14: Validation of the FE-model; (a) experimental force-displacement (denoted by black line and grey; the grey color is used to allow visualization of  $A/L=0$  case) curves compared with FE-model (denoted by a red line), (b) shows the deformation of architected beam with blocks having contact faces described by  $z(y) = a_{0,2}y^2$ , the deformed contour plots are compared side by side with experimental snapshots of the same design.

### 3.9.2 Calculating the strength and toughness

The maximum principal stress  $(\sigma_1)_{\max}$  is tracked for the entirety of the simulation until complete failure of the system. Figure 3-15a shows the normalized stress plotted with deformation  $u$  for the hyperbolic-paraboloid:  $z(x, y) = a_{1,1}xy$ . Figure 3-15a shows how the displacement at a critical stress level is found. For example, here we consider the stress limit as  $\sigma_s / E = 10^{-3}$  which limits the displacement at  $u/L=0.2$  which is the displacement at fracture. Figure 3-15b shows the principal stress  $\sigma_1(x, y, z)$  contours at that fracture displacement ( $u/L=0.2$ ). Figure 3-15b also shows a zoomed image focused at the location of critical maximum stress  $(\sigma_1)_{\max}$ . The displacement at which  $(\sigma_1)_{\max} / E > \sigma_s / E$  can then be used to truncate the force displacement curve to depict the failure of the structure (Figure 3-15c). Once the curve is truncated, we can calculate the area under the curve and the maximum force to estimate the toughness and strength respectively (Figure 3-15d).

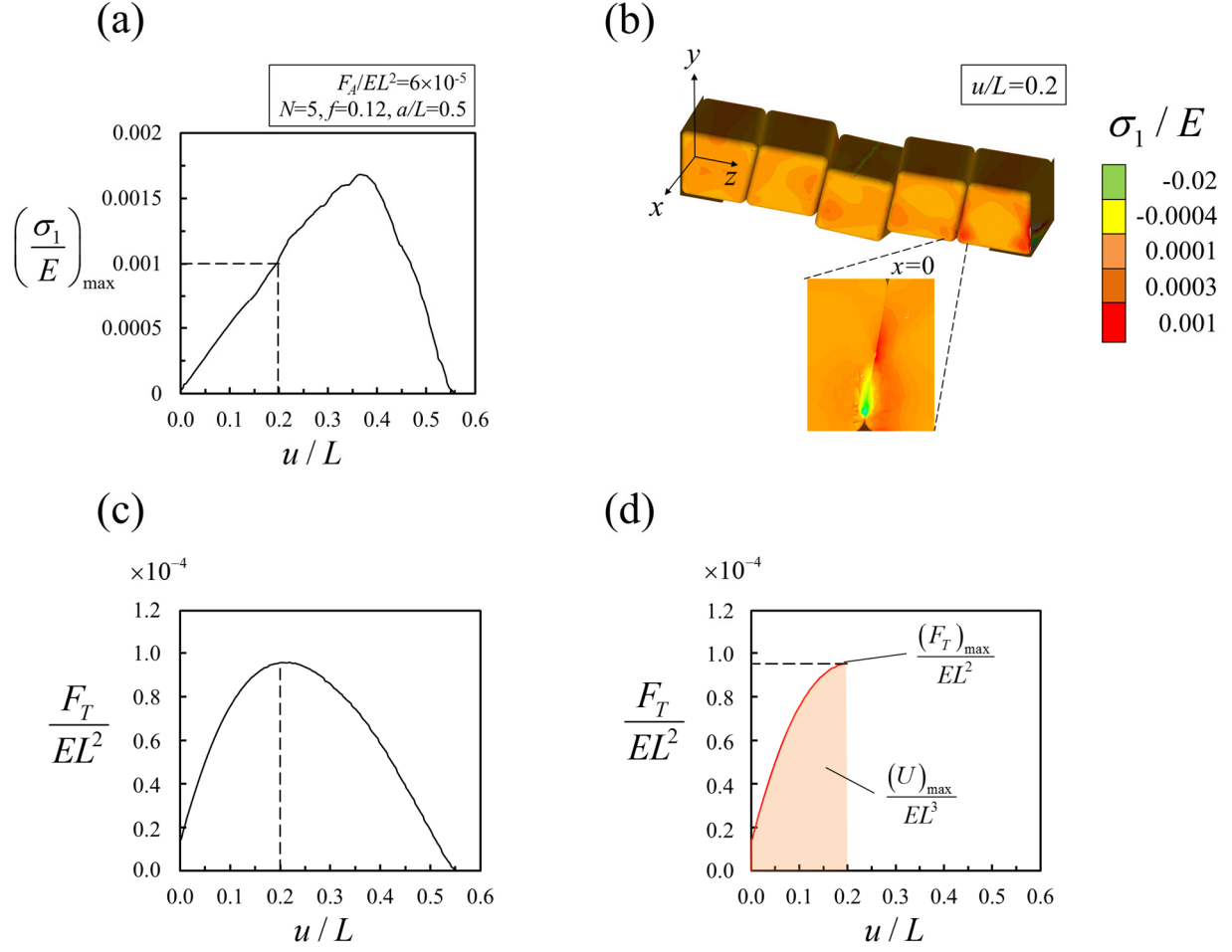


Figure 3-15: Procedure for calculating the maximum strength and toughness based on the limits of the strength of blocks  $\sigma_s / E$ , (a) maximum principal stress  $(\sigma_1)_{\max}$  variation with displacement; displacement at the point of fracture can be found, here for example, displacement at fracture is  $u/L=0.2$  for  $\sigma_s / E = 10^{-3}$ ; (b) contour plot of  $(\sigma_1)_{\max}$  at the point of fracture; (c) force–displacement truncated,  $F_T-u$ ; (d)  $F_T-u$  truncated at the point of fracture, therefore toughness  $U_{\max}$  and strength  $F_{\max}$  are found.

### 3.9.3 Optimization of monomials and binomials

We used the procedure in Appendix 3.9.2 to compute maximum strength  $F_{\max}$  and toughness  $U_{\max}$  for all designs shown on Figure 3-5 and 3-6. Here we conducted a brute force optimization where we explore the design space by computing  $F_{\max}$  and  $U_{\max}$  for  $\sigma_s / E = 10^{-4}, 10^{-3}, 10^{-2}$  for different values of  $a_{i,j}$  such that the amplitude is  $A/L < 0.5$ . For binomials, we explore the design space for different possible combinations of  $a_{i,j}$ . For example, for the monkey-saddle:

$z(x, y) = a_{2,1}x^2y + a_{0,3}y^3$ , combinations of  $(a_{2,1}, a_{0,3})$  is simulated for the range of  $[0,1]$  and  $[-1,1]$  with increment of 0.25, which results in 25 simulations for each  $\sigma_s / E$  value and a total of 75 simulations for each design.  $a_{2,1}$  starts from 0 because the design space within the range of  $[-1,0]$  and  $[-1,1]$  for  $a_{2,1}$  and  $a_{0,3}$  respectively is identical to the  $[0,1]$  and  $[-1,1]$ , so part of the design space bound by  $a_{2,1}$  with  $[-1,0]$  is redundant. As an example, Figure 3-16 shows  $F_{\max}$  and  $U_{\max}$  for different  $a_{i,j}$  values for  $z(y) = a_{0,3}y^3$  and  $z(x, y) = a_{2,1}x^2y + a_{0,3}y^3$ .

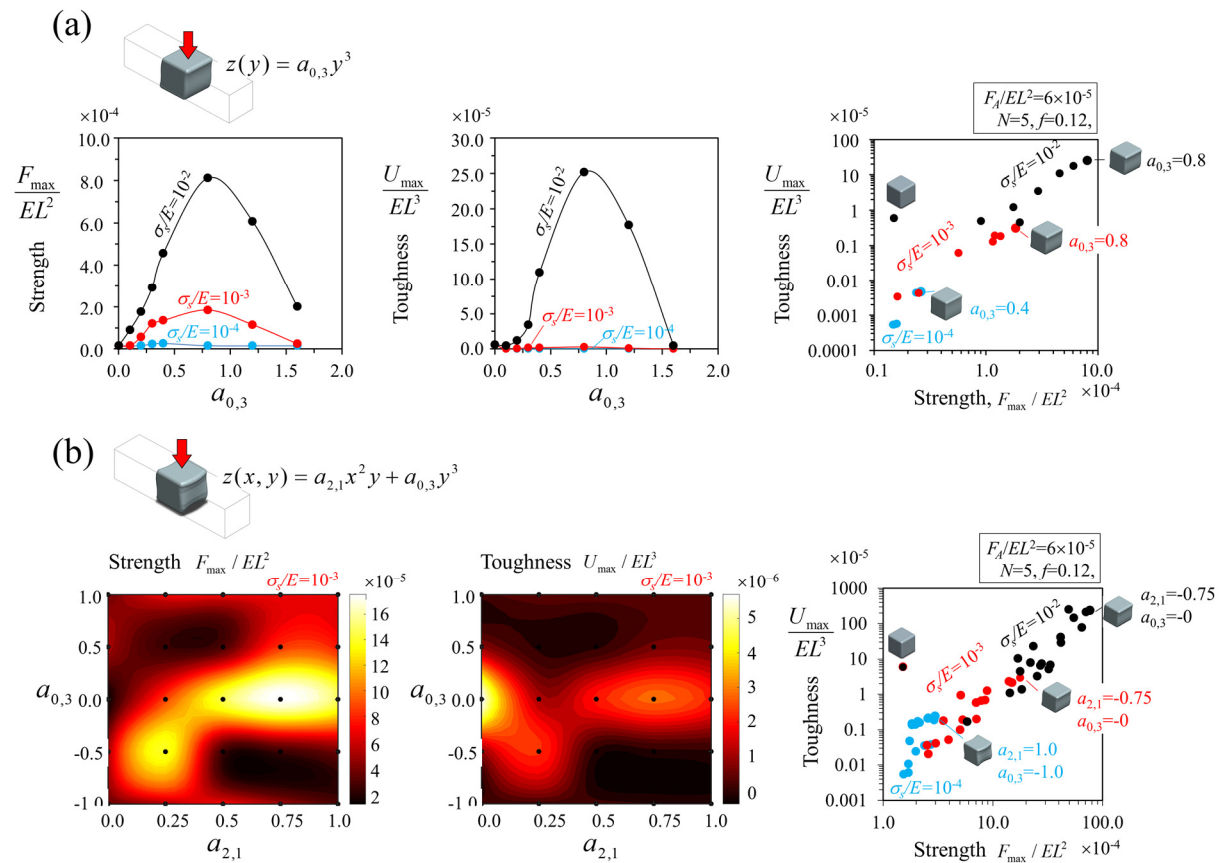


Figure 3-16: Brute force optimization for the coefficients  $a_{i,j}$  such that the  $A/L \leq 0.5$  for (a) a monomial:  $z(y) = a_{0,3}y^3$  and (b) a binomial:  $z(x, y) = a_{2,1}x^2y + a_{0,3}y^3$ .

Figure 3-16a shows that  $F_{\max}$  and  $U_{\max}$  increases as  $a_{0,3}$  increases because of increased geometric hardening resulting from larger  $a_{0,3}$ . However, there is a peak point after which both  $F_{\max}$  and  $U_{\max}$  start to decrease. Figure 3-16b shows  $F_{\max}$  and  $U_{\max}$  as contours for  $\sigma_s = 10^{-3}$  because the

simulation is run for 2 design variables:  $a_{2,1}$  and  $a_{0,3}$ . Strength is maximum at  $(a_{2,1} = 0.75, a_{0,3} = 0)$ , for this particular design any contribution from  $a_{0,3}$  term induces severe interlocking between blocks which results in very high stresses. These high stresses exceed  $\sigma_s / E$  of the beam therefore the maximum force reached during deformation is lower than cases of  $a_{0,3} = 0$ . Whereas, toughness is maximum at  $(a_{2,1} = 0, a_{0,3} = 0)$  which represents the cubes case. The cubes contact faces are flat, so the stresses are much lower than wavy and curved faces, therefore it can deform for larger displacement without failure. Both Figure 3-16a and b show how peak points for  $F_{\max}$  and  $U_{\max}$  may not necessary match, because there is a compromise between strength and toughness where both can have their distinct optimum  $a_{i,j}$  values. The objective is to find the optimum design for both strength and toughness. To do so we plot simulation results on  $F_{\max} - U_{\max}$  space. If the strength and toughness of a particular design is greater than the rest, this design is therefore is nondominated and it is considered as an optimum design. Optimum designs is shown adjacent to their corresponding optimum points.

#### 3.9.4 Preparing the ceramic glass samples

A 50 mm  $\times$  50 mm  $\times$  5 mm ceramic glass plate is cut into several prismatic beams with a span of 25 mm and depth of 5 mm (Figure 3-17a). These beams are cut into unit blocks using a nanosecond laser (Model Vitrolux, Vitro Laser Solutions UG, Minden, Germany) equipped with a pulsed UV laser (355 nm, 0.5 W cw pumped, 4 kHz repetition rate, 4–5 ns pulse duration). Different shapes were input as a cloud of points described by equation (3.1). The laser therefore traces different geometries and so carves the desired shapes of blocks from the prismatic beams (Figure 3-17b). The blocks are then assembled into an architected beam and mounted on steel rigid supports ( $E=250$  GPa) (Figure 3-17b). The blocks are pressed by a vise from both ends. A low-profile pressure sensor tracks and measures the axial force before and during testing. A dual-column loading stage (Admet, model eXpert 5000, MA US) is used to apply a displacement control load along the transverse direction ( $y$ -axis) by an indenter with a round nozzle head of a radius  $R=1.5$  mm. The displacement is imposed at a rate of 10  $\mu\text{m}/\text{sec}$  at the center of the beam (half way along the span) until complete failure. The transverse force  $F_T$  was measured using a 150 lbf load cell.

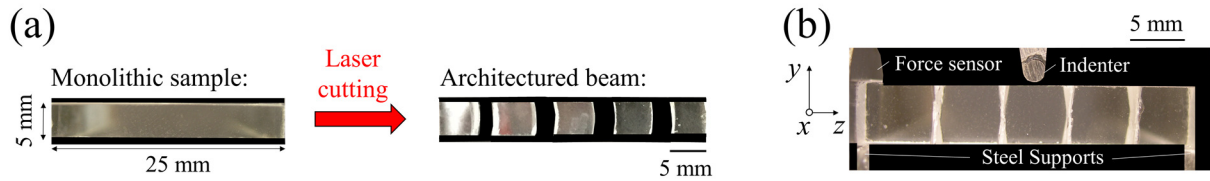


Figure 3-17: Experimental testing and fabrication of architected ceramic glass beams. (a) monolithic beam is laser cut into blocks; (b) experimental setup.

### 3.10 References

1. Ashby, M.F., *Materials Selection in Mechanical Design*. 5 ed. 2016, Cambridge, MA: Butterworth-Heinemann. 664.
2. Wondraczek, L., et al., *Towards Ultrastrong Glasses*. *Advanced Materials*, 2011. **23**(39): p. 4578-4586.
3. Wachtman, J.B., W.R. Cannon, and M.J. Matthewson, *Mechanical Properties of Ceramics*. 2009: John Wiley & Sons. 498.
4. Klingner, R.E., *Masonry Structural Design*. 2010, New York, USA, UNITED STATES: McGraw-Hill Professional Publishing.
5. Schultz, A. and M. J Scolforo, *An Overview of Prestressed Masonry*. *TMS Journal*, 1991. **10**: p. 6-21.
6. Sharp, K.G. and P.J. Armstrong, *Interlocked Concrete Block Pavements*. Australian Road Research Board Special Report, 1985(31).
7. Dyskin, A.V., et al., *Toughening by Fragmentation—How Topology Helps*. *Advanced Engineering Materials*, 2001. **3**(11): p. 885-888.
8. Dyskin, A.V., et al., *Topological interlocking of platonic solids: A way to new materials and structures*. *Philosophical Magazine Letters*, 2003. **83**(3): p. 197-203.
9. Siegmund, T., et al., *Manufacture and Mechanics of Topologically Interlocked Material Assemblies*. *Applied Mechanics Reviews*, 2016. **68**(4): p. 040803-040803.
10. Mirkhalaf, M., et al., *Toughness by segmentation: Fabrication, testing and micromechanics of architected ceramic panels for impact applications*. *International Journal of Solids and Structures*, 2018.
11. Mirkhalaf, M., T. Zhou, and F. Barthelat, *Simultaneous improvements of strength and toughness in topologically interlocked ceramics*. *Proceedings of the National Academy of Sciences*, 2018. **115**(37): p. 9128-9133.
12. Rezaee Javan, A., et al., *Impact behaviour of plate-like assemblies made of new and existing interlocking bricks: A comparative study*. *International Journal of Impact Engineering*, 2018. **116**: p. 79-93.
13. Camacho, G.T. and M. Ortiz, *Computational modelling of impact damage in brittle materials*. *International Journal of Solids and Structures*, 1996. **33**(20): p. 2899-2938.
14. Dyskin, A.V., et al., *The principle of topological interlocking in extraterrestrial construction*. *Acta Astronautica*, 2005. **57**(1): p. 10-21.
15. Dyskin, A.v., et al., *Fracture Resistant Structures Based on Topological Interlocking with Non-planar Contacts*. *Advanced Engineering Materials*, 2003. **5**(3): p. 116-119.

16. Ming-Yuan, H. and J.W. Hutchinson, *Crack deflection at an interface between dissimilar elastic materials*. International Journal of Solids and Structures, 1989. **25**(9): p. 1053-1067.
17. Barthelat, F., *Architected materials in engineering and biology: fabrication, structure, mechanics and performance*. International Materials Reviews, 2015. **60**(8): p. 413-430.
18. Mirkhalaf, M., A.K. Dastjerdi, and F. Barthelat, *Overcoming the brittleness of glass through bio-inspiration and micro-architecture*. Nature Communications, 2014. **5**.
19. Kemeny, J. and N.G.W. Cook, *Effective moduli, non-linear deformation and strength of a cracked elastic solid*. International Journal of Rock Mechanics and Mining Sciences & Geomechanics Abstracts, 1986. **23**(2): p. 107-118.
20. Malik, I.A. and F. Barthelat, *Toughening of thin ceramic plates using bioinspired surface patterns*. International Journal of Solids and Structures, 2016. **97-98**: p. 389-399.
21. Khandelwal, S., et al., *Transverse loading of cellular topologically interlocked materials*. International Journal of Solids and Structures, 2012. **49**(18): p. 2394-2403.
22. Grimaldi, G., A. Papangelo, and M. Ciavarella, *A Cattaneo-Mindlin problem for a rigid punch with tangential load applied above the interface line*. Proceedings of the Institution of Mechanical Engineers, Part C: Journal of Mechanical Engineering Science, 2016. **230**(9): p. 1410-1416.
23. Johnson, K.L., *Contact Mechanics*. 1987: Cambridge University Press. 472.
24. Blau, P.J., *Friction Science and Technology*. 1995: CRC Press. 422.
25. Estrin, Y., et al., *Architected Materials in Nature and Engineering: Archimats*. Springer Series in Materials Science. 2019: Springer International Publishing.
26. Barthelat, F., *Biomimetics for next generation materials*. Philosophical Transactions of the Royal Society of London A: Mathematical, Physical and Engineering Sciences, 2007. **365**(1861): p. 2907-2919.
27. Liu, Z., et al., *Functional gradients and heterogeneities in biological materials: Design principles, functions, and bioinspired applications*. Progress in Materials Science, 2017. **88**: p. 467-498.
28. Alben, S., P.G. Madden, and G.V. Lauder, *The mechanics of active fin-shape control in ray-finned fishes*. Journal of the Royal Society Interface, 2007. **4**(13): p. 243-256.
29. Porter, M.E., R.H. Ewoldt, and J.H. Long, *Automatic control: the vertebral column of dogfish sharks behaves as a continuously variable transmission with smoothly shifting functions*. The Journal of Experimental Biology, 2016. **219**(Pt 18): p. 2908-2919.
30. Dunn, I.F., M.R. Proctor, and A.L. Day, *Lumbar spine injuries in athletes*. Neurosurgical Focus, 2006. **21**(4): p. E4.
31. Oxland, T.R., *Fundamental biomechanics of the spine—What we have learned in the past 25 years and future directions*. Journal of Biomechanics, 2016. **49**(6): p. 817-832.
32. Fratzl, P., et al., *The mechanics of tessellations - bioinspired strategies for fracture resistance*. Chemical Society Reviews, 2016. **45**(2): p. 252-267.
33. Clement, N. and R. Schlader. *Orcinus Orca*. 2012 2019/03/29/00:49:11; Available from: <https://ptmsc.org/boneatlas/>.
34. Wright, J.K., *Ammonites*. Geology Today, 2012. **28**(5): p. 186-191.
35. John, J.S., *Tornoceras uniangulare aldenense fossil goniatite (Alden Pyrite Bed, Ludlowville Formation, Middle Devonian; western New York State, USA) I*. 2014.
36. Fronimos, J.A., J.A. Wilson, and T.K. Baumiller, *Polarity of concavo-convex intervertebral joints in the necks and tails of sauropod dinosaurs*. Paleobiology, 2016. **42**(4): p. 624-642.

37. Troxell, E.L., *Mechanics of Crocodile Vertebrae*. GSA Bulletin, 1925. **36**(4): p. 605-614.
38. Molnar, J.L., et al., *Morphological and functional changes in the vertebral column with increasing aquatic adaptation in crocodylomorphs*. Open Science, 2015. **2**(11): p. 150439.
39. Dalaq, A.S. and F. Barthelat, *Three-Dimensional Laser Engraving for Fabrication of Tough Glass-Based Bioinspired Materials*. JOM, 2020.
40. Mirkhalaf, M., J. Tanguay, and F. Barthelat, *Carving 3D architectures within glass: Exploring new strategies to transform the mechanics and performance of materials*. Extreme Mechanics Letters, 2016. **7**: p. 104-113.
41. Dalaq, A.S. and F. Barthelat, *Strength and stability in architected spine-like segmented structures*. International Journal of Solids and Structures, 2019. **171**: p. 146-157.
42. Géraudie, J., et al., *Teratogenic and morphogenetic effects of retinoic acid on the regenerating pectoral fin in zebrafish*. Journal of Experimental Zoology, 1994. **269**(1): p. 12-22.
43. Stewart, J., *Calculus*. 2011: Cengage Learning. 1382.
44. ANSYS, *ANSYS Mechanical APDL Modeling and Meshing Guide*. 2013, ANSYS, Release 15.0.
45. ANSYS, *ANSYS Mechanical APDL Contact Technology Guide*. 2013, ANSYS, Release 15.0.

## Link between chapter 3 and chapter 4

In the previous chapter, it was shown that the shape of individual blocks in segmented systems can have a strong effect on overall strength, toughness and failure mode. In addition, experiments in chapter 3 showed how the interfaces between blocks were effective in pinning crack growth and localizing damage within few blocks. In the next chapter, the analysis to glass is extend. The blocks in previous chapter were completely cut, in other words the fracture toughness of the interfaces is zero. The focus was on the effect of the fracture toughness of interfaces on the overall behavior of glass panels. A 3D pulsating laser engraver was used to architect glass panels. As part of this study, the use of confocal microscopy is explored to assess and find the critical laser engraving parameters that controls the morphology of the engraved interfaces, and to examine how the interface morphology in turn impacts the toughness of the interface.

---

## Chapter 4

# Three-Dimensional Laser Engraving for Fabrication of Tough Glass-Based Bioinspired Materials.

---

# Chapter 4: Three-Dimensional Laser Engraving for Fabrication of Tough Glass-Based Bioinspired Materials

Ahmed S. Dalaq<sup>1</sup>, Francois Barthelat\*<sup>1,2</sup>

1: Department of Mechanical Engineering, McGill University, 817 Sherbrooke Street West,  
Montreal, QC H3A 2K6, Canada

2: Department of Mechanical Engineering, University of Colorado, 427 UCB, 1111 Engineering  
Dr, Boulder, CO 80309, United States

\*Corresponding author: francois.barthelat@colorado.edu

## 4.1 Abstract

Glass has many attractive properties including transparency, durability, low electrical conductivity and corrosion resistance, but its brittleness still limits the range of its applications. Here we explore three-dimensional laser engraving to generate 3D networks of weak interfaces within the bulk of glass. These interfaces deflect cracks and dissipate energy by friction, with mechanisms that are similar to fracture in mollusk shells or teeth. Using confocal microscopy we characterized the morphology of laser-induced microcracks in borosilicate glass and ceramic glass, and we measured the effective toughness of laser engraved interfaces. We explored the effect of microcrack spacing on interface morphology, damage parameter, fracture surface and fracture toughness. We then fabricated architected borosilicate glass panels based on a simple grid pattern. These all-brittle panels do not require mechanical confinement, and they absorbed significantly more impact energy than monolithic glass provided that the interface toughness is tuned properly.

*Keywords:* Architected materials, segmented materials, topologically interlocking materials (TIMs), Glass, nondestructive testing.

## 4.2 Introduction

Glass is a relatively hard and stiff material with excellent optical properties, low thermal expansion, low electrical conductivity, chemical resistance, corrosion resistance and durability [1-3]. These properties make glass attractive for manufacturing mirrors, glass wares, windows, windshields or glass facades. However the strength of glass is very sensitive to defects, and fracture in glass is brittle and catastrophic. Several methods have been developed to improve the mechanical properties of glass. Thermal or chemical tempering increase the strength of glass, but not its toughness [1, 4]. Laminating glass improve its damage tolerance, but impact resistance and toughness are not improved significantly [5]. The inherent brittleness of glass can be addressed by incorporating microarchitectures within the bulk of these materials, using heterogeneities compositions, weak interfaces and controlled geometrical features [6-8]. For example, adding ductile particles in glass can hinder crack growth by pinning and crack bridging [9, 10], which improved toughness by 60 times. However, residual stresses and debonding between the metal and glass phases limit the efficacy of this method. Recently, other approaches based on manipulating larger scale features have emerged: architected materials are a powerful approach to producing multifunctional materials that combine tunable strength, toughness and some attractive thermal and electrical properties [6, 11-13]. Architected materials may come in different arrangements such as sandwiched, lattices and segmented forms. Sandwiched structures are well suited for lightweight flexural applications (plates and beams), while lattices are effective for shock absorption [14, 15]. Segmented materials are another type of architected materials which can confine damage, deflect cracks and increase toughness [8, 16, 17]. Interestingly these toughening strategies are also found in hard biological materials such as bone, teeth or mollusk shells [11, 12, 18, 19]. These materials are segmented into smaller building blocks made of hard minerals, bonded by softer organic-rich interfaces. For example, in mollusk shell nacre, the minerals come in the form of microscopic tablets bonded with soft organic layer to form a three-dimensional brick wall (Figure 4-1a). The interplay of architecture and interface properties generate powerful inelastic mechanisms that make nacre three orders of magnitude tougher than its brittle constituents [20-22]. Nacre has therefore been serving as a model and inspiration for designing tougher materials built from brittle components (ceramics, glasses) [20, 23-26] (Figure 4-1b). Many other materials in nature display segmentation: fish fins [27, 28], spines [12, 29] tesserae in sharks skeletons [19]. These periodic arrangements of hard structural elements are reminiscent of masonry, where

building blocks of well-defined geometries are assembled to form self-standing lintels, domes, overhanging components or interlocked pavements. Masonry structures have indeed recently inspired topologically interlocked materials (TIMs) [30-33], a class of materials made of separated blocks that can interact by sliding and interlocking upon loading, resulting in tougher materials. The shape of the blocks and the properties of the interfaces (friction, adhesion, energy dissipation) can be tuned to achieve different combinations of stiffness, strength and toughness [12, 16, 34]. In particular, architecture can be used to generate non-linear and large deformation at the interfaces, turning brittle monolithic materials into deformable structures (Figure 4-1c).

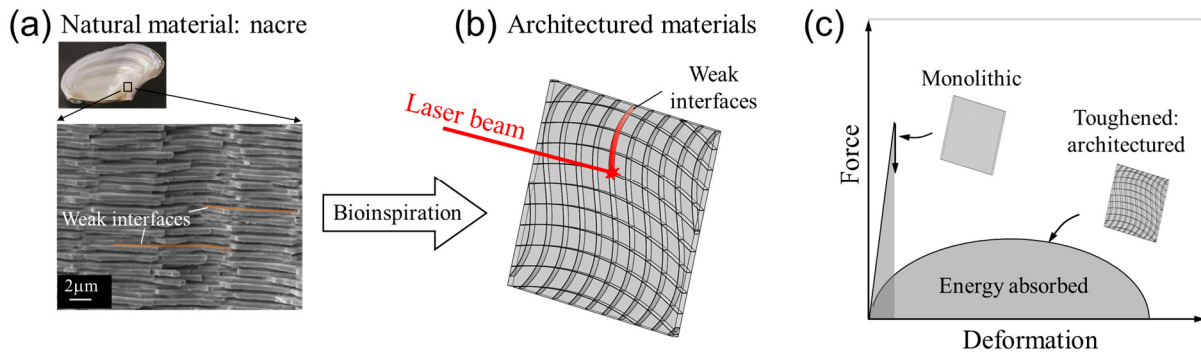


Figure 4-1: (a) Nacre is a hard biological material where the interplay between micro-architecture and weak interfaces generate unique mechanisms and high toughness (adapted from [35] and [22]); (b) these concepts are inspiring new architected materials; (c) Ideal force-deformation curves for monolithic and architected material.

The concepts of bioinspiration, micro-architecture and topological interlocking have recently been implemented in transparent glass. In particular, we recently demonstrated that 3D laser engraving can be used to make glass-based TIM panels [36] cross-ply glasses [37] or nacre-like glasses [25]. These architected glasses showed unusual deformation mechanisms and very high toughness and impact resistance with the addition of polymeric transparent layers. 3D laser engraving is a promising method to “carve” micro-architectures within glass [38], but the micro and meso-structures of the laser engraved interfaces are not well understood. In addition, most recent architected materials have either used completely separated blocks (e.g. TIMs [36]), or utilized the toughening mechanisms of ductile constituents, as in the addition of polymers in the nacre-like glass [25, 37]. Here we mainly consider the toughness of engraved interfaces in glass and their

toughening effects without including ductile materials, so the analysis is based on all-brittle materials. In this chapter we characterize the microscopic and mesoscopic structure of interfaces carved within the bulk of borosilicate glass and ceramic glass. We then expand on existing glass-based engraved material and we present new designs which are based on all-brittle materials, which can operate in free-standing conditions (i.e. no external mechanical confinements from a frame or ligaments are needed).

### 4.3 Laser-engraved interfaces: Fabrications and 3D morphology

A fundamental element of architected glass is the creation of weaker interfaces which can deflect and channel propagating cracks. Here we use a three-dimensional laser engraver (Model Vitrolux, Vitro Laser Solutions UG, Minden, Germany) to carve these weak interfaces. The engraver uses a nanosecond laser that emits a 355 nm UV pulse at frequency of 4-5 ns (0.5 W cw pumped, 4 kHz repetition rate) which is focused at specific points within the bulk of glass. Nanosecond lasers generally form a plasma within nanoseconds at the focal point. This plasma quickly decays by releasing thermal energy into the material [39-43], which creates a rapid and localized increase in local temperature. The resulting high thermal stresses create microcracks within the volume of glass, at discrete points within the volume of glass where the laser beam is focused. We chose to engrave on borosilicate and ceramic glass, because they have low density, low thermal expansion and low refractive index [1]. Their applications are diverse spanning from cookware, electronics, laboratory glass ware, dental cartridges, telescopes, glass facades, to radar protection units of aircraft nosecones [44, 45]. Figure 4-2a shows a planar interface in the  $x$ - $z$  plane that contains a square array of laser engraved microcracks with spacing  $s$ , engraved with a laser beam parallel to the  $x$ -axis. In all of the experiments in this chapter we engraved interfaces with different microcrack spacing  $s = 100, 50, 20, 5, 2$  and  $1 \mu\text{m}$ , the power of the laser was fixed at 400 mJ, which was adequate to generate microcracks in the materials considered here. Increasing laser power increases the size of the microcracks, as reported in [46]. The size of the defects is also governed by the coefficient of thermal expansion (CTE) for the material, since most of the micro-damage is generated by localized thermal stresses [38].

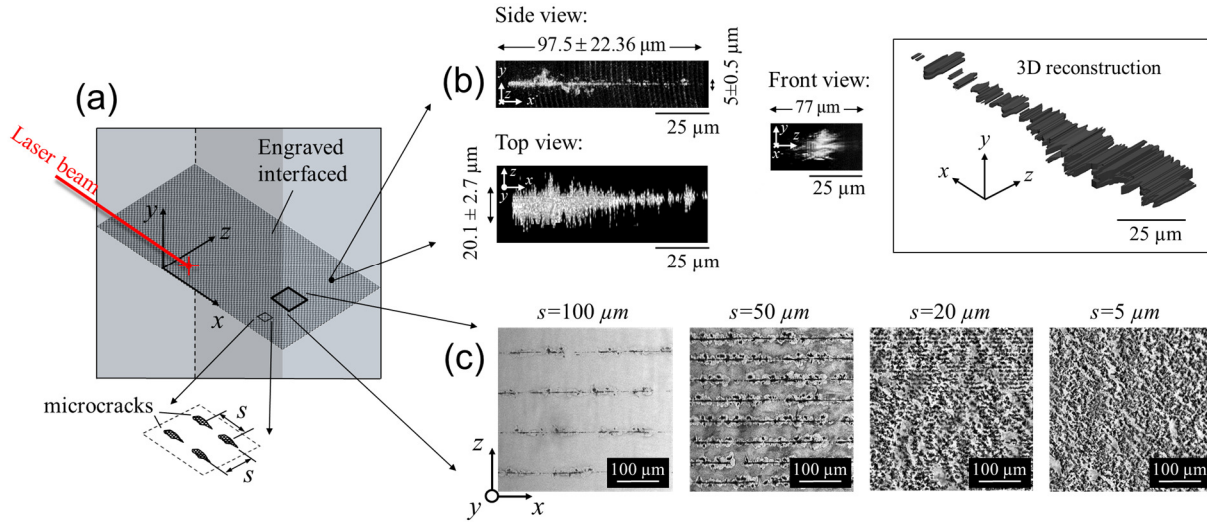


Figure 4-2: (a) Schematic of the engraved interface showing orientations, laser beam direction and microcrack spacing; (b) Confocal microscope images of an individual microcrack generated in borosilicate with a focused laser pulse; (c) Confocal images of engraved interface showing the microcracks distribution for  $s=100, 50, 20,$  and  $5 \mu\text{m}$ .

We used an optical confocal microscope (Leica SP8, Germany) to characterize the three-dimensional morphology of individual microcracks in the material. Figure 4-2b shows the front, side and top view of a typical microcrack in borosilicate glass, together with its 3D reconstruction. The largest dimension of the microcrack is about  $100 \mu\text{m}$  that is aligned with the  $x$ -direction (the direction of incident laser beam) which is possibly due to spherical aberration in the laser focusing lens, and/or due to Rayleigh scattering [47] (Figure 4-2b). The microcrack is narrower along the other two directions, about  $5 \mu\text{m}$  and  $20 \mu\text{m}$  along the  $y$  and  $z$  directions respectively. Because of the local microdamage induced by the nanosecond laser, the outline of the microcracks is rough and irregular. It is also useful to assess how microcracks interact within the engraved interfaces. Figure 4-2c shows arrays of microcracks for spacing  $s = 100, 50, 20$  and  $5 \mu\text{m}$ . The size of the microcrack along the  $x$  direction is larger than the spacing between the microcracks, and therefore they coalesced along that direction. The confocal images indeed show that the coalescence of the microcracks formed parallel lines along the  $x$  direction for  $s=100 \mu\text{m}$  and  $50 \mu\text{m}$ . For  $s=20 \mu\text{m}$ , the spacing was small enough for the microcracks to also coalesce along the  $z$ -direction. For  $s=5 \mu\text{m}$ , all microcracks coalesced so that the damaged areas were more diffused and randomly distributed.

#### 4.4 An image-based damage parameter

Using the confocal images (Figure 4-2c) we assessed the degree of damage at the interfaces for different microcrack spacing  $s$ . The raw confocal images were converted into binary images (black and white) using an image thresholding method. All images were first subjected to a bandpass Fourier transform filter, by which small features and speckles were removed. The images were then converted to binary using Phansalkar local thresholding method [48] (Appendix 4.10.1). This thresholding method is robust and produced clear and consistent outline of microcracks especially for images containing particle-like features. In the resulting images black areas indicate fractured regions of the interface, while white areas indicate intact connected glass (ligaments, Figure 4-3a). From these images we computed a damage parameter:

$$\phi = \frac{A_c}{A} = 1 - \frac{A_l}{A} \quad (4.1)$$

where  $A$  is the total area of image,  $A_c$  is the total black area which represents the cracked portion of the interfaces and  $A_l$  is the total area of the white portion which represents the ligaments. Higher values of  $\phi$  therefore indicate higher levels of interface damage and weaker interfaces. Figure 4-3b shows how the damage parameter  $\phi$  evolves when  $s$  is decreased for both types of glasses. Large spacing (100  $\mu\text{m}$ ) barely damaged the interface, with  $\phi \sim 0.025$ . Microcrack spacing had the most effect on damage in the 10 to 50  $\mu\text{m}$  range, where damage rapidly increases to  $\phi \sim 0.45$ . The effect of microcrack spacing seems to saturate for  $s \leq 5 \mu\text{m}$ . Interestingly the response of ceramic glass and borosilicate glass to laser exposure was nearly identical.

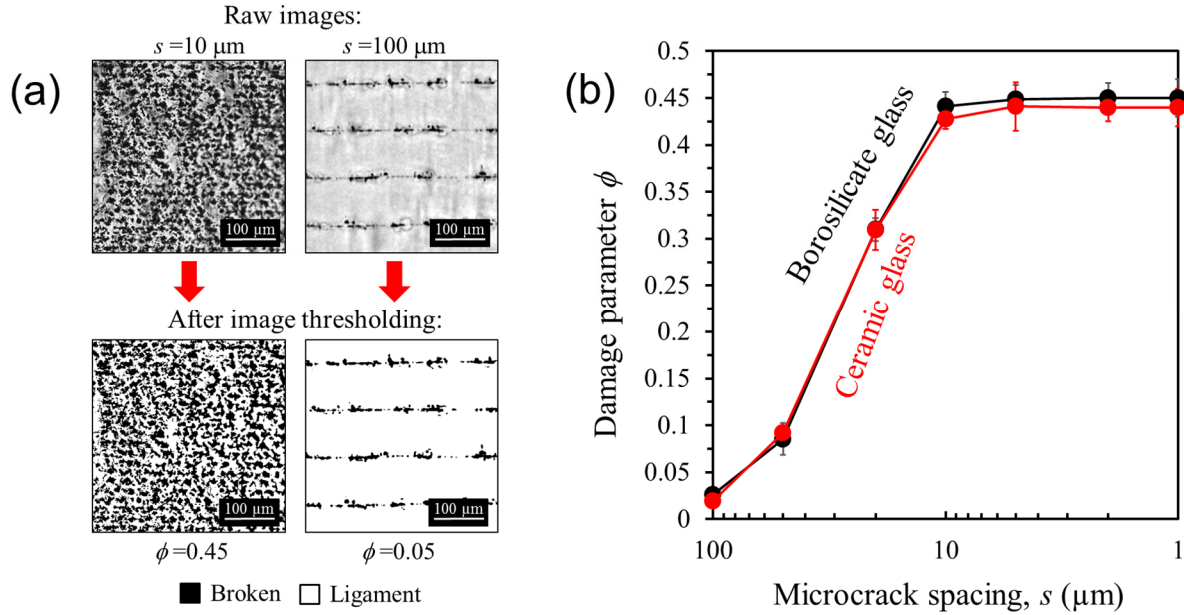


Figure 4-3: (a) Two examples of raw images from confocal microscopy converted to binary images using a thresholding technique; (b) The binary images were used to estimate a damage parameter  $\phi$ , plotted here as function of microcrack spacing  $s$ .

#### 4.5 Fracture toughness and fractography of engraved interfaces

To measure the toughness of the engraved interfaces as function of microcrack spacing and glass type we prepared single edge notch bending (SENB) samples with length of 250 mm, width of 5 mm and thickness of 3.2 mm. A notch with a depth of 0.6 mm was created using a precision diamond saw (Struers, OH, US) (Appendix 4.10.2, Figure 4-10) and the samples were then laser engraved to generate the weak interfaces. Using laser engraving to carve the entire length of the notch was possible, but required high power and special microscopic examinations to ensure that the material was fully cut. Fracture tests were then conducted by loading the sample in a three-point bend configuration, following testing standard [49] (Figure 4-10a, b). We measured the fracture toughness of bulk glass  $K_{IC}^{(b)}$  as reference ( $K_{IC}^{(b)} = 1.032 \pm 0.18 \text{ MPa}\sqrt{\text{m}}$  for borosilicate glass and  $K_{IC}^{(b)} = 1.056 \pm 0.04 \text{ MPa}\sqrt{\text{m}}$  for ceramic glass), and the toughness of the interfaces  $K_{IC}^{(i)}$  created with different microcrack spacing. Figure 4-4a shows the experimental fracture toughness of engraved planes normalized by the fracture toughness of bulk glass  $K_{IC}^{(i)} / K_{IC}^{(b)}$  for different microcrack spacing  $s$  and for borosilicate glass and ceramic glass. The fracture toughness of the

interface is close to bulk glass for  $s = 100 \mu\text{m}$ , and rapidly decreases when the microcrack spacing was decreased to  $s = 10 \mu\text{m}$ . Further decrease of the microcrack spacing ( $s < 10 \mu\text{m}$ ) had a lesser effect on toughness. We were not able to “cut” the sample at the laser engraving stage. Although microcracks coalesced for  $s = 5, 2,$  and  $1 \mu\text{m}$ , the ligaments that bear loads evidently persisted, preventing the complete separation of the interface during laser engraving. There is a slight increase in fracture toughness at  $s = 1 \mu\text{m}$ , possibly because of geometrical interlocking at the heavily damaged interfaces.

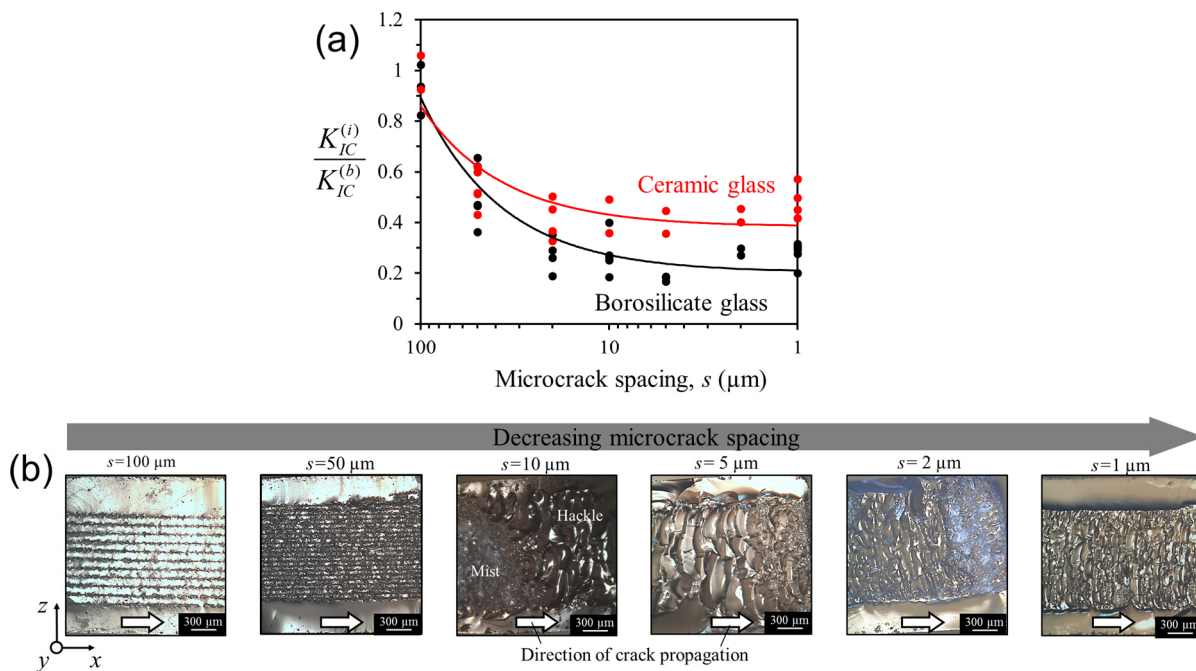


Figure 4-4: Experimental results for the fracture tests. (a) Relative fracture toughness  $K_{IC}^{(i)} / K_{IC}^{(b)}$  plotted as function of microcrack spacing for ceramic glass (red) and borosilicate glass (black); (b) Optical images of fracture surfaces for different microcrack spacing  $s$ . The macro-crack induced by the external load propagated from left to right along the  $x$ -direction.

Figure 4-4b shows optical microscopic images of the fractured surfaces for samples created with six different microcrack spacing. The fracture surfaces exposed the microcracks induced by the laser, particularly the lines parallel to  $x$ -axis seen under the confocal microscope. The spacing of these lines match the microcrack spacing  $s$  set at the laser engraving stage, which confirms that these lines are induced by laser and not as a result of crack propagation due to external load. These

engraved lines can however only be seen for  $s = 100 \mu\text{m}$  and for  $s = 50 \mu\text{m}$ . For  $s = 10 \mu\text{m}$ , these lines were not visible, and the fracture surface had a more typical mist-and-hackle appearance. The texture the fracture surface becomes rougher along  $x$ -direction, forming a “Hackle region” which indicates that the macrocrack induced by external load propagated out of the  $x$ - $z$  plane [50]. Interestingly, the texture became denser and more detailed for  $s < 5 \mu\text{m}$ , which typically indicates that the interface was under higher stresses [50]. This inference is consistent with the slight increase in fracture toughness measured for  $s < 5 \mu\text{m}$ .

#### 4.6 Predicting the fracture toughness of engraved interfaces.

From the image analysis and the fracture test presented above, there is evidently a strong correlation between the initial damage induced by the laser and the apparent fracture toughness of the interface. Experiments clearly showed an exponential or power law decay of  $K_{IC}^{(i)} / K_{IC}^{(b)}$  with more damage. Knowing the size and spacing of the microcrack, it is in theory possible to predict the apparent toughness of the interfaces. The simplest fracture model gives a trend:  $K_{IC}^{(i)} / K_{IC}^{(b)} \propto \phi / \tan(\phi)$  [51] which confirms that apparent toughness decreases with damage. Other analytical [52, 53] or numerical [54] fracture models follow a similar trend, but with additional factors that account for microcracks shape and distribution. However none of these fracture-mechanics based models could predict the decrease of toughness we observed experimentally for smaller microcracks spacing. A likely explanation for this discrepancy is the lack of order and periodicity in the microcracks and their tendency to coalesce during engraving, especially for  $s < 50 \mu\text{m}$  (Figure 4-2c). Alternatively, a simple micromechanics model based on a porous plane could capture this randomness at engraved planes [55-57]. The model assumes open porosity at the interface and a linear elastic response which is in direct correlation with the areal fraction of solid ligaments. This assumption translates into a phenomenological relationship with Young’s modulus:  $E^* = E(1-\phi)^p$  [56], where  $E$  and  $E^*$  are Young’s modulus of non-engraved and engraved samples respectively. This model also translates into a reduction of surface fracture energy  $\gamma^* = \gamma(1-\phi)^q$  [56]. One may therefore write [56, 57]:

$$\frac{K_{IC}^{(i)}}{K_{IC}^{(b)}} = (1-\phi)^n \quad (4.2)$$

where  $\gamma$  and  $\gamma^*$  are the surface energy of non-engraved and engraved samples respectively. The powers  $p$ ,  $q$  and  $n$  are empirical constants.

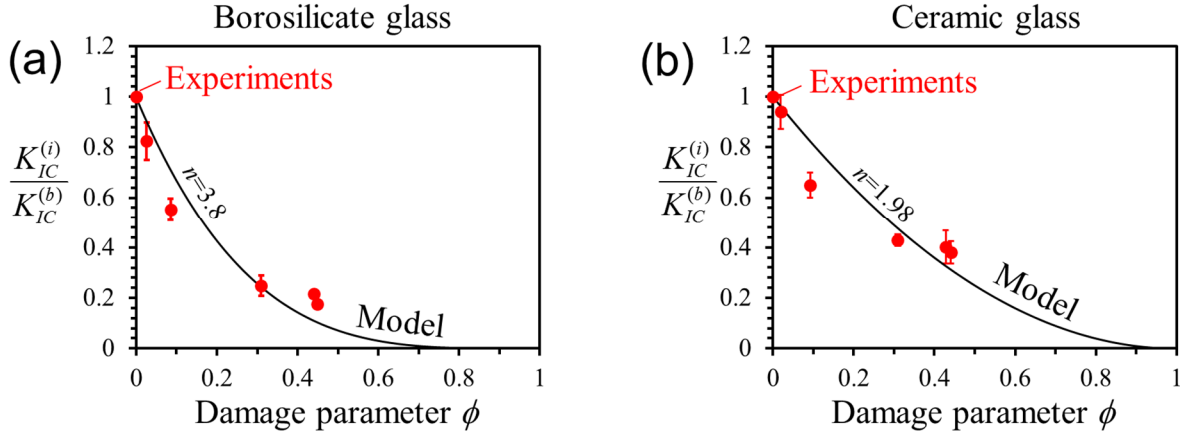


Figure 4-5: Capturing the experimental model using an empirical model for (a) borosilicate glass and (b) ceramic glass.

Equation (4.2) is plotted for the experimental data for different  $\phi$  values (Figure 4-5a and b). We used least square method to minimize the residuals and find the exponents  $n$  that fits the experiments. For borosilicate, the exponent is  $n=3.98$  with  $R^2=0.88$ . For ceramic glass the exponent is  $n=1.98$ , which is lower than that of borosilicate. This indicated that borosilicate glass incurred more damage than ceramic glass. As a result, borosilicate exhibits a sharper decay in toughness with increased  $\phi$  than that of ceramic glass, possibly because ceramic glass has almost zero thermal expansion [2] while borosilicate has a slight coefficient of thermal expansion ( $\approx 3 \times 10^{-6}$  1/K at room temperature [1]). Thermal stresses in borosilicate was therefore higher during laser engraving, resulting in more damage. The exponent  $n$  can capture the two different behaviors of materials based on the different materials interaction with laser, that depends for example on thermal expansion, transparency and composition of glass. The model (equation (4.2)) is based on area fractions, and the measured area fractions remain unchanged for  $s < 5 \mu\text{m}$  (Figure 4-3b). Therefore the model was unable to capture the slight increase in toughness for  $s < 5 \mu\text{m}$ .

#### 4.7 Example: Laser engraved architected panels

With a well-calibrated laser engraving protocol, one can create interfaces with specific fracture toughness within the bulk of glass. In this example we fabricated architected glass panels whose mechanical properties are governed by weaker interfaces and micro-architectures, in ways similar to mollusk shells, teeth or bone [11]. 50 mm× 50 mm × 3 mm borosilicate glass panels served as base materials for these experiments. Samples with this dimensions are easy to handle during engraving and experiments, and they are relevant for many glass applications. We engraved the glass panels through their full thickness following a grid pattern that partitioned the panel into 7×7 blocks where each block was 6.25×6.25×3 mm in size (Figure 4-6a). The microcrack spacing for laser engraving was adjusted to generate weak interfaces of different relative toughness  $K_{IC}^{(i)} / K_{IC}^{(b)}$ . Unlike traditional topologically interlocked panels formed of completely separated blocks [16, 33], the blocks in the engraved architected panels shown on Figure 4-6b are still attached by the weak interfaces ( $K_{IC}^{(i)} > 0$ ). Therefore the engraved glass panels do not require assembly, they can be easily handled, and they do not require special supports, abutments or mechanical confinement from external frames or ligaments.

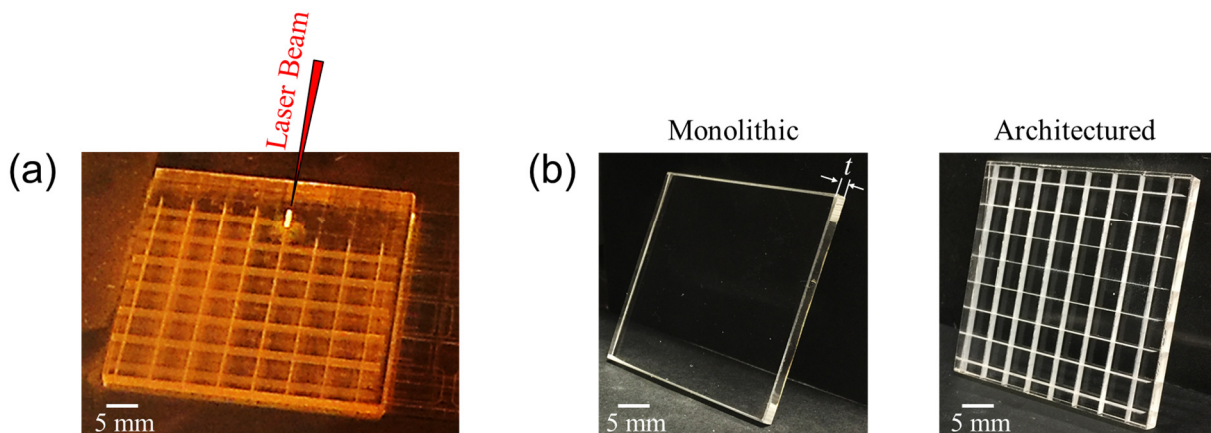


Figure 4-6: (a) Laser engraving a 7×7 grid pattern through the thickness of a monolithic glass panel to create an architected glass panel; (b) borosilicate glass panel before engraving (monolithic) and after engraving (architected).

We tested the architected glass panels under impact loading through an instrumented impact tower (Instron CEAST, MA, US) and using the setup shown on Figure 4-7a. The architected panel was simply supported on a steel frame, and it was struck by a steel impactor with a semi-spherical tip ( $r = 2.4$  mm) at a speed of 2.2 m/s. The kinetic energy of the crosshead and impactor (about 1.2 J) was large enough so that no significant decrease in speed was recorded when the impactor fractured the sample. The force history was recorded by a 3 kN piezoelectric load cell embedded near the tip of the impactor. The impact lasted on average for 3 ms, thus the stages of deformation before, at, and after impact could be captured by taking snapshots at a rate of 1000 frames/second using a high-speed camera.

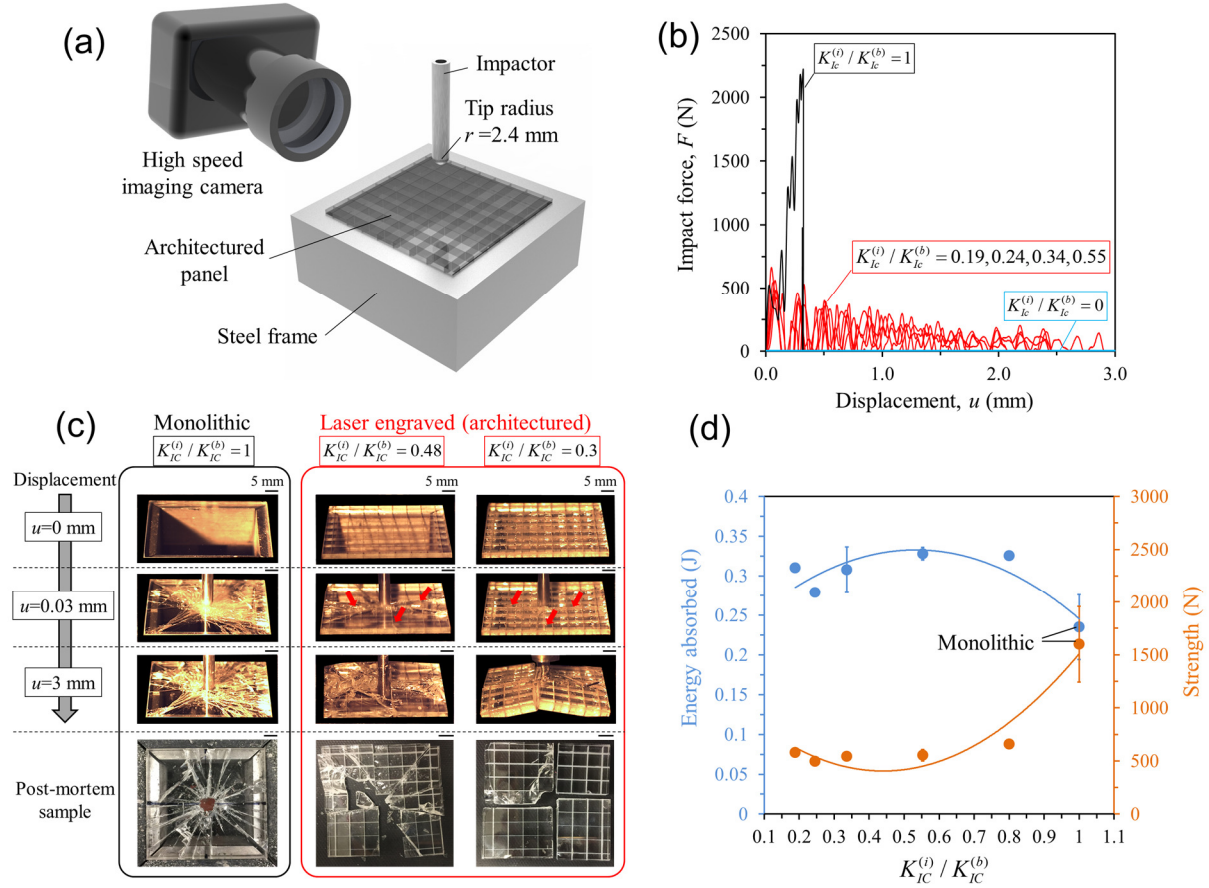


Figure 4-7: (a) Experimental setup for impact testing of borosilicate glass panels and high-speed imaging; (b) impact force-displacement curve for monolithic and architected panels; (c) corresponding high-speed images and post mortem pictures; the red arrows indicate crack deflection and pinning (d) energy absorbed (in dark blue) and strength (in orange) of architected panels fabricated with different interface fracture toughness.

Figure 4-7b shows the impact force  $F$  as function of displacement  $u$  for the monolithic glass panels  $K_{IC}^{(i)} / K_{IC}^{(b)} = 1$  (indicated in black), and for architected glass panels with different levels of interface toughness  $K_{IC}^{(i)} / K_{IC}^{(b)} = 0, 0.19, 0.24, 0.34, 0.55$  (indicated in red). For the monolithic sample, the impact force  $F$  rose quickly until a maximum force of about 2000 N, after which  $F$  dropped suddenly at  $u = 0.3$  mm, corresponding to the complete fracture of the panel. Small fluctuations in the force were attributed to elastic waves and vibrations. Figure 4-7c shows high speed snapshots captured during the impact. For the monolithic sample, the impactor tip impacted the panel at the center where high local contact stresses generated multiple radial cracks from the point of impact. The panel fractured catastrophically and into many fragments. In contrast,

architected panels showed a quick increase in force up to 600 N and a slow progressive decrease in  $F$  until complete fracture at around  $u=2.9$  mm, which is almost ten times the maximum displacement for the monolithic panel. Cracks propagated mostly along the weak interfaces of the grid pattern (marked by red arrows on Figure 4-7c). For  $K_{IC}^{(i)} / K_{IC}^{(b)} = 0.48$ , some cracks were deflected along the interfaces while others were pinned by the grid (post mortem images on Figure 4-7c). The number of fragments was also much smaller than for the monolithic glass. Interestingly for weaker interfaces,  $K_{IC}^{(i)} / K_{IC}^{(b)} = 0.3$ , almost all cracks propagated along interfaces and the panel fractured into 4 clean parts. Unlike monolithic panel, these panels can be reassembled and reused for another cycle of loads, either by re-gluing the parts or by using stiff confining frames as in conventional TIMs made from separate blocks. The larger displacements sustained by the architected glass panel can be explained by the weak interfaces, which once broken can interact by jamming, sliding and hinging [12].

From the impact force-displacement,  $F-u$  curves, we measured the strength (maximum force) and the energy absorption of the panel by calculating the total area under the curves (Figure 4-7d). Architected panels with  $0.189 < K_{IC}^{(i)} / K_{IC}^{(b)} < 1$  absorbed up to 75% more energy (an additional 0.13 J) than the monolithic panel ( $K_{IC}^{(i)} / K_{IC}^{(b)} = 1$ ). The additional 0.13 J is dissipated by the breaking of the interfaces, the sliding of the blocks, crack deflection and crack pinning. These mechanisms are possible because the interfaces are weaker than the bulk material, but on the other hand very weak interfaces are detrimental because interfacial fracture would be too easy. The experimental measurements on Figure 4-7d show that the energy absorption is the highest at the optimum interface fracture toughness of  $K_{IC}^{(i)} / K_{IC}^{(b)} = 0.328$ . Improvement in toughness for the architected panels however came at the expense of strength: the strength of the architected panels was 60% lower than the strength of the monolithic glass panels. To address this drawback, we considered designs where a layer of architected borosilicate glass (with  $K_{IC}^{(i)} / K_{IC}^{(b)} = 0.3$ ) is sandwiched between two 1 mm thick monolithic borosilicate panels. The two panels were glued to the front and back side of the architected layer using cyanoacrylate adhesive (Figure 4-8a). We performed impact tests on the resulting materials using the same protocol as described above. However in this case the total thickness of the sandwiched material was 5 mm, and therefore for comparison we also tested 5 mm thick plain borosilicate panels. Figure 4-8b shows representative

$F-u$  curves for monolithic (in black) and sandwiched architected panels (in green). As expected the failure of the monolithic panel is brittle and catastrophic, with a peak force of about 2250 N. Interestingly the architected panel was almost as strong, with a peak force of about 1500 N, but the deformation of the sandwiched architected panel was more progressive and graceful than the monolithic case. Figure 4-8c shows high-speed snapshots at different stages of deformation for the 5 mm thick monolithic panel and the sandwiched architected panels. The monolithic panel showed the same brittle and catastrophic failure as the 3 mm thick plain samples described above. For the sandwiched architected panel, the snapshots showed that the initial peak of force is generated by the front plain panel, and the fracture of the front layer results in the first drop of force observed on the  $F-u$  curve. The remainder of the curve involves the progressive failure of the architected mid-layer, which involves blocks interacting by sliding and hinging. It is not clear from the data and imaging at what point the plain back layer fractures, but at about  $u=1.5$  mm the panel has completely failed. The failure mode of the sandwich material is still governed by the architecture of the mid layer: the panels fractured into clean parts (post-mortem images of Figure 4-8c).

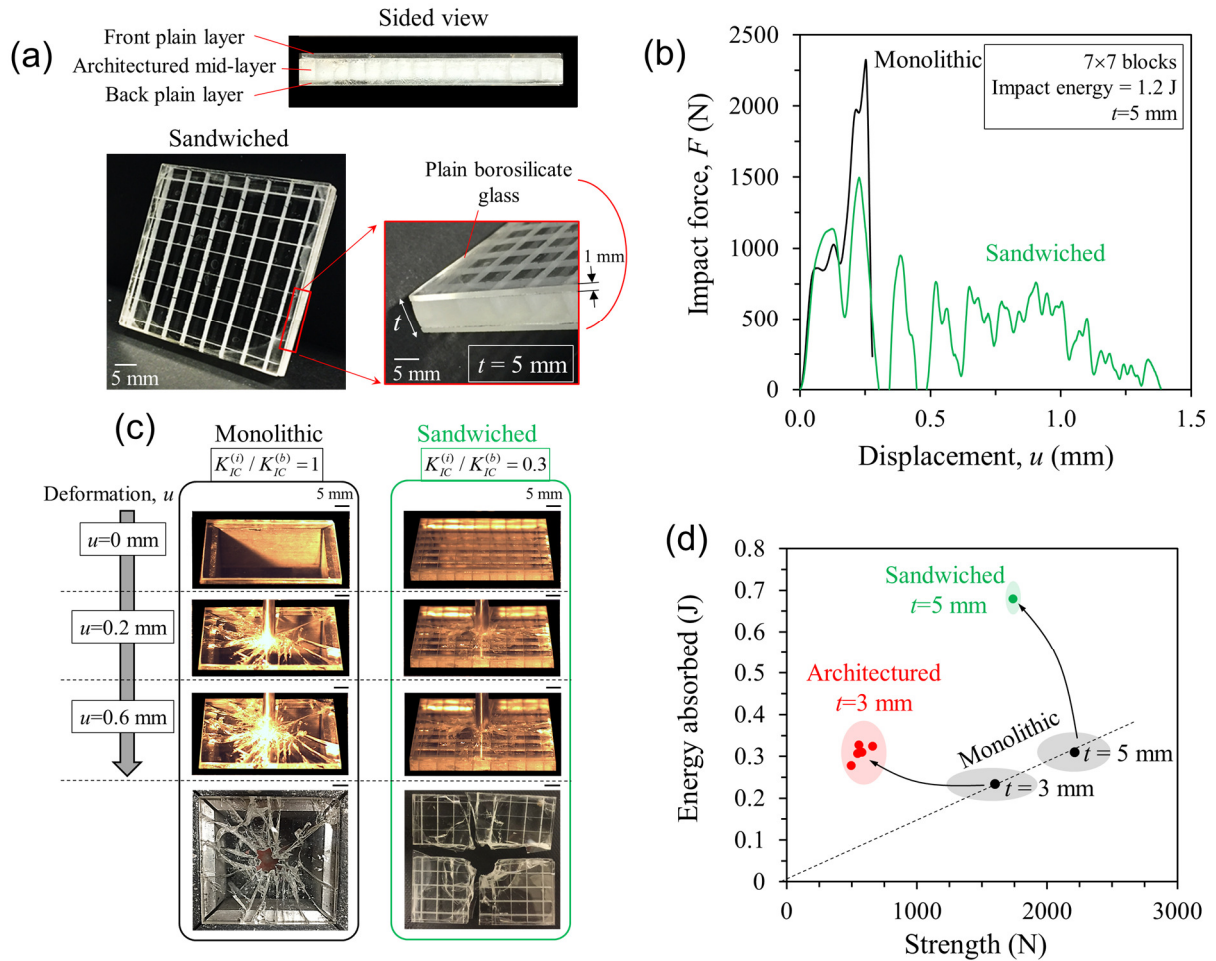


Figure 4-8: (a) Schematic and pictures of the sandwiched architecture glass panel; (b)  $F-u$  curves for monolithic panel and sandwiched panels; (c) high speed snapshots during impact at  $u=0, 0.2, 0.6 \text{ mm}$ , with post mortem images; (d) summary of all tests results on an Ashby like plot for strength-energy absorbed.

Figure 4-8d is an Ashby chart showing strength and energy absorption for all the samples tested in this chapter. The monolithic panels were relatively strong, but with little energy absorption. Thicker panels were stronger and absorbed more energy, these two properties scaling linearly with the thickness of the panel (dashed line). Thicker samples were also more prone to failure by sliding (shearing of the interfaces) due to their lower span-to-thickness ratio, whereas thinner samples were prone to failure by interface opening (hinging) [12]. The 3 mm thick architected panels absorbed 40% more energy than the 3mm thick monolithic panel, but at the expense of a drop of 60% in strength. The sandwiched architected panels absorbed 2.2 times more energy than the 5 mm thick monolithic panel, for a loss of strength of only 27%. These results suggest that the front

and back plain layers in the sandwich design not only increase strength, but also enhance energy dissipative mechanisms in the architected mid-layer probably by confining the architected blocks and increasing frictional dissipation.

Single-phase architected materials as in this chapter, rely on geometry and the presence of interfaces for toughening (e.g. sliding, crack pinning) or strengthening mechanisms (e.g. jamming of blocks). In multi-phase architected materials, additional characteristic such as damping effect can be added to the materials by the addition of viscoelastic phases. The addition of soft materials to interfaces can reduce contact stresses, control friction, vary the failure mode and provide an additional energy dissipation mechanism. The absence of any polymer however in single-phase architected materials is advantageous for high temperature applications. More complex patterns (with  $K_{IC}^{(i)} > 0$ ) that takes the hexagonal or circular patterns may generate additional in-plane confinement that result in more jamming between blocks and therefore in more strength overall.

## 4.8 Summary

In this study we characterized the morphology of individual microcracks generated by discrete laser pulses focused within glass, as well as the effects of microcrack spacing on the morphology of engraved interfaces within the bulk of glass. We used confocal imaging and a local thresholding method to compute a damage parameter  $\phi$  which can be used to predict the fracture toughness of interfaces through a simple model. We then engraved a simple square pattern into glass panels, and we manipulated the toughness of the interfaces to generate different combinations of strength and toughness. We draw the following conclusions from this study:

1. In these experiments the power of the laser was maintained to a constant value (400 mW). At this power, confocal images revealed that individual microcracks have dimensions of about 100  $\mu\text{m}$ , 20  $\mu\text{m}$  and 5  $\mu\text{m}$ , and that they are elongated along the laser beam direction.
2. For microcrack spacing of  $s > 100 \mu\text{m}$ , we observed discrete microcracks at the interfaces. For  $s \leq 100 \mu\text{m}$  we observed coalescence of microcracks along the direction of laser engraving. For  $s \leq 20 \mu\text{m}$  we observed coalescence of microcracks along all directions. The effect of decreasing microcrack spacing on the damage parameter saturated for  $s \leq 10 \mu\text{m}$ .

3. Decreasing microcrack spacing rapidly decrease the interface toughness from  $K_{IC}^{(i)} / K_{IC}^{(b)} = 1$  down to  $K_{IC}^{(i)} / K_{IC}^{(b)} = 0.38$ , over the range  $10 \leq s \leq 100 \mu\text{m}$ . The weakening effect saturated at  $s=10 \mu\text{m}$ . Reducing microcrack spacing to smaller values  $s < 10 \mu\text{m}$  had little additional effects on fracture toughness. However even at the smallest microcrack spacing ( $s=1 \mu\text{m}$ ), the interface was never entirely cut because some ligament persisted across the interface
4. Using the damage parameter  $\phi$  we could predict the fracture toughness of the interfaces using a simple empirical model.
5. The engraved glass panels we designed and fabricated are based on all-brittle component and can operate in free standing conditions. Compared to plain glass, we observed more progressive and graceful force-displacement curves under impact loads. Maximum deformation was almost 10 times higher, energy absorption was 75% higher. In basic designs the improvement in toughness was at the expense of a loss of 60% strength.
6. In contrast to monolithic glass panels where failure was catastrophic, the architected glass panels broke into four parts along the engraved interface. Unlike monolithic, the broken parts of architected panel can be reassembled and reused with the aid of side supports, ligaments or glue.
7. To address the 60% loss in strength of the simply engraved design we sandwiched the engraved layer between two thin monolithic panels, which reduced the loss in strength from 60% to 27%. In addition, this design improved toughness probably because of the added confinement of the architected blocks.

This study shows how 3D laser engraving can be used in glass to generate weak interfaces without completely cutting the material into blocks. The interfaces are strong enough so the engraved glass panels can be handled without separation of the blocks. They are also weak enough to deflect cracks, prevent cracks from spreading and growing across blocks, even in the absence of mechanical confinement. This fabrication method may be applicable to other transparent materials such as acrylic, PMMA, and other types of glasses. The laser engraving method is amenable to the design and fabrication of many micro-architecture designs, many of which could be inspired from architectures found in hard biological materials.

## 4.9 Acknowledgements

We thank Prof. Allen J. Ehrlicher (bioengineering department, McGill) for providing access and training for the confocal microscope facility at his lab. This work was supported by a Strategic Grant (STPGP 479137-5) from the Natural Sciences and Engineering Research Council of Canada and by a Team Grant (191270) from the Fonds de Recherche du Québec – Nature et Technologies. A.D. was partially supported by a McGill Engineering Doctoral Award.

## 4.10 Appendix

### 4.10.1 Converting confocal images to binary images

Grayscale were converted to binary images using a thresholding method. Each image has a field intensity distribution of  $I(x, z)$  on 8-bit grey scale. The simplest form of thresholding is:

$$I(x, z) = \begin{cases} 255 \text{ (white)} & \text{if } I(x, z) \geq T \\ 0 \text{ (black)} & \text{if } I(x, z) < T \end{cases} \quad (4.10.1)$$

where  $T$  is a fixed threshold value of intensity. There is no universal method to set the threshold limit  $T$ , different images may require different  $T$  depending on the image contrast, illumination gradients and on the density of features on the image. There are however several methods to finding optimal  $T$  (if any) that depends on the histogram of pixel intensity  $I$  (a frequency histogram) (second column on Figure 4-9a). Setting a fixed threshold  $T$  over the whole image is known as a global thresholding method. Global methods are best suited for bimodal histograms, in other words when the intensities of the pixels cluster at two widely different intensities which forms two distant narrow peaks in the histogram. Since our images were not bimodal, global methods were not appropriate [55]. Instead adaptive global methods that generate an optimal  $T$  using the mean, the variance as in Ostu-method [56], or entropy [57] are more appropriate. In addition, the presence of illumination gradient and fine features require local adaptive thresholding methods. Local methods selects a local threshold value of  $T(x, z)$  for each pixel based on the statistics (mean and variance) of the local neighborhood of the pixel. Here we used the local thresholding method

proposed by Phansalkar to amplify the local threshold  $T(x,z)$  using an exponential term [45]. The local intensity follows:

$$T(x, z) = \bar{I}_l \left( 1 + p \exp(-q\bar{I}_l) + k \left( \frac{\sigma(x, z)}{R} - 1 \right) \right) \quad (4.10.2)$$

Where  $\bar{I}_l$  and  $\sigma(x, z)$  is the mean and the standard deviation of local intensity in the neighborhood of a pixel at  $(x, z)$ , respectively. The parameters  $p$ ,  $q$  and  $k$  are constants that depend on the type of the images.  $R$  is the range of the standard deviation, which captures the local contrast; for very large contrast we get  $\sigma(x, z) \approx R$ . The neighborhood boundary is made of a circular window of radius  $r$ , where we used a representative radius of  $r=15$  pixels, which is large enough to capture the statistics near  $(x, z)$  point. Different  $r$  values are checked until the area fractions of black to white are independent of  $r$ . As suggest by Phansalkar, for best results for images containing smeared particles which are very similar to the confocal images of engraved interfaces at hand, we used  $p=2$ ,  $q=10$  and  $k=0.25$  [45].

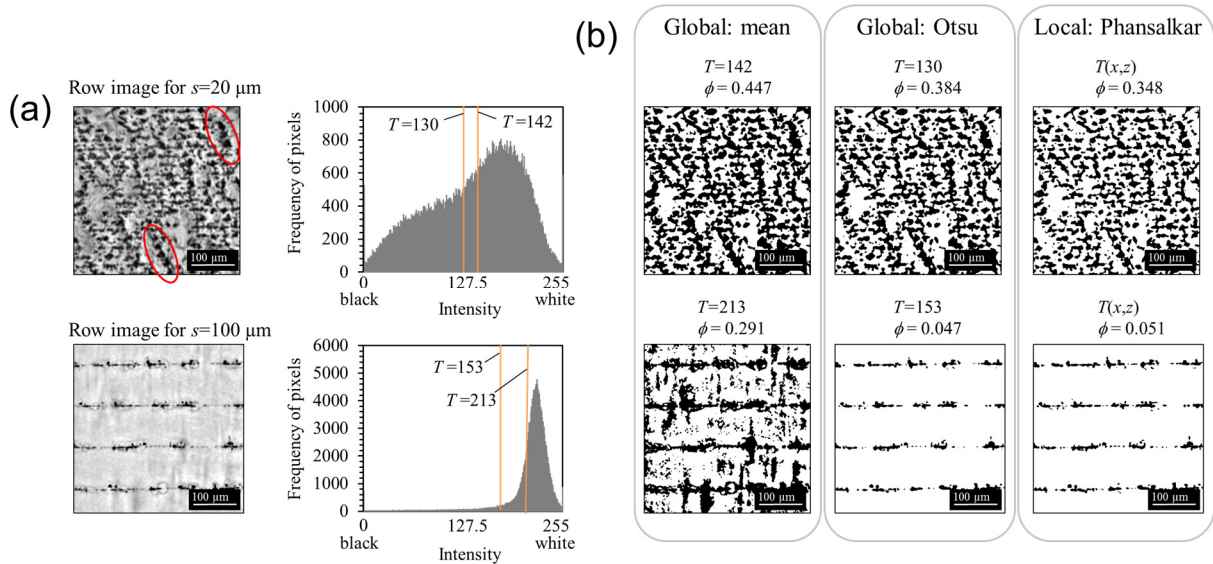


Figure 4-9: Thresholding of raw confocal images. (a) raw confocal image (first column) and their frequency histogram, challenging regions are indicated by red circles; (b) binary images generated by 3 different thresholding algorithms: mean, Otsu and Phansalkar.

Figure 4-9b shows binary images generated by different adaptive methods. Setting the threshold to a mean value of the intensity histogram,  $T = \bar{I} = 142$  for  $s=20 \mu\text{m}$  and  $T = \bar{I} = 213$  for  $s=100$

$\mu\text{m}$  exaggerate the size of the damaged areas (black areas) and undersize the ligaments areas (white areas) for both cases. Otsu method generated better result but quickly fails if illumination gradients is present. In contrast, the local criterion captured the outline of the broken parts quite well, including the challenging fine outlines marked by a red circle on Figure 4-9a. Whereas, Otsu method merged these challenging damaged areas together which resulted in a slightly higher damage parameter  $\phi$  for  $s=20 \mu\text{m}$ . We therefore adapted Phansalkar method for all estimations of  $\phi$ .

#### 4.10.2 Measuring the fracture toughness of engraved interfaces

A single-edge notched bend specimen (SE(B)) with a thickness  $B$ , depth of  $W$  is prepared as recommended in ASTM-1820 [46]. A 0.6 mm deep pre-crack (notch) was made on each specimen using a diamond saw (Struers, OH, US). Each sample have a length of  $L=250 \text{ mm}$ , depth  $W=5 \text{ mm}$  and a thickness of  $B=3.2 \text{ mm}$ . The sample is mounted under a dual-column loading stage (Admet, model eXpert 5000, MA US), the loading head moves at a displacement rate of  $10 \mu\text{/s}$ . The transverse load  $P$  was measured using a 500 lbf load cell (Figure 4-10b). Using the critical load  $P_c$  at fracture (Figure 4-10c), we compute the fracture toughness using equations:

$$K_{IC} = \frac{P_c S}{BW^{3/2}} f(a/W) \quad (4.10.3)$$

$$f(a/W) = \left( 2 + \frac{a}{W} \right) \left( \frac{0.886 + 4.64 \frac{a}{W} - 13.32 \left( \frac{a}{W} \right)^2 + 14.72 \left( \frac{a}{W} \right)^3 - 5.6 \left( \frac{a}{W} \right)^4}{\left( 1 - \frac{a}{W} \right)^{3/2}} \right) \quad (4.10.4)$$

We therefore estimated the fracture toughness of borosilicate and ceramic glass to be  $K_{IC}^{(b)} = 1.032 \pm 0.18 \text{ MPa}\sqrt{\text{m}}$  and  $1.056 \pm 0.04 \text{ MPa}\sqrt{\text{m}}$ ; respectively. These measurements are in good agreement with values reported in the literature ( $K_{IC} \approx 1 \text{ MPa}\sqrt{\text{m}}$  [7]).

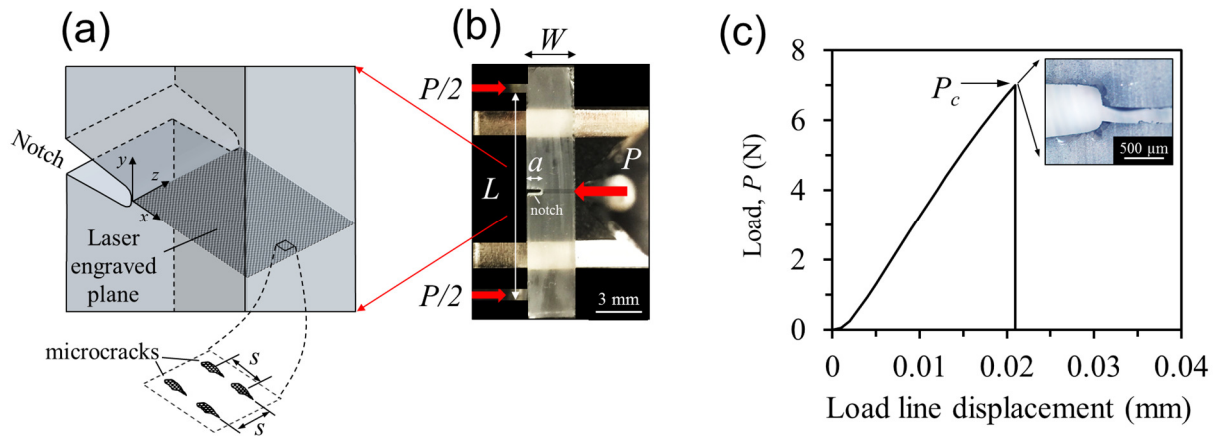


Figure 4-10: Fracture toughness test for the engraved interfaces: (a) schematic of the engraved interface in front of a sharp notch; (b) a bend fracture sample mounted in a 3-point bending test configuration; (c) load-displacement curve showing the critical load  $P_c$  at fracture, where the inset shows the sample after fracture.

#### 4.11 References

1. Shelby, J.E. and M. Lopes, *Introduction to Glass Science and Technology*. 2 ed. 2005, Cambridge: Royal Society of Chemistry. X001–X004.
2. Varshneya, A.K., *Fundamentals of Inorganic Glasses*. 1994, New York: Gulf Professional Publishing. 590.
3. Wondraczek, L., et al., *Towards Ultrastrong Glasses*. *Advanced Materials*, 2011. **23**(39): p. 4578-4586.
4. Petit, F., et al., *Fracture toughness and residual stress measurements in tempered glass by Hertzian indentation*. *Acta Materialia*, 2007. **55**(8): p. 2765-2774.
5. Norville, H.S., W. King Kim, and L. Swofford Jason, *Behavior and Strength of Laminated Glass*. *Journal of Engineering Mechanics*, 1998. **124**(1): p. 46-53.
6. Ashby, M.F., *Hybrids to fill holes in material property space*. *Philosophical Magazine*, 2005. **85**(26-27): p. 3235-3257.
7. Ashby, M.F., *Materials Selection in Mechanical Design*. 5 ed. 2016, Cambridge, MA: Butterworth-Heinemann. 664.
8. Bouaziz, O., Y. Bréchet, and J.D. Embury, *Heterogeneous and Architected Materials: A Possible Strategy for Design of Structural Materials*. *Advanced Engineering Materials*, 2008. **10**(1-2): p. 24-36.
9. Krstic, V.V., P.S. Nicholson, and R.G. Hoagland, *Toughening of Glasses by Metallic Particles*. *Journal of the American Ceramic Society*, 1981. **64**(9): p. 499-504.
10. Huang, H., et al., *U-involved sphere-dispersed metallic glass matrix composites*. *Materials & Design*, 2018. **157**: p. 371-376.
11. Barthelat, F., *Architected materials in engineering and biology: fabrication, structure, mechanics and performance*. *International Materials Reviews*, 2015. **60**(8): p. 413-430.
12. Dalaq, A.S. and F. Barthelat, *Strength and stability in architected spine-like segmented structures*. *International Journal of Solids and Structures*, 2019. **171**: p. 146-157.

13. Abueidda, D.W., et al., *Micromechanical finite element predictions of a reduced coefficient of thermal expansion for 3D periodic architected interpenetrating phase composites*. Composite Structures, 2015. **133**: p. 85-97.
14. Dalaq, A.S., D.W. Abueidda, and R.K. Abu Al-Rub, *Mechanical properties of 3D printed interpenetrating phase composites with novel architected 3D solid-sheet reinforcements*. Composites Part A: Applied Science and Manufacturing, 2016. **84**: p. 266-280.
15. Song, J., et al., *Octet-truss cellular materials for improved mechanical properties and specific energy absorption*. Materials & Design, 2019. **173**: p. 107773.
16. Mirkhalaf, M., T. Zhou, and F. Barthelat, *Simultaneous improvements of strength and toughness in topologically interlocked ceramics*. Proceedings of the National Academy of Sciences, 2018. **115**(37): p. 9128-9133.
17. Yazdani Sarvestani, H., et al., *Multilayered architected ceramic panels with weak interfaces: energy absorption and multi-hit capabilities*. Materials & Design, 2019. **167**: p. 107627.
18. Barthelat, F., *Biomimetics for next generation materials*. Philosophical Transactions of the Royal Society of London A: Mathematical, Physical and Engineering Sciences, 2007. **365**(1861): p. 2907-2919.
19. Fratzl, P., et al., *The mechanics of tessellations - bioinspired strategies for fracture resistance*. Chemical Society Reviews, 2016. **45**(2): p. 252-267.
20. Abid, N., M. Mirkhalaf, and F. Barthelat, *Discrete-element modeling of nacre-like materials: Effects of random microstructures on strain localization and mechanical performance*. Journal of the Mechanics and Physics of Solids, 2018. **112**: p. 385-402.
21. Wang, R.Z., et al., *Deformation mechanisms in nacre*. Journal of Materials Research, 2001. **16**(9): p. 2485-2493.
22. Barthelat, F., et al., *On the mechanics of mother-of-pearl: A key feature in the material hierarchical structure*. Journal of the Mechanics and Physics of Solids, 2007. **55**(2): p. 306-337.
23. Abid, N., J.W. Pro, and F. Barthelat, *Fracture mechanics of nacre-like materials using discrete-element models: Effects of microstructure, interfaces and randomness*. Journal of the Mechanics and Physics of Solids, 2019. **124**: p. 350-365.
24. Zhu, H., et al., *Nacre-like composite films with a conductive interconnected network consisting of graphene oxide, polyvinyl alcohol and single-walled carbon nanotubes*. Materials & Design, 2019. **175**: p. 107783.
25. Yin, Z., F. Hannard, and F. Barthelat, *Impact-resistant nacre-like transparent materials*. Science, 2019. **364**(6447): p. 1260-1263.
26. Magrini, T., et al., *Transparent and tough bulk composites inspired by nacre*. Nature Communications, 2019. **10**(1): p. 2794.
27. Flammang, B.E., et al., *Functional morphology of the fin rays of teleost fishes*. Journal of Morphology, 2013. **274**(9): p. 1044-1059.
28. Porter, M.E., R.H. Ewoldt, and J.H. Long, *Automatic control: the vertebral column of dogfish sharks behaves as a continuously variable transmission with smoothly shifting functions*. The Journal of Experimental Biology, 2016. **219**(Pt 18): p. 2908-2919.
29. Troxell, E.L., *Mechanics of Crocodile Vertebrae*. GSA Bulletin, 1925. **36**(4): p. 605-614.
30. Dyskin, A.V., et al., *Toughening by Fragmentation—How Topology Helps*. Advanced Engineering Materials, 2001. **3**(11): p. 885-888.

31. Dyskin, A.V., et al., *Topological interlocking of platonic solids: A way to new materials and structures*. Philosophical Magazine Letters, 2003. **83**(3): p. 197-203.
32. Feng, Y., et al., *Impact mechanics of topologically interlocked material assemblies*. International Journal of Impact Engineering, 2015. **75**: p. 140-149.
33. Siegmund, T., et al., *Manufacture and Mechanics of Topologically Interlocked Material Assemblies*. Applied Mechanics Reviews, 2016. **68**(4): p. 040803-040803.
34. Mirkhalaf, M., et al., *Toughness by segmentation: Fabrication, testing and micromechanics of architected ceramic panels for impact applications*. International Journal of Solids and Structures, 2018.
35. August, M.G. *Pearl coating built from the ground up*. Chemistry World 2019 2019/09/16/00:10:08; Available from: <https://www.chemistryworld.com/news/pearl-coating-built-from-the-ground-up/1017294.article>.
36. Mirkhalaf, M., J. Tanguay, and F. Barthelat, *Carving 3D architectures within glass: Exploring new strategies to transform the mechanics and performance of materials*. Extreme Mechanics Letters, 2016. **7**: p. 104-113.
37. Yin, Z., A. Dastjerdi, and F. Barthelat, *Tough and deformable glasses with bioinspired cross-ply architectures*. Acta Biomaterialia, 2018. **75**: p. 439-450.
38. Rastogi, V., S. Chaurasia, and D.S. Munda, *Laser induced damage studies in borosilicate glass using nanosecond and sub nanosecond pulses*. Journal of Non-Crystalline Solids, 2017. **463**: p. 138-147.
39. Zeng, X., et al., *Experimental investigation of ablation efficiency and plasma expansion during femtosecond and nanosecond laser ablation of silicon*. Applied Physics A, 2005. **80**(2): p. 237-241.
40. Do, B.T., et al. *The damage mechanism in borosilicate glass generated by nanosecond pulsed laser at 1.064*. 2012.
41. Sugioka, K. and Y. Cheng, *Ultrafast lasers—reliable tools for advanced materials processing*. Light: Science & Applications, 2014. **3**(4): p. e149.
42. Wu, B. and Y.C. Shin, *Modeling of nanosecond laser ablation with vapor plasma formation*. Journal of Applied Physics, 2006. **99**(8): p. 084310.
43. Rastogi, V., S. Chaurasia, and D.S. Munda, *Laser Induced Damage Studies in Borosilicate Glass Using nanosecond and sub nanosecond pulses*. arXiv:1601.03146 [physics], 2016.
44. Martienssen, W. and H. Warlimont, *Springer Handbook of Condensed Matter and Materials Data*. 2006, New York: Springer Science & Business Media. 1143.
45. Karmakar, B., *Functional Glasses and Glass-Ceramics: Processing, Properties and Applications*. 2017, Cambridge, MA: Butterworth-Heinemann. 418.
46. Mirkhalaf, M., A.K. Dastjerdi, and F. Barthelat, *Overcoming the brittleness of glass through bio-inspiration and micro-architecture*. Nature Communications, 2014. **5**.
47. Steen, W.M. and J. Mazumder, *Basic Laser Optics*, in *Laser Material Processing*, W.M. Steen and J. Mazumder, Editors. 2010, Springer London: London. p. 79-130.
48. Neerad, P., et al. *Adaptive local thresholding for detection of nuclei in diversity stained cytology images*. in *2011 International Conference on Communications and Signal Processing*. 2011.
49. International, A., *Test Method for Measurement of Fracture Toughness (ASTM e-1820)*. 2004, ASTM International: USA.
50. Quinn, G.D., *Fractography of Ceramics and Glasses*. 2007, Gaithersburg, Md: National Institute of Standards and Technology. book.

51. Anderson, T.L. and T.L. Anderson, *Fracture Mechanics: Fundamentals and Applications*. 3 ed. 2005, New York: CRC Press. 648.
52. Lekesiz, H., et al., *The stress intensity factors for a periodic array of interacting coplanar penny-shaped cracks*. International Journal of Solids and Structures, 2013. **50**(1): p. 186-200.
53. Tada, H., P.C. Paris, and G.R. Irwin, *The Stress Analysis of Cracks Handbook*. 3 ed. 2000, Three Park Avenue New York, NY 10016-5990: ASME.
54. Dong, C.Y. and K.Y. Lee, *Numerical analysis of doubly periodic array of cracks/rigid-line inclusions in an infinite isotropic medium using the boundary integral equation method*. International Journal of Fracture, 2005. **133**(4): p. 389-405.
55. Jelitto, H. and G.A. Schneider, *A geometric model for the fracture toughness of porous materials*. Acta Materialia, 2018. **151**: p. 443-453.
56. Wagh, A.S., J.P. Singh, and R.B. Poeppel, *Dependence of ceramic fracture properties on porosity*. journal of Materials Science, 1993. **28**(13): p. 3589-3593.
57. Flinn, B.D., et al., *Evolution of defect size and strength of porous alumina during sintering*. Journal of the European Ceramic Society, 2000. **20**(14): p. 2561-2568.

---

## Chapter 5

### Conclusions

---

# Chapter 5: Conclusions

## 5.1 Summary of the findings

This thesis mainly focused on the mechanics of segmented beams. First, a simple beam composed of a row of cubes to study the underlying mechanics of segmentation is considered. The system in hand was assessed by applying a transverse force  $F_T$  while being subjected to an axial precompression  $F_A$ . Then, the attention shifted towards the effect of the geometry of individual blocks (segments). Therefore, the contact faces of blocks were enriched with 2D polynomial functions which transformed the contact faces of blocks from flat to curved and then wavy. Optimum designs were found computationally and tested experimentally. Finally, a 3D pulsating laser is used to engrave 3D network of interfaces in glass panels. The effect of laser on interfaces was characterized using confocal microscopy, while strength and toughness of architected panels was assessed using impact testing. The outcome of the thesis can be summarized as follows:

1. Short segmented beams fail by sliding, where  $F_T$  in the system depends on friction. Long and slender segmented beams can show a nonlinear behavior where three or four interfaces open, reflecting a “hinging” failure mode, where the maximum  $F_T$  (strength) is independent of friction. The critical force at sliding and hinging are proportional to the initial compressive force  $F_A$ . The transition between hinging and sliding (failure mode) is strongly dependent on the number of blocks  $N$  and on the friction coefficient  $f$ , but independent of  $F_A$ .
2. The geometry of the interfaces between the blocks can have a profound effect on overall behavior and properties of segmented beams. Round interfaces can delay hinging and promote sliding and induce geometric hardening resulting from progressive jamming of blocks, that is dependent on the Young’s modulus and surface friction of blocks. Specifically, it was found that interlocking geometries along loading direction that are curved and wavy generates more progressive hardening, which promotes higher energy absorption (toughness) and maximum  $F_T$  (strength). A geometric parameter:

$$\phi L = \frac{1}{L} \left\langle \frac{\partial^2 z}{\partial y^2} + \frac{\partial^2 z}{\partial y \partial x} \right\rangle \left/ \left\langle \frac{\partial z}{\partial y} + \frac{\partial z}{\partial x} \right\rangle \right.$$
 is devised which can characterize the “waviness” of

contact faces of blocks where both strength and toughness were found to correlate well with it. Individual strength of blocks limits both toughness and strength. Designs with flat contact faces achieve high toughness by sliding. Curved and wavy contact faces generate higher stresses, so they require stronger blocks but can achieve higher strength and toughness by progressive interlocking between blocks. Experiments revealed that architected beams are up to 370 times tougher than monolithic counterpart and it preserved 40% of strength of the monolithic sample.

3. Laser engraver can be used to generate discrete arrays of microcracks that can form engraved interfaces in transparent materials. Confocal microscopic images revealed that individual microcracks are elongated and have dimensions of 100  $\mu\text{m}$ , 20  $\mu\text{m}$  and 5  $\mu\text{m}$ . Controlling the spacing between microcracks  $s$  can tune the fracture toughness of engraved interfaces. Decreasing the spacing between microcracks rapidly decreases the fracture toughness of interfaces. Using the confocal microscopic images, a damage parameter at engraved interfaces was characterized which could predict the fracture toughness of interfaces for different  $s$  quite well. A grid pattern is engraved on borosilicate glass panels. These engraved panels generated a more progressive deformation that reflected a higher toughness (75% higher) than the monolithic (plain panels) but at the expense of strength (60% loss of strength). To address the 60% loss in strength, a sandwiched structure is proposed where the engraved layer is positioned between two thin monolithic panels, which reduced the loss in strength from 60% to 27%.

## 5.2 Thesis contributions and accomplishment

The following list summarizes the main contributions and accomplishments achieved during the present study:

- Developed comprehensive analytical and computational models for predicting the failure mode, deformation, strength, and toughness of segmented systems.

- Developed a framework to control geometric features in architected materials and predict both strength and toughness of such systems using a single geometric parameter (a general metric).
- Generated damage-tolerant thick glass panels formed by laser engraving of monolithic glass into blocks joined by weak interfaces.
- Demonstrated how confocal microscopy is an effective method for characterizing damage in transparent materials.

### 5.3 Possible future directions

This thesis focused on segmented beams and addressed the role of the fracture toughness of interfaces in architected materials. Future work would focus more on panels and 3D design of architected materials.

- Architected materials like any other will be disposed of when failed. Shape memory alloys (SMA) could offer a solution to this problem, where the system could reconstruct itself to original configuration. This addition will endow segmented systems with self-healing capability.
- These segmented systems are ideal for artwork where different shapes can be morphed into stunning sculptures with visual and movement resolution controlled by the shape and number of blocks.
- A neural network can be trained to design architected materials. In addition to optimization schemes, this neural network can unlock some uncharted areas in the design space.
- Chapter 2 of this thesis may provide a mechanical viewpoint for the causes of vertebral disc herniation of spines. This study can be followed up with another study where soft interfaces are incorporated in the design of segmented system, which is more representative of human spines. The failure maps developed in chapter 2 can be extended to incorporate the effect of adding the soft interfaces between blocks.
- Chapter 3 of this thesis can be followed with a 3D rigid element-based model to assess deformation rapidly and find optimum designs using Nelder–Mead algorithm/brute force

methods as well as machine learning. Finally compare results and explore how machine learning could assist the design process.

- Cellular materials are an equally powerful approach of architected materials for energy absorption. Similar to the case of bones, where all strategies of architected materials are present. Material of the future may have cellular core and external segmented armors (a protective TIM layer). The proportion of these two regions can be optimized using Mesh Adaptive Direct Search optimization algorithm and machine learning. Soft spots are to be fabricated with cellular materials while hard spots can be filled with TIMs.
- An extension to chapter 5, a high frequency pulsating laser could be used (femtosecond laser) and accordingly examine the variation of interface toughness with microcracks spacing. Instead of using a damage-based model as in chapter 5, a rigorous fracture model could be used to capture the decrease of interface fracture toughness with the decrease in the microcrack spacing. This study will demonstrate how laser induced microcracks by the femtosecond laser are less rough and more uniform than low frequency laser cases.

## 5.4 Publications

### 5.4.1 Refereed journals

1. **Dalaq, A. S.**, Barthelat, F., 2019, “Manipulating the geometry of architected beams for maximum toughness and strength”, *Materials and Design (JMAD)* (Under review).
2. **Dalaq, A. S.**, Barthelat, F., 2020, “Three-Dimensional Laser Engraving for Fabrication of Tough Glass-Based Bioinspired Materials”, *The Journal of The Minerals, Metals & Materials Society (JOM)* (published).
3. **Dalaq, A. S.**, Barthelat, F., 2019, “Strength and stability in architected spine-like segmented structures”, *International Journal of Solids and Structures (IJSS)*, 2019. 171: p. 146-157. (published)

#### 5.4.2 Conference papers and presentations

4. **Dalaq, A. S.**, Barthelat, F., 2019, “Manipulating the architecture of beams for high toughness and strength”, Canadian Society for Mechanical Engineering (CSME-CFDSC Congress 2019), London, Ontario, Canada.
5. **Dalaq, A. S.**, Barthelat, F., 2018, “Deformation and failure of bioinspired segmented architected beams and plates”, The minerals metals & materials society (TMS), Arizona, USA.